The Observational and Theoretical Tidal Radii of Globular Clusters in M87

The Observational and Theoretical Tidal Radii of Globular Clusters in M87

By

Jeremy J. Webb, B.Sc.

A Thesis

Submitted to the School of Graduate Studies

in Partial Fulfilment of the Requirements

for the Degree

Master of Science

McMaster University

Master of Science (2011) McMaster University

(Department of Physics and Astronomy) Hamilton, Ontario

TITLE: The Observational and Theoretical Tidal Radii of Globular Clusters in M87

AUTHOR: Jeremy Webb, B.Sc.

SUPERVISOR: Alison Sills, William Harris

NUMBER OF PAGES: xvii, 180

Abstract

Globular clusters have linear sizes (tidal radii) which are theoretically determined by their mass and by the gravitational potential of their host galaxy. However observationally, cluster sizes are simply a determination of where the cluster's surface brightness profile becomes zero. This distance is also known as the limiting radius. While it is commonly assumed that the tidal radius and the limiting radius of a globular cluster are the same thing, it has yet to be validated. The purpose of this thesis is to explore the assumption that cluster tidal radii and limiting radii are equal by comparing the tidal radii of an observed and simulated globular cluster population.

An established link between cluster tidal radii and limiting radii will yield new methods of utilizing globular clusters as tools for studying galaxies. If cluster sizes are truly imposed by the tidal field of the host galaxy, then tidal radii measurements can be used to trace the mass distribution within a galaxy, including the dark matter halo. Additionally, as we will demonstrate in this thesis, cluster sizes can also be used a tracer for the orbital anisotropy profile of a galaxy.

To explore the assumption that tidal radii and limiting radii are equal, we utilize the globular cluster population of the Virgo giant M87. Unusually deep, high signal-to-noise images of M87 are used to determine the radius for approximately 2000 globular clusters. To compare with these observations, we simulate a globular cluster population that has the same characteristics to the observed M87 cluster population. These characteristics include cluster radial distribution, mass distribution, central concentration distribution and line of

sight velocity dispersion. Placing these simulated clusters in the well-studied tidal field of M87, the orbit of each cluster is solved and the theoretical tidal radius of each cluster is determined. We compare the predicted relationship between cluster size and projected galactocentric distance found in our simulation to observations in order to test whether a cluster's tidal radius and limiting radius are equal. We find that for an isotropic distribution of cluster velocities, theoretical tidal radii are approximately equal to observed limiting radii. The simulation predicts the observed increase in cluster size with galactocentric distance, which is expected if tidal radii are dependent on the tidal field. Additionally, simulated cluster sizes are of the same order of magnitude as observed cluster sizes. However the simulation does underestimate cluster sizes in the inner regions of M87. To minimize the discrepancy between theory and observations, we further explore the effects of orbital anisotropy on cluster sizes, and suggest a possible orbital anisotropy profile for M87 which yields the best fit between theory and observations. Finally, we suggest multiple future studies which will aid in our understanding of tidal theory and in establishing a stronger link between tidal radii and limiting radii.

Acknowledgements

I would especially like to thank my parents and my sister Emily. Your support, guidance and encouragement over the years has been invaluable, and none of this would have been possible without you. For that and more, I am greatly in your debt.

I would like to thank my supervisors, Dr. Alison Sills and Dr. Bill Harris. Your ideas, encouragement, and enthusiasm have been inspiring. I have learned so much from the two of you, and am excited to continue working with you both. I would also like to thank my Master's committee member Dr. James Wadsley for both his time and extremely helpful suggestions and insight. Thanks as well goes to Dr. Gretchen Harris, for first giving me the opportunity to work in the field of astronomy, and for her help and support along the way. A similar thank you to Mr. Joe Strever, without whom I never would have considered working in the field of physics.

A big thank you also goes out to members of the Webb and Darrach families. You have each helped me in your own ways, and your constant support has been most appreciated. Special mention to Aunt Ro and Aunt Marg, who have both gone above and beyond on multiple occasions. Another thank you goes out to the Vercaigne family, you have been there and supported me for many years, and always make things easier whenever possible.

I would also like to thank a few people who have made the time it took to get here an enjoyable one. My roommate and travelling companion for the past 6 years, who has made the best of out every situation we have been in. My research group members and friends at McMaster, who have made the last two years a great experience. Jer Nicholson, Cait Mckee, and the rest of The Everett for making every time we see each other like we hung out yesterday. Kyle Johnston for his

friendship, interest, and support through undergrad and beyond. Chris Coulter and James Elliot, for their uncanny ability to drop whatever they are doing to hang out, whenever the word is given. Andrew Packer, for counter attacks, always keeping the pace, and never ever forgetting about cold fusion. And his wife Elena, for her unwavering interest in all things astronomy. Dave and Amber Patchett, your friendship knows no bounds, and your constant support and interest has been greatly appreciated. Chris Godwin, you consistently go above and beyond the call of duty, and I could not ask for a better friend.

To Megan Vercaigne, listing the ways how you have supported, encouraged, and been there for me would double the size of this thesis. I know that I would not be where I am or who I am today if not for you, and this thesis would definitely not have been possible. You have been with me every step of the way and never once could I have asked for anything more. You cannot be thanked enough.

And just in case it is not said as often as it should be, thanks again Mom and Dad.

Table of Contents

List of Figures

List of Tables

Chapter 1

Introduction

1.1 Globular Clusters

Globular clusters are almost spherical, gravitationally bound collections of 10^4 to 10^7 old stars. Classic globular clusters do not contain any gas, dust, dark matter, or young stars (Binney & Tremaine, 2008). They are believed to be very old, forming around the same time as their host galaxy. Current estimates of mean cluster age for old Milky Way globular clusters are on the order of 13 Gyr (e.g. Marín-Franch et al., 2009; Dotter et al., 2010). Globular clusters are found orbiting in all types of galaxies, ranging from the Milky Way which contains approximately 150 globular clusters (Harris, 1996 (2010 Edition)) orbiting in the galactic halo to galaxies like M87 which contain about 13000 clusters (Tamura et al., 2006).

Observationally it is possible to determine many globular cluster parameters, including galactocentric distance, magnitude (brightness), colour, metallicity (mass fraction of elements heavier than helium), and structural parameters like cluster core radius (where the surface brightness falls to half its central

value), effective radius (radius which contains half of the cluster's luminosity), and tidal radius. There exists a rich literature which explores the connections among all of these parameters (e.g. Brodie & Strader, 2006; Djorgovski & Meylan, 1994). For Milky Way globular clusters, these parameters and more can be found in the recently updated catalog of Harris (1996) (2010 Edition). Since globular clusters likely formed at the same time as the host galaxy or through merger events, the properties of clusters contain information regarding not only the formation and evolution of globular clusters themselves, but of the host galaxy as well. More specifically, globular clusters can be used as tracers for galaxy formation.

Not only can globular clusters be found in all types of galaxies, but they tend to have many similar properties. In the Milky Way, we see that the globular cluster luminosity function (Figure 1.1) can be approximated by a Gaussian symmetric about a visual magnitude of -7.3, with a standard deviation of 1.3 (e.g. Brodie & Strader, 2006). This observation is not only true for the Milky Way, but for globular cluster populations in all other galaxies as well.

Also consistent between different galaxies is the fact that globular clusters all have a mean effective radius of approximately 2.5-3 pc (Binney & Tremaine, 2008). This is illustrated for the Milky Way globular cluster population in Figure 1.2, with the vertical line marking the peak at 2.5 pc. Additionally, cluster populations have metallicity distributions which are bimodal (Figure 1.3), indicating the presence of two distinct sub-populations. More specifically, clusters appear to either have a low metallicity (blue) or a high metallicity (red)

(Brodie & Strader, 2006). These similarities between populations indicate that globular clusters in different galaxies may share a common formation mechanism and have similar stages of evolution.

This study is aimed at investigating the characteristic scale sizes of individual globular clusters, and what exactly governs the sizes clusters can reach. Historically it has been assumed that the gravitational field of the host galaxy regulates cluster sizes (e.g. von Hoerner, 1957; King, 1962; Innanen, Harris, & Webbink, 1983; Binney & Tremaine, 2008; Bertin & Varri, 2008). Essentially if a star is capable of reaching a distance far enough from the cluster center such that it feels a stronger gravitational attraction towards the host galaxy, it will be stripped from the cluster. If this assumption is true, one should be able to predict the size of a globular cluster based on its location within the gravitational field of a galaxy. Hence the sizes of globular clusters should have an observable trend with galactocentric distance. This study will compare the theoretically calculated and observationally determined sizes of globular clusters to see whether the gravitational field of a galaxy is truly responsible for limiting cluster sizes, or whether other factors play a role.

1.2 Globular Cluster Tidal Radii

The size of a globular cluster is more commonly referred to as the tidal radius. The tidal radius has both a theoretical and observational definition.

Theoretically, the tidal radius is better known as the Jacobi radius. The Jacobi radius of a globular cluster is the radius at which a star feels an acceleration toward its host globular cluster that is equal in magnitude but opposite

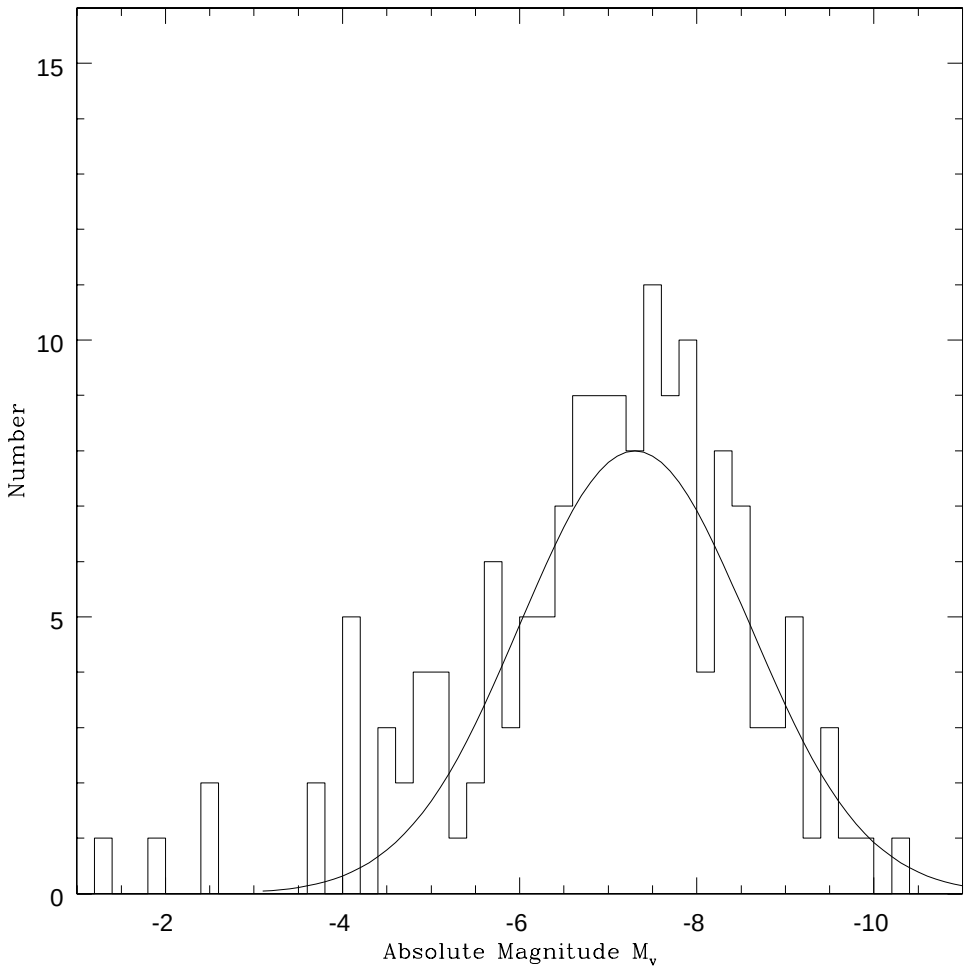

Figure 1.1: Globular cluster luminosity function for Milky Way globular clusters. The solid line is a Gaussian centered at -7.3 with a standard deviation of 1.3 (Brodie & Strader, 2006). Data taken from Harris (1996) (2010 Edition).

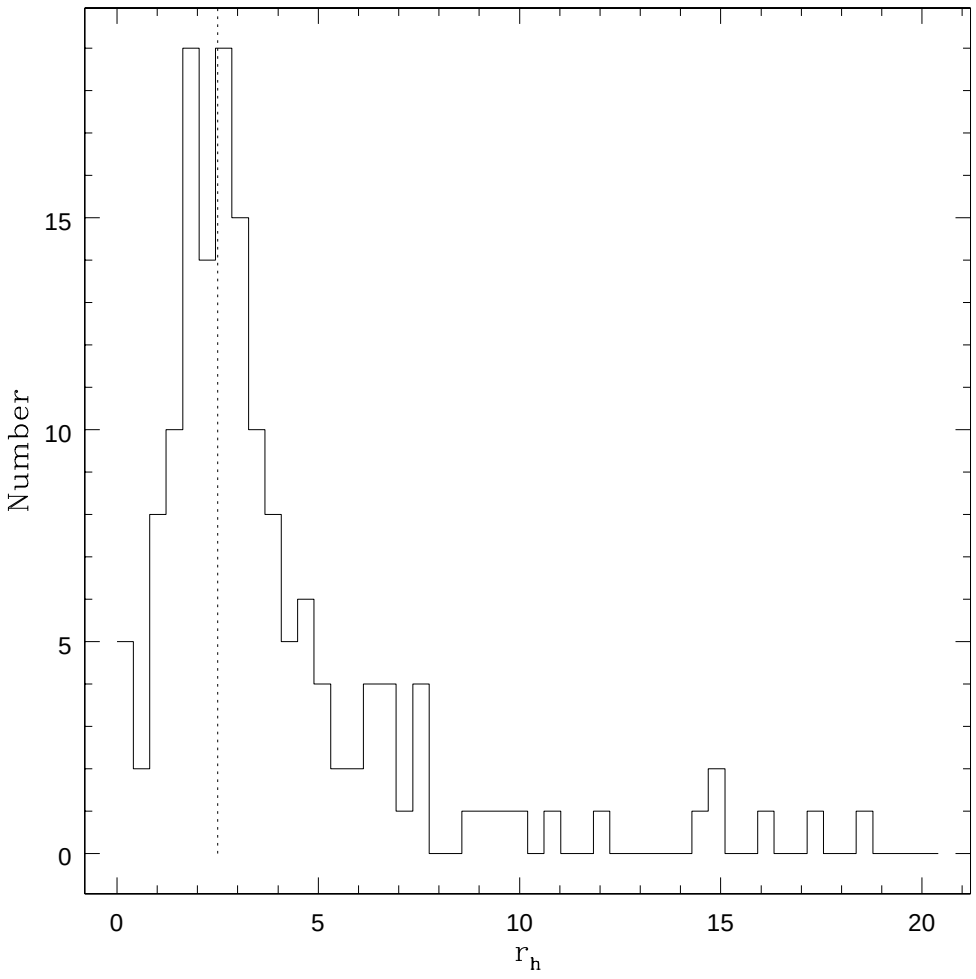

Figure 1.2: Effective radius distribution for Milky Way globular clusters. The dotted line represents an effective radius of 2.5 pc. Data taken from Harris (1996) (2010 Edition).

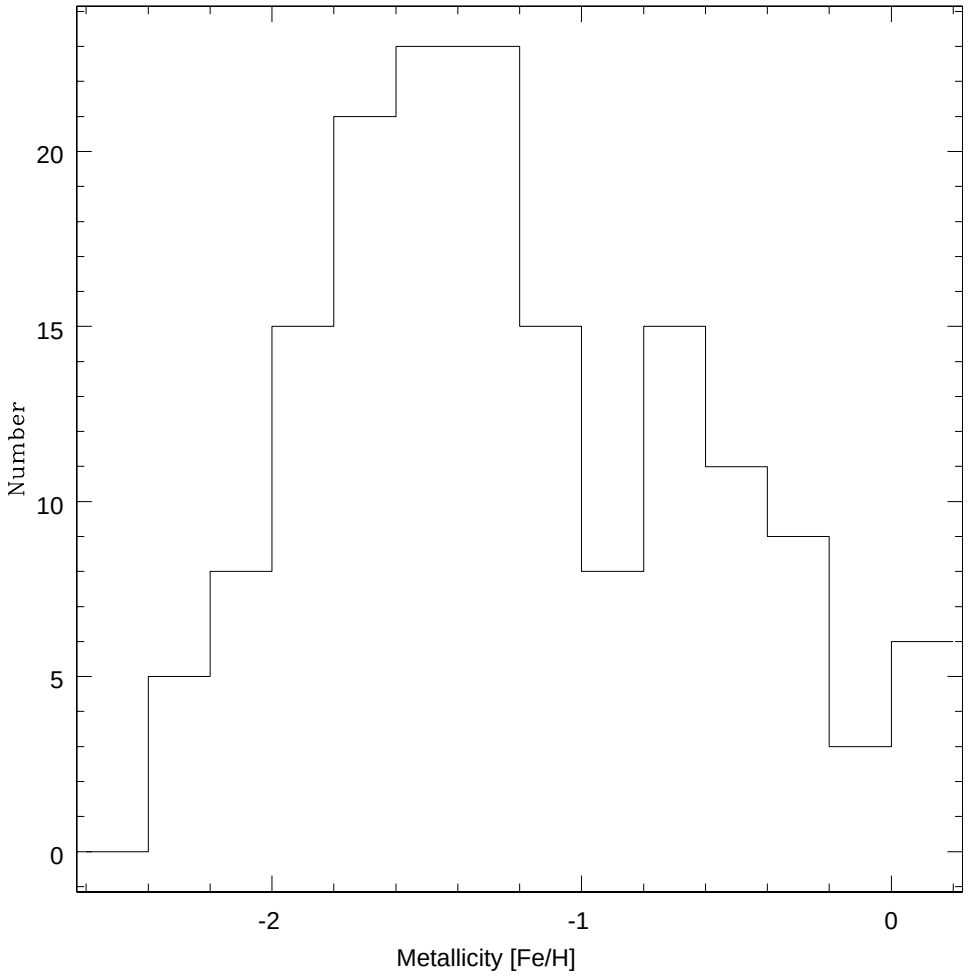

Figure 1.3: Metallicity distribution for Milky Way globular clusters. Data taken from Harris (1996) (2010 Edition).

in direction to the acceleration felt towards the cluster's host galaxy (von Hoerner, 1957). It marks the distance that past which, a star will no longer be bound to the globular cluster and will escape to join the field stars of the galaxy. Unfortunately there exist multiple mathematical definitions of where exactly the Jacobi radius of a cluster is located, due to the fact that tidal theory is not well understood and different definitions make different assumptions. However, these definitions all assume that the gravitational potential, or tidal field, of the host galaxy is responsible for regulating cluster size. For example, a cluster located near the center of a galaxy will be deep inside the tidal field. Being subject to a strong tidal field, the cluster will be small in size as the galaxy is able to strip stars that are only a small distance from the cluster's center. On the other hand, a cluster that is located far from the galaxy center will be subject to a much weaker gravitational field. This allows stars to travel far from the cluster center while still remaining bound to the cluster. For clusters with elliptical orbits, it is assumed that the Jacobi radius is imposed at the point of closest approach to the galaxy center, where the tidal field is the strongest. This assumption is based on the fact that cluster orbital periods are less than cluster internal relaxation times. The internal relaxation time is the time it takes for the encounters between the stars in a cluster to significantly change their velocities. If a cluster was able to relax before completing a full orbit, it is possible that changes in stellar velocities could result in bound stars orbiting at distances larger than the cluster's tidal radius, as calculated at perigalacticon. As long as a cluster returns to perigalacticon before it is able to relax, the assumption that cluster size is imposed at perigalacticon is believed to be valid.

An observer usually refers to the tidal radius of a cluster as the limiting radius. The limiting radius of a globular cluster is "the outer limit of the cluster where the density drops to zero" (Binney & Tremaine, 2008). For a Milky Way globular cluster it may be possible to determine which stars are members of the cluster and call the distance to the most remote one the tidal radius. But for clusters in other galaxies, the only way of defining the exact size of a cluster is to examine its density profile, or surface brightness profile. A surface brightness profile is a projection of a cluster's brightness as a function of distance from its center. Projecting where the density profile or brightness profile will reach zero is the only method of determining the tidal radius of globular clusters in other galaxies. This is done by fitting observed profiles to accepted models.

Based on the theoretical definition of cluster tidal radius, it is clear that cluster sizes could be used as tracers of mass distribution within a galaxy. This is especially useful for mapping the dark matter halo of a galaxy. Cluster sizes have also been linked to the orbital anisotropy of the stars within the host galaxy. Orbital anisotropy is a measure of what type of orbit is preferred in a population. Since tidal radii are believed to be imposed at perigalacticon, a cluster's orbit will play an important role in governing cluster sizes. For a tangentially anisotropic population, clusters will preferentially have more nearly circular orbits. Hence their galactocentric distance will always be close to perigalacticon. However for a radially anisotropic population, clusters will have very eccentric orbits bringing them very close to the galaxy center when at perigalacticon. Having travelled deep into the tidal field of the galaxy, we expect radially anisotropic populations to have smaller tidal radii as opposed

to tangentially anisotropic populations with clusters that remain more or less at the same mean galactocentric distance.

However, before we can use observations of clusters to make conclusions about the host galaxy's mass distribution and anisotropy profile, it must first be established that the observed tidal radius of a globular cluster is the same as the theoretical tidal radius of a cluster, as imposed by a tidal field. While it is generally assumed that these two radii are the same, recent studies are finding that this assumption is not entirely true, and requires modification. Brosche, Odenkirchen, & Geffert (1999) and Kupper et al. (2010) both found that using a cluster's perigalactic distance to calculate its tidal radius is likely incorrect, and yields an underestimation of cluster size. Baumgardt et al. (2010) found that some Milky Way clusters are tidally-underfilling, which suggests some clusters will have observational and theoretical sizes that are not in agreement. Through the use of N-body simulations, Gieles & Baumgardt (2008) found that cluster internal relaxation can lead to clusters underfilling their tidal radius, which would also yield a disagreement between theoretical and observational cluster sizes. We aim to explore this assumption that theoretical and observational tidal radii are the same by directly comparing the relationship between cluster size and galactocentric distance for both an observed and simulated cluster population.

In order to study the relationship between the theoretical and observational tidal radii, a cluster population is needed which must meet specific requirements. For theoretical tidal radii calculations, we require the globular cluster population to reside in a galaxy with a well-defined mass distribution that

is spherically symmetric. To determine observational tidal radii, well-resolved globular clusters are necessary to accurately fit cluster observations with model surface brightness profiles. It is also required that the population contain a large number of globular clusters to make any findings statistically relevant. The galaxy M87 meets all of these requirements.

1.3 The Giant Elliptical Galaxy M87

M87 is a giant elliptical galaxy located 17 Mpc from the Milky Way, at the center of the Virgo galaxy cluster. Elliptical galaxies are classically smooth, featureless systems with little to no evidence of cool gas, dust, or a stellar disk (Binney & Tremaine, 2008). M87 is best known for the large jet of matter being ejected from its central black hole. However, it is also an excellent candidate for studying globular clusters. The primary reason is that M87 hosts the largest population of globular clusters of any galaxy in the local universe, providing a statistically significant number of clusters to any study. Hence any individual clusters that may have a unique formation or evolution history will have a minimal effect on any trends observed regarding the population as a whole. Furthermore, globular clusters can be observed out to large galactocentric distances because the foreground reddening and field contamination are low (Tamura et al., 2006).

The large population of clusters in M87 has led to the cluster population being heavily studied. With respect to cluster sizes, more recent studies include Kundu et al. (1999), who determined cluster size using WFPC2 images of the inner region of M87 and Jordán et al. (2005), who made use of the ACS

Virgo Cluster Survey to determine effective radii for thousands of globular clusters within Virgo, including M87. The most recent work is that of Madrid et al. (2009), who used HST observations to determine the effective radius of approximately 2000 of M87's globular clusters. All three of these studies find that globular cluster size increases with galactocentric distance, as one might expect if cluster size is dependent on tidal field.

For the purpose of determining observational and theoretical cluster tidal radii, M87 is an excellent fit for multiple reasons. Observationally, there exist Hubble Space Telescope (HST) images of M87 which are perhaps the best data available for accurate measurements of the radius of globular clusters in other galaxies. The unusually deep, high signal-to-noise images contain nearly 2000 of its globular clusters. From a theoretical point of view, the gravitational field which is required for the calculation of a cluster's tidal radius, is better known for M87 then for any other giant elliptical galaxy (McLaughlin, 1999). Essentially, M87 provides the best available test bed for comparing theoretical and observational tidal radii.

1.4 Thesis Objectives

This thesis will test whether the theoretically determined Jacobi radius of a cluster is equal to the observed limiting radius and will determine whether the observational trend of cluster tidal radius versus projected galactocentric distance matches the predicted trend from basic tidal theory. The giant elliptical galaxy M87 will be used as a test bed to perform this comparison between theory and observations. In Chapter 2 we first explore the history of the

theoretical calculation of a cluster's tidal radius, and specifically derive the relationship between a cluster's tidal radius and the tidal field of its host galaxy we will be using to calculate tidal radii. Second, we outline the models which will be used to fit the surface brightness profiles of observed globular clusters in M87. In Chapter 3 we will actually fit the observed surface brightness profiles of M87 globular clusters with each of the models, determine the tidal and effective radii of each cluster, and establish the observed trend between cluster size and galactocentric distance. If cluster sizes are truly dependent on the tidal field of the galaxy, we will in general expect cluster sizes to increase with galactocentric distance, as the tidal field of the galaxy gets weaker. While this is known to be true, we must establish the trend for M87 to compare with theory. In Chapter 4, we make use of observationally determined parameters of the M87 cluster population including the line of sight velocity dispersion, and mass and radial distributions to simulate a theoretical cluster population. Using the gravitational field of M87, we can determine each cluster's perigalactic distance and calculate a theoretical relationship between cluster size and galactocentric distance. Projecting the simulated clusters onto a two dimensional plane, we will then have a theoretical relationship between cluster size and projected galactocentric distance that is purely due to the tidal field of the galaxy. The results of the simulation are then compared to the observational results of Chapter 3, which will indicate whether the assumption that a clusters Jacobi radius is equal to its observed limiting radius is valid. We will also explore the affects of varying orbital anisotropy on cluster size. In Chapter 5 we apply this technique of comparing theoretical and observational tidal radii to the cluster population of the Milky Way, as it is the only clus-

ter population for which we have three-dimensional information regarding the positions and orbits of individual clusters. Our conclusions and future work are then discussed in Chapter 6.

Bibliography

Baumgardt, H., Parmentier, G., Gieles, M., Vesperini, E., 2010, MNRAS, 401, 1832

Bertin, G. & Varri, A. L. 2008, ApJ, 689, 1005

Binney, J. & Tremaine, S. 2008, Galactic Dynamics, 2^{nd} edition (Princeton, NJ, Princeton University Press)

Brodie, J. P. & Strader, J. 2006, ARA&A, 44, 193

Brosche, P., Odenkirchen, M., Geffert, M. 1999, New Astron., 4, 133

Dotter, A., Sarajedini, A., Anderson, J., Aparicio, A., Bedin, L. R., Chaboyer, B., Majewski, S., Marín-Franch, A., Milone, A., Paust, N., Piotto, G., Reid, I. N., Rosenberg, A., Siegel, M., 2010, ApJ, 708, 698

Djorgovski, S. & Meylan, G. 1994, AJ, 108, 1292

Gieles, M. & Baumgardt, H. 2008, MNRAS, 389, L28

Harris, W. E. 1996, AJ, 112, 1487, 2010 Edition

Harris, W.E. 2009, ApJ, 703, 939

Innanen, K. A., Harris, W.E., Webbink, R.F. 1983, AJ, 88, 338

Jórdan, A., Côté, P., Blakeslee, J. P., Ferrarese, L., McLaughlin, D. E. , Mei, S., Peng, E. W., Tonry, J. L., Merrit, D., Milosavljević, M., Sarazin, C. L., Sivakoff, G. R., West, M. J., 2005, ApJ, 634, 1002

King, I. R. 1962, AJ, 67, 471

Kundu, A, Whitmore, B. C., Sparks, W. B., Macchetto, F. D., Zepf, S. E., Ashman, K. M., 1999, ApJ, 513, 733

Kupper, A. H. W, Kroupa, P, Baumgardt, H., Heggie , D. C., 2010, MNRAS, 407, 2260

Madrid, J. P., Harris, W. E., Blakeslee, J. P., Gómez, M 2009, ApJ, 705, 237

Marín-Franch, A., Aparicio, A., Piotto, G., Rosenberg, A., Chaboyer, B., Sarajedini, A., Siegel, M., Anderson, J., Bedin, L. R., Dotter, A., Hempel, M., King, I., Majewski, S., Milone, A. P., Paust, N., Reid, I. N. 2009, ApJ, 694, 1498

McLaughlin, D. E. 1999, ApJ, 512, L9

Tamura, N., Sharples, R. M., Arimoto, N., Onodera, M., Ohta, K., Yamada, Y., 2006, MNRAS, 373, 601

von Hoerner, S. 1957, ApJ, 125, 451

Chapter 2

The Determination of Tidal Radii

Before we can begin comparing the theoretical and observational sizes of globular clusters, we must first explore how cluster sizes are determined. The possibility of a tidal cut-off was initially pointed out by von Hoerner (1957). Since then, it has been a continuing problem in astronomy to properly define what the tidal radius of a globular cluster is, how it can be calculated theoretically, and how it can be determined observationally.

2.1 History of the Theoretical Tidal Radius

The original derivation of a cluster's tidal radius by von Hoerner (1957) assumed that it is the tidal field of the host galaxy that is the primary source in regulating the maximum size a globular cluster can reach. For a globular cluster of mass M in an orbit around a galaxy of mass M_g at a distance R_g, consider a star within the globular cluster located a distance r from the cluster center, and is located directly between the cluster center and galaxy center with r $\ll R_g$. The star will be subject to acceleration toward both the cluster and the galaxy. The acceleration at R_g toward M_g is equal to

$$a_{gc} = \frac{GM_g}{R_g^2} \tag{2.1}$$

The acceleration at the location of the star is then

$$a_s = \frac{GM_g}{(R_g - r)^2} \tag{2.2}$$

with the difference being the net acceleration the star feels towards the galaxy, written below as a_g.

$$a_g = \frac{2GM_g r}{R_g^3} \tag{2.3}$$

The acceleration of the star towards the globular cluster is

$$a_c = \frac{GM}{r^2} \tag{2.4}$$

The tidal radius is then defined as the distance where $a_g = a_c$, beyond which a star will feel a stronger acceleration towards the galaxy and escape the globular cluster. From the equations above, the tidal radius can be written as

$$r_t = R_g(\frac{M}{2M_g})^{1/3} \tag{2.5}$$

However, as von Hoerner (1957) and later King (1962) point out, Equation 2.5 actually yields the instantaneous tidal radius of a globular cluster. One should actually use the perigalactic distance (R_p) of the cluster's orbit as

opposed to its present distance (R_g) to calculate the tidal radius as this is where the tidal field of the galaxy is felt the strongest by the cluster. It is assumed that internal relaxation is too slow to increase the size of the cluster between perigalactic passages (King, 1962). A more detailed derivation by King (1962) which takes this into account still follows the general trend $r_t \; \alpha \; R_p(M/M_g)^{1/3}$. However, since the perigalactic distances of globular clusters outside of the Milky Way are difficult to determine, the assumption must be made that a cluster's current distance is a small multiple of its perigalactic distance. More specifically, the cluster is assumed to have a circular orbit. Despite this assumption making tidal radii calculations less accurate, it is unavoidable.

The key disadvantage of the King (1962) and von Hoerner (1957) derivations is that the galaxy is assumed to be a point mass. Based on detailed observations of galaxies, this assumption is known not to be true. This has led to further derivations of cluster tidal radii which consider the mass distribution of the host galaxy.

Innanen, Harris, & Webbink (1983) provide a much more rigorous and thorough derivation of the tidal radius. An advantage of this derivation over King's is that it assumes $M(R_g) = M_0(R_g/R_0)^n$, where $M(R_g)$ is the enclosed mass of the galaxy at radius R_g and R_0 is an unspecified reference radius. For the n=0 case, they recover the solution presented by King (1962). Unfortunately the final form of the tidal radius relation is in terms of n, perigalactic distance of the cluster, and the galactocentric distance the globular cluster would have assuming it has the same energy but with a circular orbit. The n dependence can make it difficult for mass distributions which do not resemble

a power law, and the latter point makes it difficult to use this equation with observational data.

Binney & Tremaine (2008) determine their version of the tidal radius by looking at the restricted three-body problem, "finding the trajectory of a massless test particle that orbits in a combined gravitational field of two masses." A galaxy of mass M and a globular cluster of mass m on a circular orbit at a distance R_g from the center of the galaxy will rotate around their common center of mass with angular speed

$$\Omega = \sqrt{\frac{G(M+m)}{R_g^3}} \tag{2.6}$$

A star orbiting a distance x from the center of mass in the combined effective potential of the galaxy and cluster (Φ_{eff}) will have an energy

$$E_J = \frac{1}{2}v^2 + \Phi_{eff}(x) \tag{2.7}$$

where E_J is known as the Jacobi integral, which is a conserved quantity. Since $v^2 \geq 0$, a star with E_J will never be able to pass into a region with $\Phi_{eff} > E_J$. This defines a zero-velocity surface for stars with E_J as a star must have a velocity of zero to reach a distance x such that $\Phi_{eff}(x) = E_J$. To better quantify Φ_{eff}, a coordinate system is selected such that the center of mass of the system is located at the origin, the galaxy is located at $\vec{x_M} = [\frac{-mR_g}{M+m}, 0, 0]$ and the cluster is located at $\vec{x_m} = [\frac{MR_g}{M+m}, 0, 0]$. For a star bound to the globular cluster and located a distance x from the center of mass, $\Phi_{eff}(\vec{x})$ can be written as

$$\Phi_{eff}(\vec{x}) = -G[\frac{M}{|\vec{x} - \vec{x_M}|} + \frac{m}{|\vec{x} - \vec{x_m}|} + \frac{1}{2}|\Omega \times \vec{x}|^2] \tag{2.8}$$

With Equation 2.8, we can draw contours of effective potential for the two masses in a circular orbit which represent zero-velocity surfaces (Figure 2.1)

Examining the contour lines about the globular cluster (m), it can be seen that the nearby zero-velocity surfaces surround only the globular cluster, but farther out the surfaces surround both the cluster and the galaxy. Therefore there exists a critical value of Φ_{eff} which corresponds to the last zero-velocity surface that encloses just the globular cluster, which is drawn in red on Figure 2.1. The final closed surface is known as the tidal or Roche surface of the cluster, and the distance to this surface is known as the Jacobi radius (r_J).

Noting that at the Jacobi radius the effective potential has a saddle point, a condition arises such that

$$\frac{d\Phi_{eff}}{dx}_{(x_m - r_J, 0, 0)} = 0 \tag{2.9}$$

This ultimately results in the Jacobi radius being written as

$$r_J = (\frac{m}{3M})^{\frac{1}{3}} R_g \tag{2.10}$$

similar to the previous derivations of von Hoerner (1957), King (1962), and Innanen, Harris, & Webbink (1983).

Unfortunately all these derivations are limited, as they do not match the observations. Assuming a simple galaxy mass distribution $M(R_g) \propto R_g$, Equa-

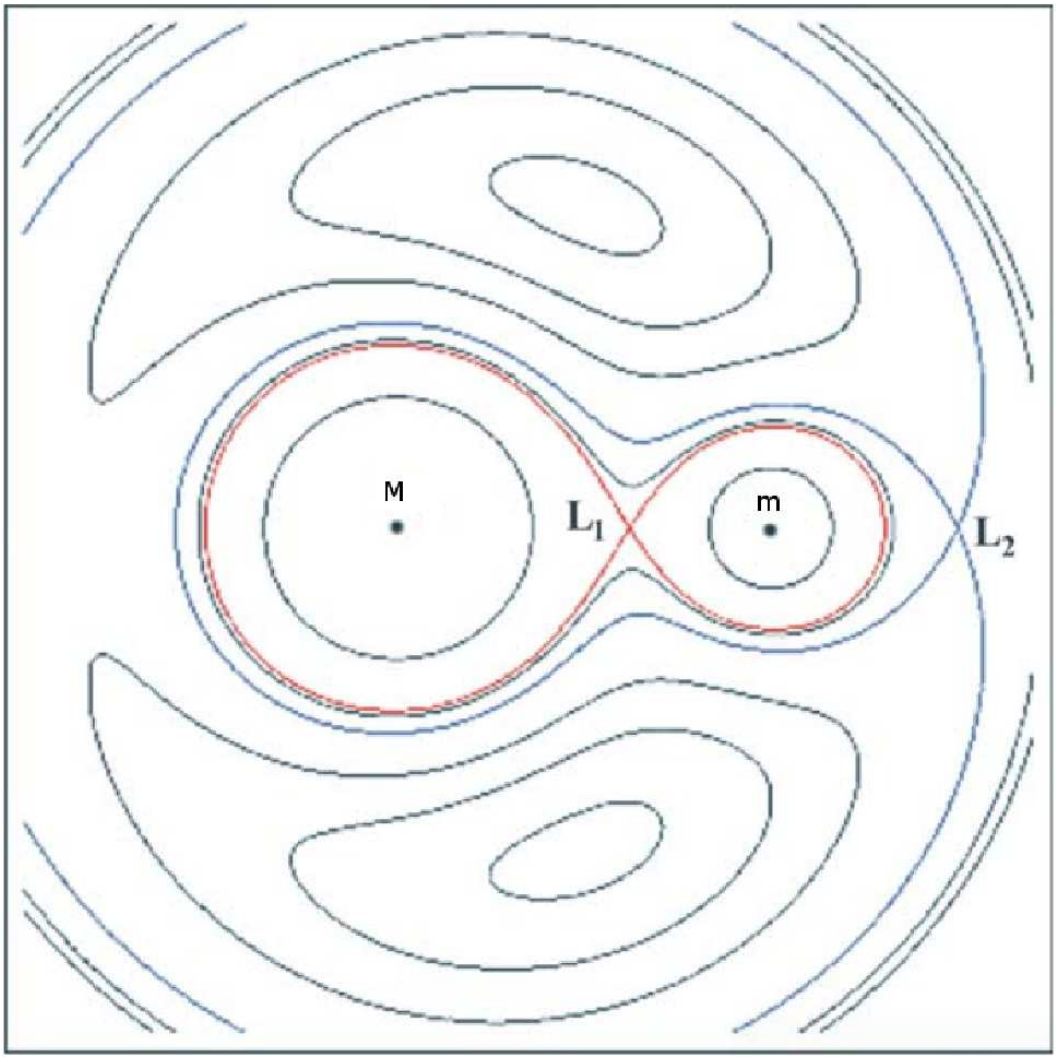

Figure 2.1: Contours of equal effective potential Φ_{eff} defined by Equation 2.8 for a galaxy (M) and a globular cluster (m) in a circular orbit. The red line marks the outermost contour which fully encloses the globular cluster. This image was taken from Skelton & Smits (2008).

tion 2.5 suggests that $r_t \propto R_g^{\frac{2}{3}}$. This result is also reached for King (1962),Innanen, Harris, & Webbink (1983), and Binney & Tremaine (2008) tidal radii. Observationally, the tidal radii of globular clusters do not increase this rapidly, suggesting that either the assumption that $M(R_g) \propto R_g$ is incorrect or further work is required in theoretically explaining a globular cluster's tidal radius. However, given that in many galaxies, including the Milky Way (Binney & Tremaine, 2008) it is observed that the circular speed as a function of radius is constant at larger radii, the basic assumption that $M(R_g) \propto R_g$ is validated.

2.2 The Bertin and Varri (2008) Tidal Radius

Bertin & Varri (2008) consider the center of mass of a globular cluster moving on a circular orbit of radius R_0 and orbital frequency Ω, and focus on the motion of stars inside the globular cluster. Under the assumption that the cluster has a circular orbit, it will always be located at its perigalactic distance. The galaxy is then modeled by means of a frozen gravitation field. The important difference to note between the restricted three-body problem and the Bertin & Varri (2008) derivation is that the secondary mass (globular cluster) is not treated as a point mass but as a stellar system with a cluster mean-field potential Φ_C.

Assuming the galactic potential $\Phi_G(R)$ is spherically symmetric, R is taken to be $\sqrt{X^2+Y^2+Z^2}$ where X,Y, and Z are with respect to the center of the galaxy. The orbital frequency Ω of the cluster is then taken from $\Omega^2 = (d\Phi_G(R)/dR)_{R_0}/R_0$. It is further assumed that the X-Y plane is the orbital plane of the globular cluster.

Bertin & Varri (2008) then introduce a local frame of reference which rotates at the orbital frequency of the cluster (Ω), with the origin located at the center of mass of the cluster. The x-axis is taken to point away from the center of the galaxy, the y-axis follows the direction of cluster rotation around the galaxy, and the z-axis is perpendicular to the orbital plane. The Lagrangian which describes the motion of a star bound to the globular cluster is:

$$\begin{aligned} Ł =& \frac{1}{2} \left(\dot{x}^2 + \dot{y}^2 + \dot{z}^2 + \Omega^2 \left[(R_0 + x)^2 + y^3\right]\right. \\ & \left. + 2\ \Omega\ (R_0 + x)\ \dot{y} - 2\ \Omega\ \dot{x}\ y\right) \\ & - \Phi_G(R) - \Phi_C(x, y, z) \end{aligned} \tag{2.11}$$

with $R = \sqrt{(R_0 + x)^2 + y^2 + z^2}$ and R_0 being the previously defined circular orbit radius of the globular cluster.

The cluster's equation of motion in an arbitrary direction q, can be determined from the Lagrangian via

$$\frac{d}{dt}\ (\frac{dŁ}{d\dot{q}}) = \frac{dŁ}{dq} \tag{2.12}$$

The resulting equations of motion in the x, y, and z directions are

$$\ddot{x} - 2\ \Omega\ \dot{y} - (4\ \Omega^2 - \kappa^2)\ x = \frac{-d\Phi_C}{dx} \tag{2.13}$$

$$\ddot{y} + 2\ \Omega\ \dot{x} = \frac{-d\Phi_C}{dy} \tag{2.14}$$

$$\ddot{z} + \Omega^2 \ z = \frac{-d\Phi_C}{dz} \tag{2.15}$$

with $\kappa^2 = 3\Omega^2 + (d^2\Phi_G/dR^2)_{R_0}$. κ is the epicyclic frequency at R_0. Cluster orbits are described by first setting the cluster to orbit around a small ellipse, with angular frequency κ. The center of the small ellipse then orbits around the center of the galaxy, with angular frequency Ω (Binney & Tremaine, 2008). Hence the epicyclic frequency refers to the frequency κ of a cluster's orbit around the small ellipse.

From Binney & Tremaine (2008), the momentum is

$$p = \frac{-d\text{Ł}}{d\dot{x}} \tag{2.16}$$

and the Hamiltonian is defined as

$$\begin{aligned} H &= p\dot{x} - L \\ &= \frac{p^2}{2} + \Phi - \Omega_b L \end{aligned} \tag{2.17}$$

where Ω_b is the angular velocity the reference frame must rotate at such that the potential is static. In the case of a cluster orbiting in the potential of a galaxy, Ω_b is the orbital frequency of the cluster (Ω).

The Jacobi integral (H_J) is then defined as

$$H_J = H - \Omega_b \cdot L \tag{2.18}$$

Since the potential is constant in the rotating frame, H_J will have no time dependence. Therefore, while neither H or L is conserved, the combination $H_J = H - \Omega_b \cdot L$ is a conserved quantity (Binney & Tremaine, 2008).

From the equations of motion above, the Jacobi integral is determined to be:

$$H_J = \frac{1}{2}(\dot{x}^2 + \dot{y}^2 + \dot{z}^2) + \Phi_T + \Phi_C \tag{2.19}$$

where the tidal potential $\Phi_T = \frac{1}{2}\,\Omega^2\,(z^2 - \upsilon\,x^2)$. The variable υ is a positive dimensionless coefficient equal to $4 - \kappa^2/\Omega^2$.

Similar to the Binney & Tremaine (2008) derivation, the tidal radius is the distance to the last closed zero-velocity surface surrounding the globular cluster. Since the final closed surface passes through a minima of the combined effective potential of the cluster and the galaxy, the distance to this surface can be determined with the condition:

$$\frac{d\Phi}{dx}(r_T, 0, 0) = 0 \tag{2.20}$$

The next step is to assume a potential for the globular cluster. If we assume that the potential of the cluster is Keplerian ($\Phi_C = -GM/r$), the combined potential can be written as:

$$\begin{aligned} \Phi(r) &= \Phi_C(r) + \Phi_T(r) \\ &= -GM/r + \frac{1}{2}\,\Omega^2\,(z^2 - \upsilon x^2) \end{aligned} \tag{2.21}$$

The assumption that the cluster has a Keplerian potential is only valid because we are concerned with the potential a star feels at the cluster's tidal radius. At the tidal radius, the enclosed mass will be the entire mass of the cluster. From Newton's second theorem (Binney & Tremaine, 2008) we know that the gravitational force felt by a star at the tidal radius due to the mass of the cluster is the same as if all the cluster's mass was concentrated at a single point located at the center of the cluster. Since a Keplerian potential is the potential due to a point mass, the assumption is valid.

Utilizing Equation 2.20, the tidal radius is then determined to be:

$$r_t = (\frac{GM}{\Omega^2 \upsilon})^{1/3} \tag{2.22}$$

Where Ω, κ and υ were previously defined as:

$$\Omega^2 = (d\Phi_G(R)/dR)_{R_0}/R_0 \tag{2.23}$$

$$\kappa^2 = 3\Omega^2 + (d^2\Phi_G(R)/dR^2)_{R_0} \tag{2.24}$$

$$\upsilon = 4 - \kappa^2/\Omega^2 \tag{2.25}$$

The relation is useful because it presents the tidal radius in terms of globular cluster mass and galactocentric distance, and does not make any unrealistic assumptions. The only constraint placed on the gravitational potential field of the host galaxy is that it must be spherically symmetric. For the case where the cluster's orbit is not circular, the perigalactic distance can be used in Equation 2.22 as opposed to R. If the perigalactic distance cannot be determined, the present distance can be assumed to be a small multiple of the perigalactic

distance. This will of course result in a less accurate tidal radius calculation. Recent studies (e.g. Brosche, Odenkirchen, & Geffert, 1999; Kupper et al., 2010) have found that using a cluster's perigalactic distance to determine its tidal radius is likely incorrect, and that instead some sort of orbit averaged distance will result in a more accurate tidal radius. However, for the purposes of this discussion we use the assumption that the tidal radius is imposed at perigalacticon.

It can be shown that a cluster's Jacobi radius as defined by Bertin & Varri (2008) (Equation 2.10) is a form of Equation 2.22 if we assume the host galaxy is a point source of mass M_g, and the galactic potential is Keplerian ($\Phi_G = -\frac{GM_g}{r}$). For a globular cluster of mass M located a distance R_g from the center of the galaxy, we find that

$$\Omega^2 = \frac{GM_g}{R_g^3} \tag{2.26}$$

$$\kappa^2 = \frac{GM_g}{R_g^3} \tag{2.27}$$

$$\upsilon = 3 \tag{2.28}$$

Substituting Ω^2, κ^2, and υ into Equation 2.22, we find

$$r_t = R_g(\frac{M}{3M_g})^{1/3} \tag{2.29}$$

which is equal to Equation 2.10.

2.3 Measuring Tidal Radii

Equation 2.22 provides a method for calculating the tidal radius of a globular cluster based on its perigalactic distance, its mass, and the gravitational potential field of the host galaxy. Observationally, this is not an ideal relation. The gravitational field of a galaxy is a difficult function to determine, as it requires the combination of many different types of observations out to large galactocentric distances. Hence for a galaxy that is not the Milky Way, the gravitational field is rarely known. Additionally, the perigalactic distance of a globular cluster outside of the Milky Way is impossible to determine. Not only is an observer forced to use a cluster's present distance instead of its perigalactic distance, but observations are subject to projection effects. Projecting a cluster's three-dimensional location on to the two dimensional plane of the sky further increases the amount of uncertainty in the cluster's true three dimensional position. For these reasons, observers do not use any of the mathematical relations previously discussed to determine observational tidal radii. Instead, observers turn to analytical models.

The most commonly used method of determining the tidal radius of a globular cluster is through a King (1966) model (hereafter K66 model). A K66 model is a dynamical model of a star cluster which is spatially limited, corresponding to a tidal cutoff imposed by the host galaxy. The projected density distribution of K66 models are similar to observed distributions in open clusters, globular clusters, and elliptical galaxies. By matching a K66 model to the observed brightness distribution of a globular cluster, the tidal radius can be determined. This thesis will also fit the brightness distributions

of globular clusters to King (1962) models (hereafter K62 models), Wilson (1975) models (hereafter W75 models), and Sérsic (1968) models (hereafter S68 models). Comparing the results of all four models will indicate the uncertainty in each tidal radius measurement. When comparing observations to theory, the assumption is made that the observed tidal radius deduced through model fitting is equal to the theoretical radius derived by Bertin & Varri (2008).

A disadvantage of using models to determine tidal radii is that the majority of observed stellar members of a globular cluster are in the inner regions of the cluster. The same can be said for brightness profiles where measurements near the center are far more accurate then measurements near the outskirts of the cluster. Hence the tidal radius located at the outermost point of a globular cluster is dependent on the distribution of stellar members within the inner regions. Unfortunately no methods are available to bypass this problem without having star counts out to a cluster's tidal radius. For clusters in the Milky Way, while using star counts to determine stellar distribution profiles is possible, background galaxies, quasars, dust extinction, foreground stars, and background stars all provide sources of uncertainty when determining cluster membership (Jordi & Grebel, 2010). Unfortunately, it is currently not possible to resolve individual stars within a cluster outside of the Local Group. Hence star counts cannot be used to determine cluster size.

2.3.1 The King (1962) Model

K62 models were published first in a series of papers by Ivan King entitled the Structure of Star Clusters (King, 1962). Stating that physically realistic

models regarding cluster structure are too complex and results from simpler models tend to reflect mathematical simplifications as opposed to physical realities, King used observations of 15 globular clusters to establish a spatial density law. This would in turn limit the range of possible dynamical models and possibly lead to a physically realistic globular cluster model (See Section 2.3.2).

Star counts in multiple globular clusters led King to a spatial density profile of the form

$$f = f_1(\frac{1}{r} - \frac{1}{r_t})^2 \tag{2.30}$$

where f is the number of stars per square arcminute, f_1 is a constant, and r_t is the value of r at which f reaches zero. Figures 2 and 3 in King (1962) illustrate how well Equation 2.30 fits for globular clusters M 15, ω Cen, 47 Tuc, and M 13. However, the central parts of a cluster are not expected to follow Equation 2.30 as it leads to infinite density at r=0.

In order to compensate for Equation 2.30 having f go to infinity as r goes to 0, examination of the inner parts of concentrated clusters led to a spatial density profile for the inner region of a cluster of the form

$$f = \frac{f_0}{1 + (\frac{r}{r_c})^2} \tag{2.31}$$

where f_0 is the central surface density and r_c is a scale factor that King denotes as the core radius. Combining Equations 2.30 and 2.31 leads to the K62 spatial density profile for globular clusters (Equation 2.32)

$$f = k(\frac{1}{[1+(\frac{r}{r_c})^2]^{\frac{1}{2}}} - \frac{1}{[1+(\frac{r_t}{r_c})^2]^{\frac{1}{2}}})^2 \tag{2.32}$$

where k is a scale factor. For smaller values of r/r_c, Equation 2.32 can be rewritten as

$$f_0 = k(1 - \frac{1}{[1+(\frac{r_t}{r_c})^2]^{\frac{1}{2}}})^2 \tag{2.33}$$

such that it is similar to Equation 2.31. For $r >> r_c$, Equation 2.32 becomes similar to Equation 2.30 in the form

$$f_1 = kr_c^2 \tag{2.34}$$

While K62 models are simply mathematical fits to globular cluster observations, they are much easier to work with than other complicated dynamical models, and often produce similar results.

2.3.2 The King (1966) Model

The King (1966) models were published as the third paper in King's Structure of Star Clusters series.

The main difference between the K66 and the K62 models is that the K66 models are dynamically motivated. As seen in Section 2.3.1, K62 models simply attempt to fit the observed data points, and are independent of any dynamical processes within a cluster. However, the generation of a density profile in a K66 model is based on the dynamical properties of the stars within

a globular cluster. Therefore once the appropriate K66 model has been fit to a cluster, much more information than a cluster's tidal radius can be taken from the data.

A collection of stars can be described by a distribution function $f(x, v, t)$, such that $f(x, v, t)dx^3dv^3$ is the probability that at time t a randomly chosen star will be in the phase space volume dx^3dv^3 (Binney & Tremaine, 2008). Here, x,v, and t are position, velocity, and time. The distribution function for a spherical isotropic distribution of stars in a static potential (no time dependence) can be written as

$$f(x, v) = k\ exp(\frac{-H(x, v)}{\sigma^2}) \tag{2.35}$$

where k is a normalization constant, σ^2 is a velocity scaling factor, and H is the Hamiltonian. The velocity scaling factor σ can be thought of as the radius of the sphere the stellar system occupies in velocity space. In a steady state potential $\Psi(x)$, the Hamiltonian is an integral of motion. That is to say its absolute time derivative is zero. The Hamiltonian is of the form

$$H(x, v) = \Psi(x) - \frac{1}{2}v^2 \tag{2.36}$$

For some constant Ψ_0, we can define a relative potential (ψ) and relative energy (ϵ) to be

$$\psi = -\Psi + \Psi_0 \tag{2.37}$$

$$\epsilon = -H + \Psi_0 = \psi - \frac{1}{2}v^2 \tag{2.38}$$

such that the distribution function can be written as

$$f(x,v) = k\ exp(\frac{\epsilon}{\sigma^2}) = k\ exp(\psi - \frac{1}{2}v^2) \tag{2.39}$$

In order to develop a distribution function for a globular cluster, we consider how we need to modify the distribution function of an isothermal sphere. At small radii, individual stars can have large values of the relative energy ϵ. Since the cluster potential is much stronger at small radii, stars can have a wide range of velocities and still remain bound. If we integrate the distribution function for an isothermal sphere over all space, we find the resulting velocity distribution to be Maxwellian (Equation 2.40) (Binney & Tremaine, 2008).

$$dn \propto exp(-\frac{|v^2|}{2\sigma^2})d^3v \tag{2.40}$$

From Equation 2.40, we see that the probability of a star having a high velocity is very low. More specifically, the probability of a star having the extremely high velocity it would need to escape the inner regions of a globular cluster is approximately zero. Therefore at small radii, a globular cluster can be taken to be isothermal as stars can have a large range of velocities and still remain bound to the cluster. However at larger radii, the cluster must become less dense, such that it has a finite size and mass. At these larger radii the potential is weaker, such that the relative energy ϵ becomes very small. This in turn limits the range of velocities a bound star can reach. At

the surface of the cluster, the potential and therefore the relative energy a star can have will be zero. Hence we can obtain a distribution function for a globular cluster by decreasing the distribution function of the isothermal sphere until the surface of the cluster is reached. On the surface of the cluster and beyond, the distribution function must equal zero.

By choosing Ψ_0 such that the relative energy ϵ equals zero on the cluster's surface, the resulting stellar distribution function will be of the form

$$f(x,v) = k(exp(\frac{\epsilon}{\sigma^2}) - 1) \tag{2.41}$$

where k is a constant (McLaughlin et al., 2008). Binney & Tremaine (2008) write this equation as

$$\begin{aligned} f_K(\epsilon) &= \frac{\rho_1}{(2\pi\sigma^2)^{\frac{3}{2}}}(exp(\frac{\epsilon}{\sigma^2}) - 1) \quad E > 0 \\ &= 0 \qquad\qquad\qquad\qquad\qquad\quad E \leq 0 \end{aligned} \tag{2.42}$$

where ρ_1 is a constant, and $f_K(x,v)$ defines the family of King models (King, 1966).

Continuing with the derivation of a K66 model from Binney & Tremaine (2008), the density distribution can be determined by integrating the distribution function over the entire range of velocities. At a given distance from the cluster's center, stellar velocities can range from 0 to the escape velocity, which is equivalent to $\sqrt{2\psi}$. Substituting $\epsilon = \psi - \frac{1}{2}v^2$ into Equation 2.42 and integrating over all velocities, the density in the globular cluster at any given radius is then

$$\begin{aligned}\rho_K(\psi) &= \frac{4\pi\rho_1}{(2\pi\sigma^2)^{\frac{3}{2}}}\int_0^{\sqrt{2\psi}} dv\ v^2[exp(\frac{\psi-\frac{1}{2}v^2}{\sigma^2})-1] \\ &= \rho_1[exp(\frac{\psi}{\sigma^2})\ erf(\frac{\sqrt{\psi}}{\sigma}) - \sqrt{\frac{4\psi}{\pi\sigma^2}}(1+\frac{2\psi}{3\sigma^2})]\end{aligned} \tag{2.43}$$

where $erf(x)$ is the error function. Poisson's equation ($\bigtriangledown^2\psi = 4\pi G\rho$), which relates cluster potential to cluster density, can be written as

$$\begin{aligned}\frac{d}{dr}(r^2\frac{d\psi}{dr}) = &-4\pi G\rho_1 r^2\ [exp(\frac{\psi}{\sigma^2})\ erf(\frac{\sqrt{\psi}}{\sigma}) \\ &- \sqrt{\frac{4\psi}{\pi\sigma^2}}(1+\frac{2\psi}{3\sigma^2})]\end{aligned} \tag{2.44}$$

A K66 model is then generated by integrating Equation 2.44 outwards from r=0, where $\frac{d\psi}{dr}$ is set to zero. The first parameter which makes one K66 model different from another is the value selected for the relative potential ψ at r=0 ($\psi(0)$). As r increases, ψ will decrease from $\psi(0)$, and the range of speeds that stars at a given radius can have will narrow as the escape velocity ($\sqrt{2\psi}$) becomes smaller and smaller. At the tidal radius of the cluster, ψ and the stellar density ρ will both equal zero. The potential at the tidal radius is then

$$\Psi(r_t) = -\frac{GM(r_t)}{r_t} \tag{2.45}$$

where the total enclosed mass $M(r_t) = 4\pi\int_0^{r_t} dr\ r^2\rho_K$. The central potential is then

$$\Psi(0) = \Psi(r_t) - \psi(0) \tag{2.46}$$

From Equation 2.46, we see that the larger the value of $\psi(0)$ that is selected to begin the integration of Equation 2.44, the larger the tidal radius, total enclosed mass, and central potential ($\Psi(0)$) of the cluster will be.

However while two clusters may be fit with K66 models which have the exact same $\Psi(0)$, they will not necessarily have the exact same density profile and tidal radius. The decrease in cluster potential with radius must be properly scaled as it goes from $\Psi(0)$ to zero. Therefore the second parameter which makes one K66 model different from another is known as the scaling radius or King radius r_0. The King radius is related to σ via

$$r_0 = \sqrt{\frac{9\sigma^2}{4\pi G\rho_0}} \tag{2.47}$$

where ρ_0 is the central density of the cluster. The King radius ends up being the radius at which the projected density of the globular cluster is approximately half (0.5013) of the central density (Binney & Tremaine, 2008). This has led to the King radius being commonly referred to as the core radius, which is the radius at which the projected density is exactly half of its central value. Therefore, by finding which values of $\Psi(0)$ and r_0 produce a K66 model that best fits an observed globular cluster, we are finding the value of the potential at the center of the cluster and the radius at which the surface brightness falls to half its central value (core radius). The resulting density profile can then be used to determine the tidal radius.

K66 models are often parameterized by r_0 and the central potential parameter $W_0 = \frac{\Psi(0)}{\sigma^2}$. However, observationally W_0 is a less meaningful quantity, so models can instead be parameterized by the more intuitive central concentra-

tion parameter c. The central concentration of a globular cluster is related to the core and tidal radii through Equation 2.48, and the correlation between central concentration and the dimensionless central potential W_0 is illustrated in Figure 2.2 (King, 1966).

$$c = \log(r_t/r_c) \tag{2.48}$$

2.3.3 The Wilson (1975) Model

A W75 model, similar to K66 models, is a dynamically motivated attempt to model the surface brightness distribution of a globular cluster. The motivation behind W75 models is that K66 models assume a spherically symmetrical mass distribution, while most elliptical galaxies and star clusters are non-spherical. This led Wilson (1975) to derive a dynamical model for a rotationally symmetrical but non-spherical stellar system.

Wilson (1975) begins with a potential that is time independent and rotationally symmetrical, such that the two isolating integrals of motion are the energy per unit mass (E) and the component of angular momentum per unit mass parallel to the symmetry axis (J). In spherical coordinates, the integrals of motion are

$$E = \frac{1}{2}(v_r^2 + v_\theta^2 + v_\phi^2) + U(r, \theta) \tag{2.49}$$

$$J = r(sin\theta)v_\phi \tag{2.50}$$

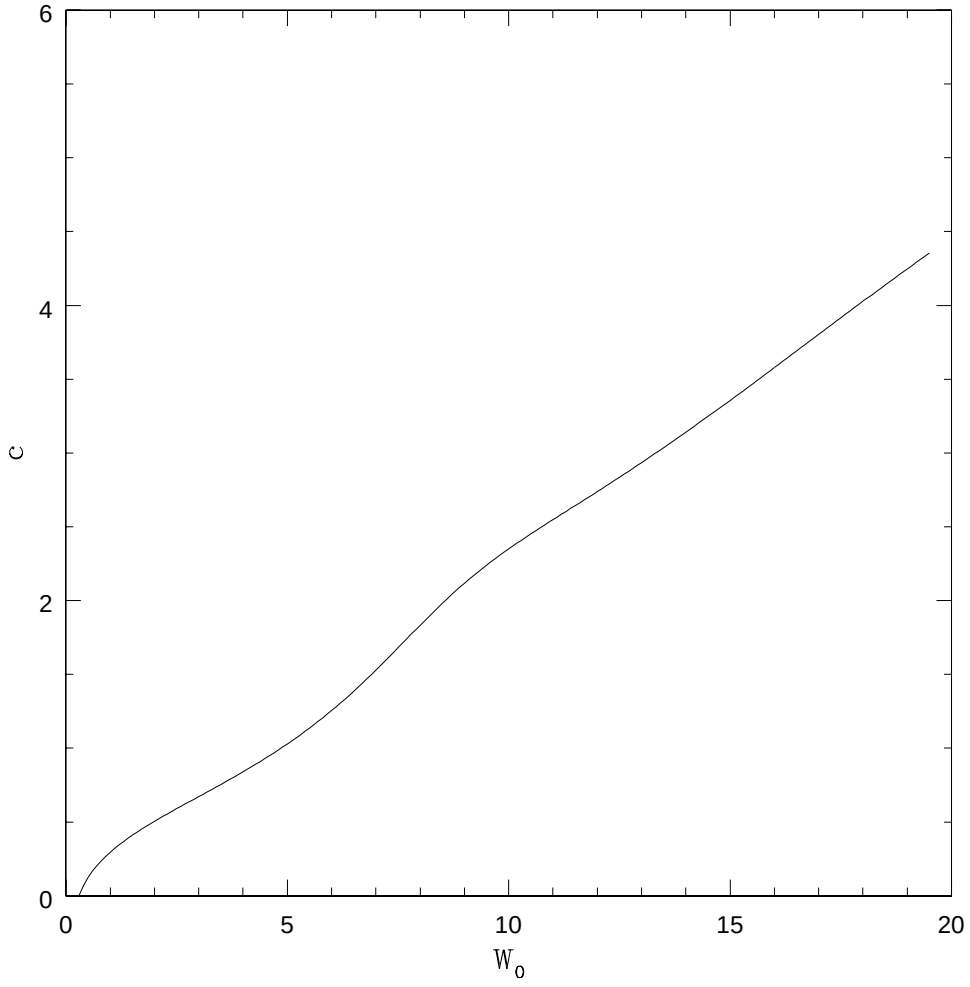

Figure 2.2: Relationship between cluster central concentration and the dimensionless central potential W_0. Data points taken from King (1966).

where U is the gravitational potential. The next step is then to assume a given distribution function F(E,J) and determine density via

$$\rho(rsin\theta, U) = \int\int_{-\infty}^{\infty}\int F(E,J)\, dv_r\, dv_\theta\, dv_\phi \tag{2.51}$$

The self-consistent model is then constructed by solving Poisson's equation ($(\bigtriangledown^2\psi = 4\pi G\rho)$, as seen in Section 2.3.2. The key difference between K66 and W75 models is the choice of distribution function. W75 chose a distribution of the form

$$\begin{aligned} F(E,J) &= (e^{-E} - 1 + E)\ exp[(\beta J - \frac{1}{2}\xi^2 J^2) \quad E \leq 0 \\ &= 0 \qquad\qquad\qquad\qquad\qquad\qquad\quad E > 0 \end{aligned} \tag{2.52}$$

where β is the angular velocity of the central region of the model and ξ is included to introduce differential rotation in a manner that is independent of the energy cutoff. For our purposes, we use W75 models in the case of a non-rotating system, such that J=0. Therefore Equation 2.52 reduces to

$$\begin{aligned} F(E,0) &= (e^{-E} - 1 + E) \qquad E \leq 0 \\ &= 0 \qquad\qquad\qquad\quad E > 0 \end{aligned} \tag{2.53}$$

The second order Taylor series expansion of e^{-E} is $1 - E + \frac{1}{2}E^2$, which allows us to rewrite the above equation as

$$\begin{aligned} F(E,0) &= \frac{1}{2}E^2 \qquad E \leq 0 \\ &= 0 \qquad\quad E > 0 \end{aligned} \tag{2.54}$$

The key difference between the W75 distribution function and the K66 distribution function is that the W75 function smoothly goes to zero. More specifically, as E goes to zero in Equation 2.54, F(E,0) smoothly goes to zero. The K66 distribution function has a sharp tidal cutoff at zero, which corresponds to the tidal radius of a cluster being marked as the point where the density sharply turns to zero. Since the W75 distribution function goes smoothly to zero, it suggests the tidal limit of a cluster is farther out than K66 models. Hence it is expected that the W75 tidal radius of a cluster will be larger than the K66 radius of a cluster. This is clear in Figure 2.3, which is a plot of luminosity surface density versus projected radius for K62, K66, W75, and S68 models with equal central potentials. We see that K62 (black), K66 (blue) , and S68 (cyan) models are all similar in shape, and predict a sharp decrease in luminosity surface density near the tidal radius. A W75 model on the other hand smoothly goes to zero. This will be explored in further detail when we fit models to observations in Chapter 3.

2.3.4 The Sérsic (1968) Model

A S68 model, perhaps better known as the Sérsic law, is an empirical formula that is often used to fit the surface brightness profiles of elliptical galaxies. Similar to K62 models, it has no dynamical motivations, and is simply a mathematical fit to observations. It has the general from

$$I_n(R) = I(0)exp(-kR^{\frac{1}{n}}) = I_e exp(-b_n[(\frac{R}{R_e})^{\frac{1}{n}} - 1]) \tag{2.55}$$

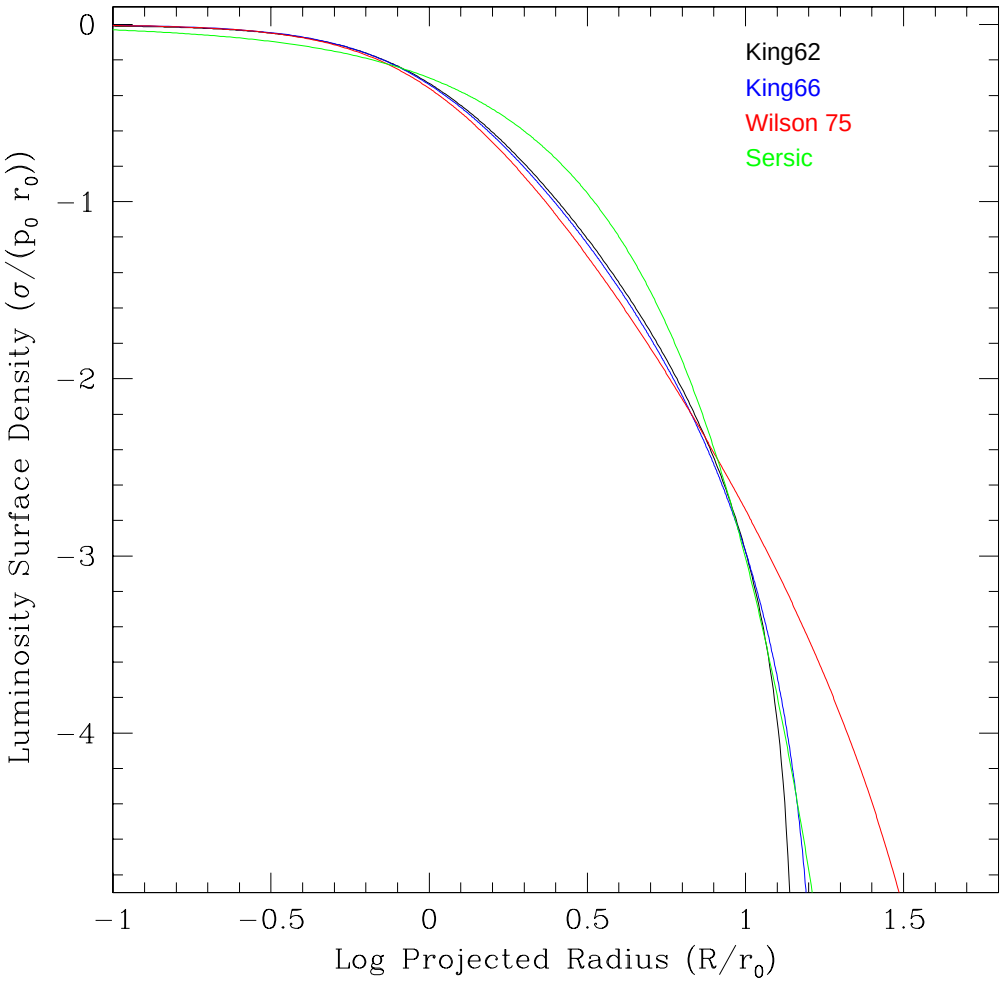

Figure 2.3: K62, K66, W75, and S68 models of luminosity surface density versus projected radius with equal central potentials.

where I(R) is the surface brightness at radius R and I_e is the surface brightness at the galaxy's effective radius R_e. The dimensionless parameter n is known as the Sérsic index. The function b_n must be determined numerically by using the condition that R_e is the radius which encloses half the light of the galaxy, represented mathematically by the relation $\int_0^{R_e} RI_n(R)\,dR = \frac{1}{2}\int_0^{\infty} RI_n(R)\,dR$. However, the formula

$$b_n = 2n - 0.324 \tag{2.56}$$

is an acceptable approximation, with fractional error less than 0.001 for $1 < n < 10$ (Binney & Tremaine, 2008).

It has been shown that the Sérsic index n is correlated with galaxy luminosity. The most luminous elliptical galaxies have a value of n of approximately 6, while fainter elliptical galaxies have values of n closer to 2 (Binney & Tremaine, 2008). The latter point suggests that the Sérsic law could be applied to globular clusters, with the expected best fit Sérsic index to be near the faint elliptical galaxy value of 2. However, Equation 2.55 will not have a special value of radius R that results in $I(R) = 0$, which means it has no tidal limit. Hence S68 cannot be used to determined globular cluster tidal radii to compare with K62, K66, and W75. Since S68 can be used to determine the effective radii of globular clusters, we will still fit S68 models to our observations, and compare the fit effective radius with other models.

2.4 The Effect of Globular Cluster Orbit on Tidal Radius

As previously discussed in Sections 2.1 and 2.2, the value chosen for a globular cluster's galactocentric distance is very important when calculating tidal radii. Theoretical derivations assume that a cluster has a circular orbit around its host galaxy. This ensures that the cluster's present galactocentric distance is equal to its perigalactic distance at all times. However, we know from the solved orbits of Milky Way globular clusters (Dinescu et al., 1999; Casetti-Dinescu et al., 2007) that this is not the case. In fact, assuming a circular orbit establishes the upper limit of a cluster's tidal radius. This is best illustrated in Figure 2.4. A globular cluster (small circle) is presently located 5 kpc from the center of a galaxy (large circle). If the cluster has a circular orbit (red dotted line), then it will always have a galactocentric distance of 5 kpc, which will in turn determine the cluster's tidal radius. However, if the cluster instead has an eccentric orbit (blue dotted line), even though its current galactocentric distance is 5 kpc, its orbit will take it deeper into the tidal field of the galaxy. Therefore, the perigalactic distance will determine the cluster's tidal radius, which will be much smaller then if the cluster had a circular orbit as it is subject to a much stronger tidal field. This scenario indicates that the orbit of a cluster needs to solved before the tidal radius can be determined.

For a population of globular clusters, a measurement of orbital anisotropy (β) provides an indication of the distribution of cluster orbits. Orbital anisotropy is related to the mean velocity ($\bar{v}$) and velocity dispersion (σ) in the R, θ, and

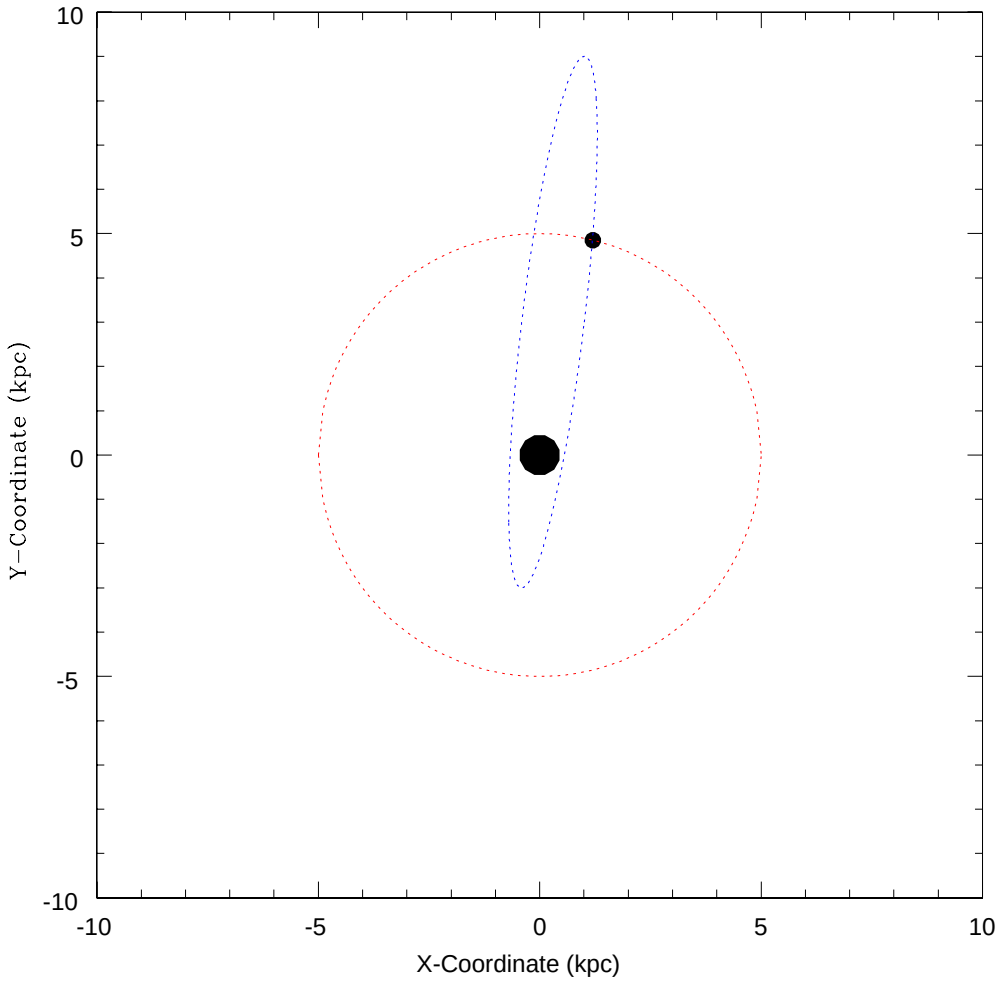

Figure 2.4: Globular cluster (small circle) orbiting around the center of a galaxy (large circle) on either a circular orbit (red) or eccentric orbit (blue)

ϕ directions as given in Equation **??**. It is believed that β can be written in terms of either the mean velocity or velocity dispersion of the population if the system is taken to be an isothermal sphere.

$$\begin{aligned} \beta &= 1 - \frac{\bar{v}_\theta^2 + \bar{v}_\phi^2}{2\bar{v}_R^2} \\ &= 1 - \frac{\sigma_\theta^2 + \sigma_\phi^2}{2\sigma_R^2} \end{aligned} \tag{2.57}$$

For a population of clusters with all circular orbits, we expect that the mean radial velocity and the radial velocity dispersion will be zero. This results in $\beta \to -\infty$, and corresponds to the largest the tidal radius of each cluster can be. If we increase the value of β, we reach the isotropic case where the velocity distribution in all three directions is equal at $\beta = 0$. Under this condition, clusters will have a range of different orbits, with a mean eccentricity of about 0.5 (Prieto & Gnedin, 2008). Finally, increasing β to a value of one corresponds to purely radial orbits, where the cluster bounces back and forth between its pericenter and apocenter, with no tangential motion. This marks the lower limit of a cluster's tidal radius, as a purely radial orbit results in the smallest possible perigalactic distance. The local value of β must be taken into consideration when calculating theoretical tidal radii, as it provides an indication of whether a cluster's current galactocentric distance is on average close to its perigalactic distance ($\beta < 0$) or its galactocentric distance is on average larger than its perigalactic distance ($\beta > 0$). This will be explored in much more detail in Chapter 4.

Bibliography

Bertin, G. & Varri, A. L. 2008, ApJ, 689, 1005

Binney, J. & Tremaine, S. 2008, Galactic Dynamics, 2^{nd} edition (Princeton, NJ, Princeton University Press)

Brosche, P., Odenkirchen, M., Geffert, M. 1999, New Astron., 4, 133

de Vaucouleurs, G. 1948, Ann. d'Astroph., 11, 247

Casetti-Dinescu, D.I., Girard, T.M., Herrera, D., van Altena, W.E., López, C.E., Castillo, D.J. 2007, AJ, 134, 195

Dinescu, D.I., Girard, T.M., van Altena, W.E. 1999, AJ, 117, 1792

Innanen, K. A., Harris, W.E., Webbink, R.F. 1983, AJ, 88, 338

Jordi, K. & Grebel, E. K., 2010, A&A, 552, id.A71

King, I. R. 1962, AJ, 67, 471

King, I. R. 1962, AJ, 70, 376

King, I. R. 1966, AJ, 71, 64

Kupper, A. H. W, Kroupa, P, Baumgardt, H., Heggie , D. C., 2010, MNRAS, 407, 2260

McLaughlin, D. E., Barmby, P., Harris, W. E., Forbes, D.A., & Harris, G.L.H. 2008, MNRAS, 384, 563

Prieto, J. L. & Gnedin, O. Y. 2008, ApJ, 689, 919

Sérsic, J. L. 1968, Atlas de galaxias australes. Observatorio Astronomico, Cordoba

Skelton, P. L. & Smits, D. P. 2009, S. Afr. J. Sci., 105, 120

von Hoerner, S. 1957, ApJ, 125, 451

Wilson, C. P. 1975, AJ, 80, 175

Chapter 3

M87

With a formal understanding of what a cluster's tidal radius is, and how it can be determined both observationally and theoretically, we turn to the giant elliptical galaxy M87 to compare theory with observations. We begin our study by using the unusually deep, high signal-to-noise images of M87, which contain nearly 2000 globular clusters, to observationally determine cluster tidal radii.

3.1 Observational Data

The images we use in this study are taken with the HST Wide Field Channel of the Advanced Camera for Surveys (ACS/WFC), in the broadband filters F606W (wide V) and F814W (I). The raw images are drawn from the HST Archive and are originally from program GO-10543 (PI Baltz). The $3.4' \times 3.4'$ ACS/WFC field was centered on M87. The exposures were taken in 61 separate spacecraft visits over a 71-day period from 2005 Dec 24 to 2006 March 5: in $F814W$ there are 205 images totalling 73800 seconds, while in $F606W$ there are 49 images totalling 24500 seconds. The co-added composite exposures in each filter were combined as described in detail in Bird et al. (2010),

through use of the APSIS software (Blakeslee et al., 2003), which performs accurate image registration, cosmic-ray rejection, and distortion correction with drizzle. Subpixel resampling was done during the drizzle step to yield final combined science images with a scale $0\farcs025$ px^{-1} (half the native pixel size of the camera). As will be seen below, the subsampling produced a noticeable improvement in the effective spatial resolution of the data and thus the highest possible quality of measurement for the cluster sizes. We are indebted to John Blakeslee (HIA/NRC) for the generation of these composite images.

In order to remove the "brightness" of M87 to view globular clusters closer to the center of the galaxy, the ELLIPSE and BMODEL functions within STSDAS were used. The ELLIPSE function fits elliptical isophotes to the brightness distribution of M87 in both the V and I images. BMODEL then models the fitted elliptical isophotes into a separate image. By subtracting this new image from the original to remove the brightness of the galaxy, it is then possible to more easily detect objects that were previously hidden. The sky levels in the corners of the original images are added as background to both the F814W and F606W images, to remove negative pixel values created by the subtraction process. The relevant parameters used for the ELLIPSE and BMODEL functions are summarized in Table 3.1. The before and after images of the F814W image are illustrated in Figure 3.1.

Once the smooth light profile of M87 has been removed from the F814W and F606W images, it is then possible to identify globular cluster candidates within M87. This was done with the DAOFIND function within IRAF/DIGIPHOT/DAOPHOT. The first step was to determine the standard deviation of the background sky

Table 3.1: ELLIPSE and BMODEL Galaxy Fitting Parameters

	F814W (I)	F606W (V)
center	4200, 4600	4200, 4600
sma0	50	50
minsma	0	0
maxsma	4000	4000
step	0.1	0.1
nclip	3	3
background	87	85

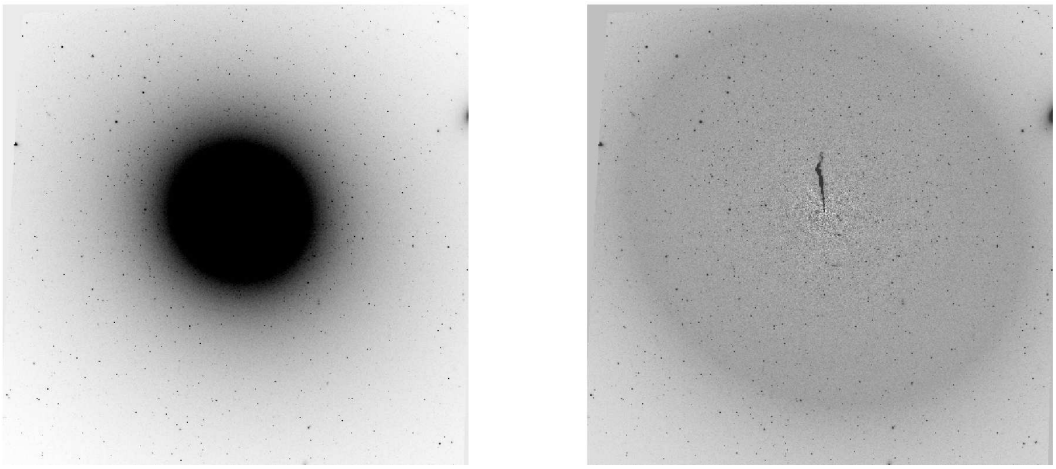

Figure 3.1: Image of F814W before the brightness of M87 has been removed (Left) and after ELLIPSE/BMODEL fitting and image subtraction (Right). The subtracted image (Right) unveils the famous M87 jet.

pixel values (σ). We then searched for candidates brighter than a brightness cut-off of $n\sigma$, where the integer n was increased until the remaining candidates contained mostly spherical, globular cluster-like objects with minimal point sources. It was important not to set the cut-off too high, such that true globular clusters were eliminated. Therefore cut-offs were chosen so that there were still non-globular cluster objects in the candidate list, which could be removed later through further cuts. We found that accepting objects that were 9 σ and 10 σ brighter than the deviation of the background sky pixels, for the F814W and F606W images respectively, resulted in 2052 globular cluster candidates. For cut-offs less than 9 σ and 10 σ, the number of found objects increased rapidly and included many non-globular cluster like objects. After objects were matched based on their position on both images, we identified two regions where candidates had to be manually removed. Any candidates found near the center of M87 ($R_{gc} < 0.2$ kpc) and near the M87 jet were removed as the background light intensity is much higher in these regions, making the identification of globular clusters difficult. A final globular cluster candidate list was produced with 1833 objects. The location of each globular cluster candidate is shown in Figure 3.2.

To construct a color-magnitude diagram (CMD) for the candidates, the instrumental magnitude in V and I of each candidate as determined by DAOFIND must be converted to a true magnitude scale. To do this, we compare our list of candidates to the list of globular clusters in M87 found by Madrid et al. (2009). Madrid et al. (2009) calibrated cluster magnitudes using the number of counts within a circular aperture of 5 pixels, an aperture correction factor, image exposure time, and photometric zero points obtained from the STScI

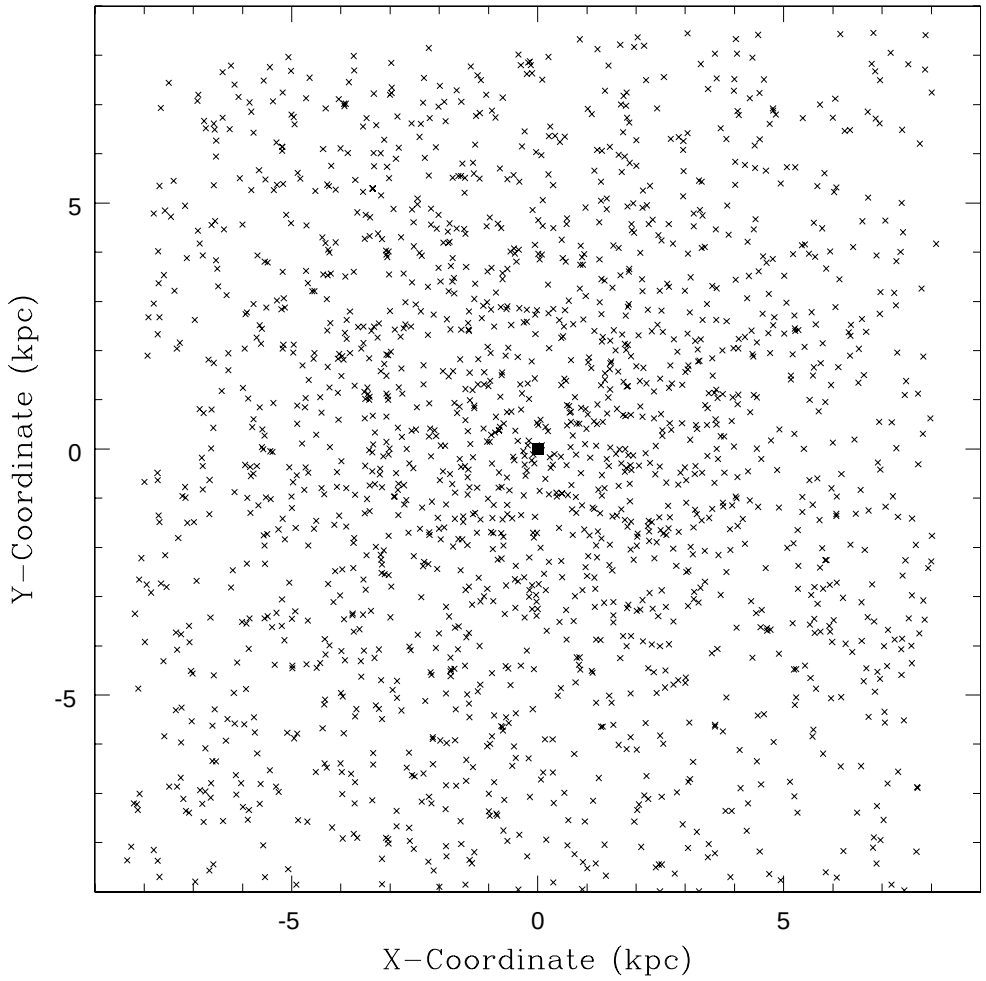

Figure 3.2: The x,y position of each globular cluster candidate in kiloparsecs, relative to the center of M87 (marked as a black square).

website. For the candidates which were able to be matched based on position to the Madrid et al. (2009) dataset, we plot their true magnitude (Madrid et al., 2009) versus their instrumental magnitude in both V and I in Figure 3.3. Ignoring outliers, the linear relationships between true and instrumental magnitude for both V and I were found to be

$$V_{true} = 0.96 \times V_{instrumental} + 24.01 \tag{3.1}$$

$$I_{true} = 1.00 \times I_{instrumental} + 25.37 \tag{3.2}$$

These relationships are plotted in red on Figure 3.3, and were used to convert the instrumental magnitudes of cluster candidates that were not matched with a Madrid et al. (2009) globular cluster. The data points which are displaced above the lines of best fit by approximately 0.5 are primarily stars. Therefore, it was expected that these data points would be offset from the median trend.

A CMD of the candidates using their true V and I magnitudes can be seen in Figure 3.4. However, not all of these candidates are believed to be globular clusters. More specifically, objects in Figure 3.4 which are located far from the main candidate population or near the colour-magnitude limit of the images (faint end of candidate population) are likely not globular clusters, and are instead likely background galaxies, blended clusters, or foreground stars. These objects will eventually be removed from the candidate list once their surface brightness profiles are fit with models. Not only will the fits be poor,

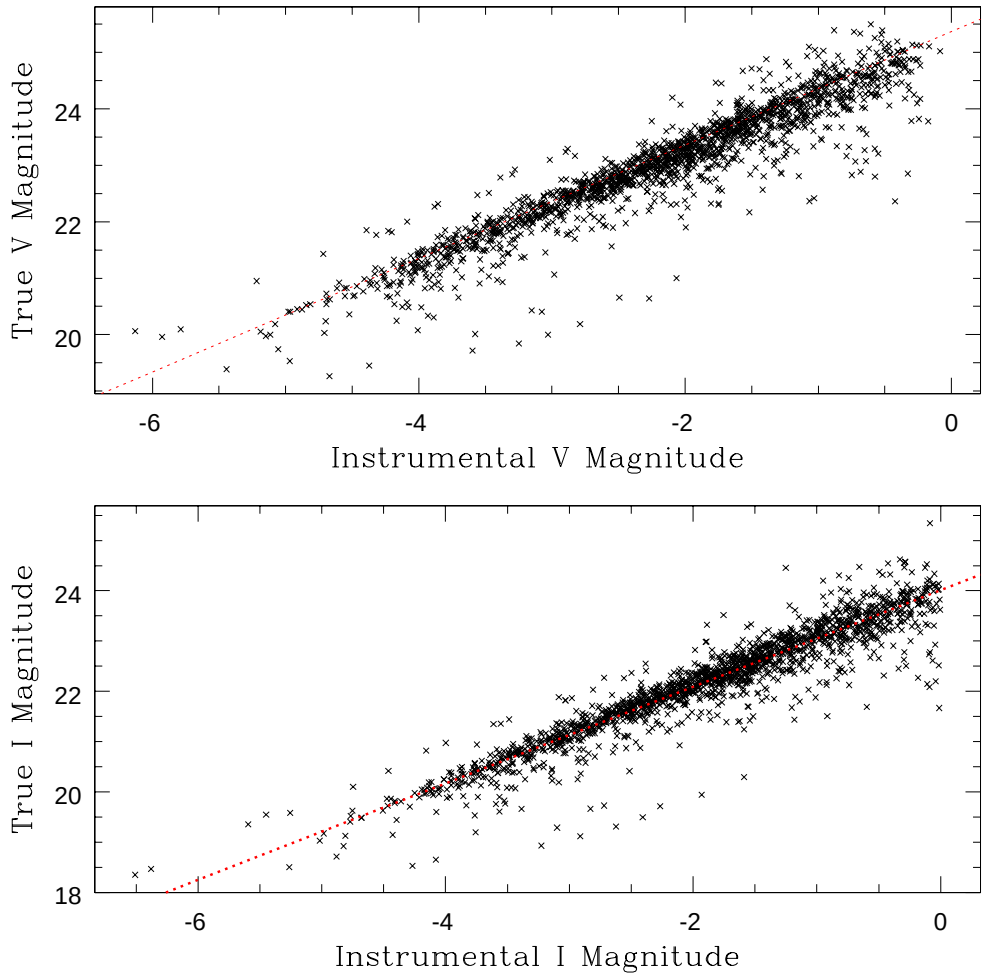

Figure 3.3: True magnitude (Madrid et al., 2009) versus instrumental magnitude for both V (upper) and I (lower) globular cluster candidates. The red lines illustrate a linear fit to the data.

but the model parameters fit to a background galaxy will differ greatly in the V and I images since different broadband filters sample different populations within a galaxy.

3.2 Model Fitting

With the final list of globular cluster candidates, the surface brightness distribution of each cluster is fit with each of the models described in Chapter 2.3 via a fitting program from Dean McLaughlin (McLaughlin et al., 2008) entitled CLUSTERFIT. The STSDAS ELLIPSE function was once again employed to determine the brightness profile of each individual cluster, as opposed to the brightness distribution of the galaxy. This was accomplished via a PYRAF routine which adjusted the center position of each isophote to match the position of each cluster candidate, and then ran ELLIPSE on each cluster. The relevant ELLIPSE parameters are listed in Table 3.2. In order to be properly used within CLUSTERFIT, the background intensity was subtracted from each isophote. This was accomplished by taking the average intensity of the final five data points and taking that value as the background intensity. The final five data points were always beyond the radius of the cluster, as each brightness profile was initially measured out to a distance of 100 pc. Any clusters with fit tidal radii greater than 60 pc were then re-measured out to larger radii to ensure the final five data points of the intensity profile are greater than the size of the cluster.

For a typical globular cluster (GC20), the brightness profile in the I and V images are illustrated in Figures 3.5 and 3.6. The error bars represent the

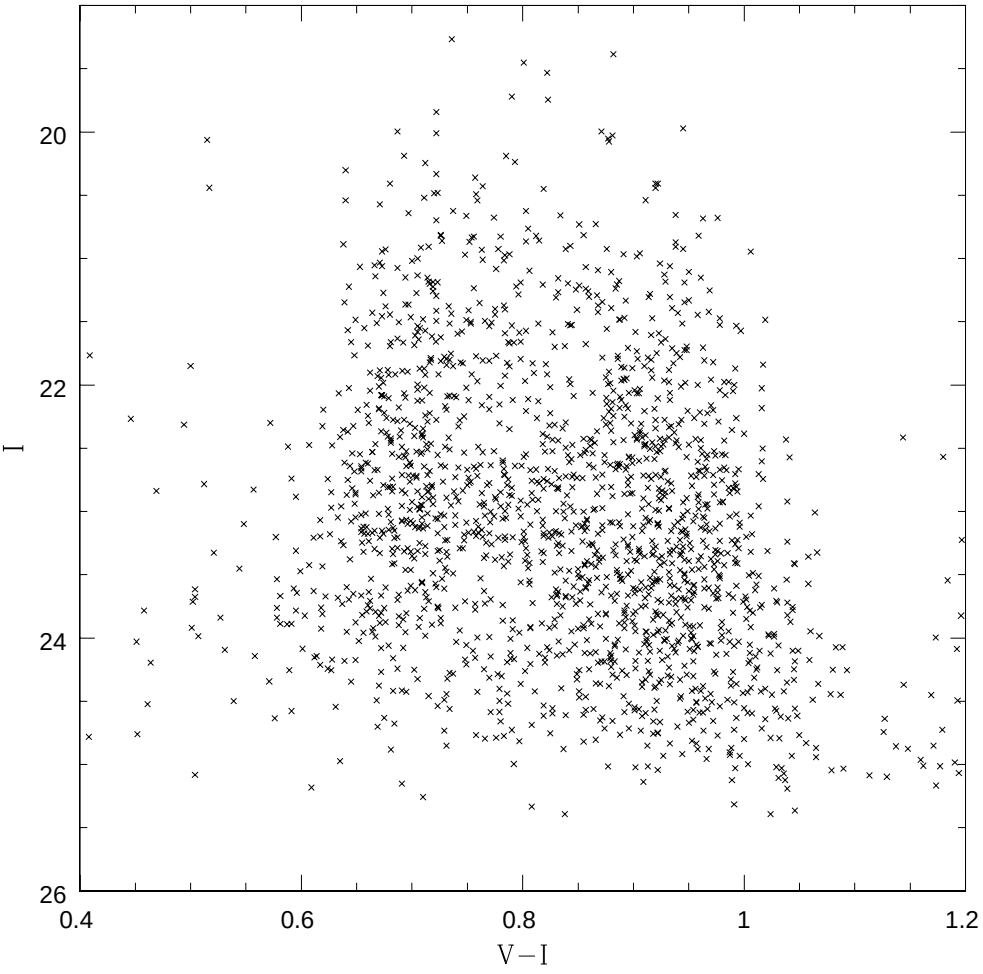

Figure 3.4: Instrumental CMD of the globular cluster candidates in M87.

Table 3.2: ELLIPSE Globular Cluster Fitting Parameters

	Value
sma0	5
minsma	0
maxsma	50
step	0.05

error in surface brightness as determined by the ELLIPSE fitting routine. It is important to note that the surface brightness profile does not explicitly go to zero, but instead levels off to a background value.

As discussed in Chapter 2.3, we will be comparing our observations to King (1962), King (1966), Wilson (1975), and Sérsic (1968) models. Based on this comparison we will decide which results will be compared to the theory. Before we can compare the models, each model is convolved with a point spread function (PSF). The PSF is a representation of a point source of light as seen through the optics of a telescope. A point source, or in this case a star, would have an intensity profile equal to a delta function, however due to the optics of the telescope the intensity profile as a function of position is Gaussian-like as opposed to a delta function. The profile is essentially the diffraction pattern of the optics that the light from a point source passes through before reaching the camera. Using tools within IRAF/DIGIPHOT/DAOPHOT, a PSF was built for both the V and I images by averaging the profiles of approximately 20 stars across the field of view, which has a scale of $0\farcs025$/pixel (Madrid et al., 2009). Models must be convolved with the PSF of each image before fitting can take place, such that the model is on the same scale is the images. With a globular cluster brightness profile that has been background subtracted, the program computes a dimensionless model profile $\tilde{I}_{mod} = I_{mod}/I_0$ where I_{mod} is the model intensity profile and I_0 is the central intensity. The model profile is then convolved with a point spread function from the observations via

$$\tilde{I}^*_{mod}(R|r_0) = \int\int_{-\infty}^{\infty} \tilde{I}_{mod}(R'/r_0)\tilde{I}_{psf}[(x-x'),(y-y')]\,dx\,dy \qquad (3.3)$$

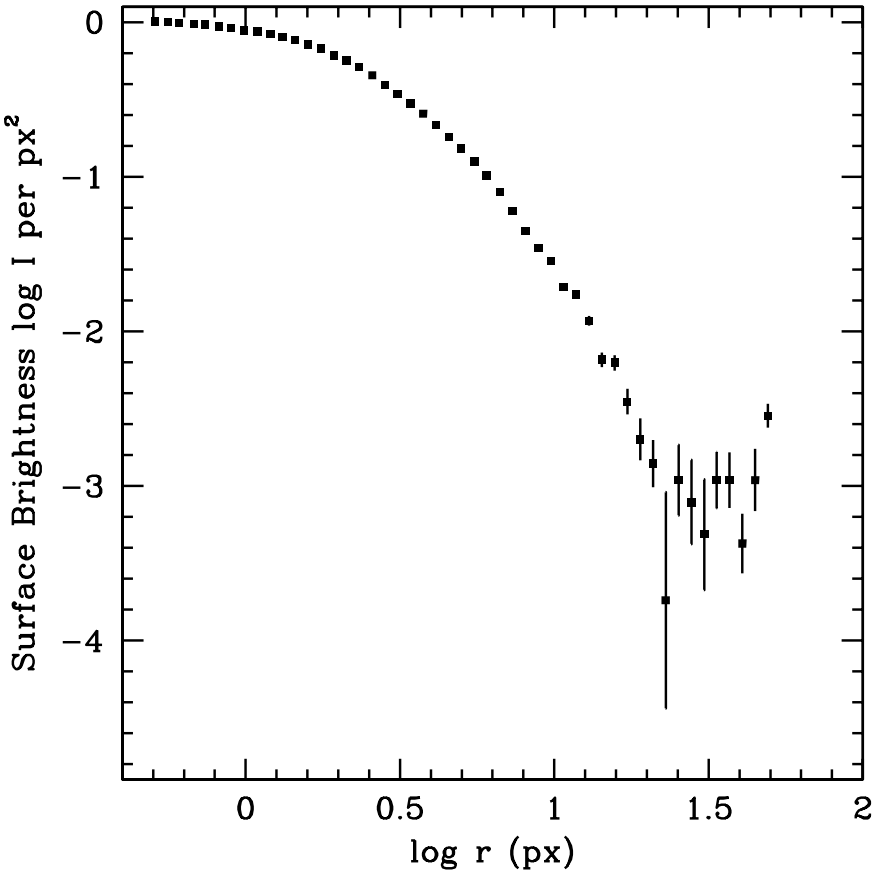

Figure 3.5: Background subtracted brightness distribution as determined by STSDAS ELLIPSE for a globular cluster in M87 in the I band.

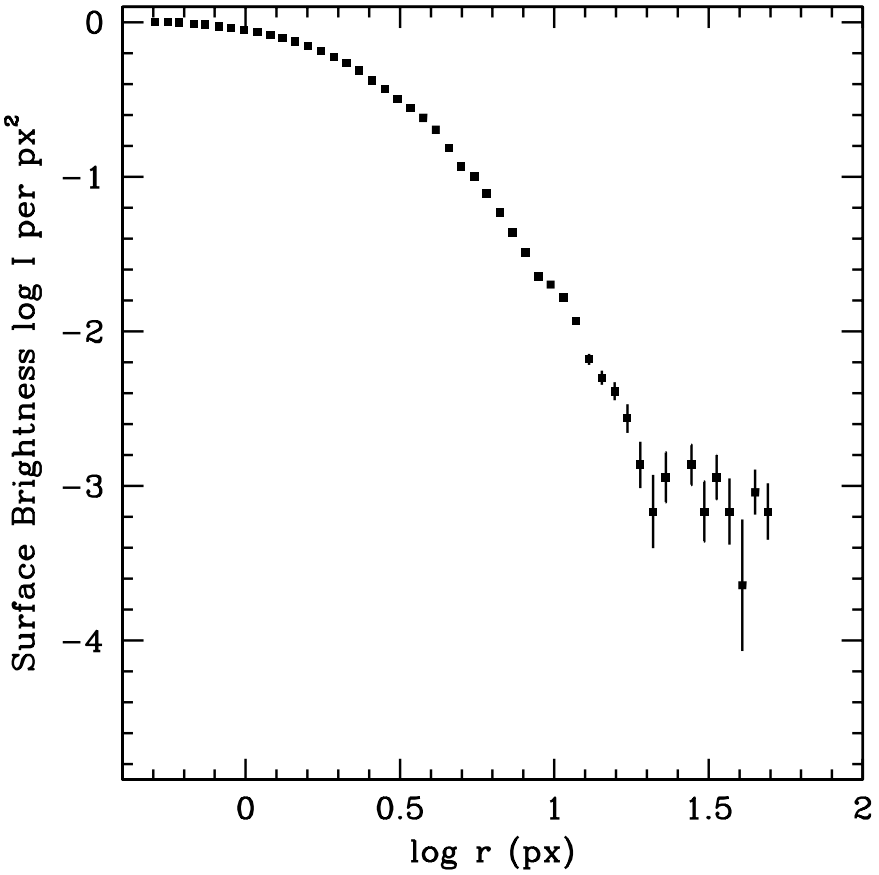

Figure 3.6: Background subtracted brightness distribution as determined by STSDAS ELLIPSE for a globular cluster in M87 in the V band.

where r_0 is the model scale radius, $R^2 = x^2 + y^2$, $R'^2 = x'^2 + y'^2$, and $\tilde{I}_{psf}$ is the PSF profile normalized to unit total luminosity.

For a given shape parameter (k for K62, W_0 for K66 and W75, n for S68), the program finds the scale radius which minimizes Equation 3.4, where σ_i is the error in $I_{obs}(R_i)$. A range of shape parameters is then tried until the lowest possible χ^2 value is found.

$$\chi^2 = \sum_i \frac{[I_{obs}(R_i) - I_0 \ \tilde{I}^*_{mod}(R_i|r_0)]^2}{\sigma_i^2} \tag{3.4}$$

The associated model is then said to be the best fit to the observed globular cluster. The model then returns the central concentration, scale radius, core radius, effective radius, and tidal radius of each cluster.

3.3 Model Fitting Results

3.3.1 King (1962) Results

Each globular cluster candidate was fit with a K62 model. For illustrative purposes, Figures 3.7 and 3.8 demonstrate the K62 model fit (solid line) to GC20 illustrated in Figure 3.5 and 3.6. Since the surface brightness profile does not go explicitly to zero, the model fit takes into account that it instead levels off to a background value.

The results of the K62 model fitting for GC20 are summarized in Table 3.3, where c is the central concentration, r_0 is the model scale radius, r_c is

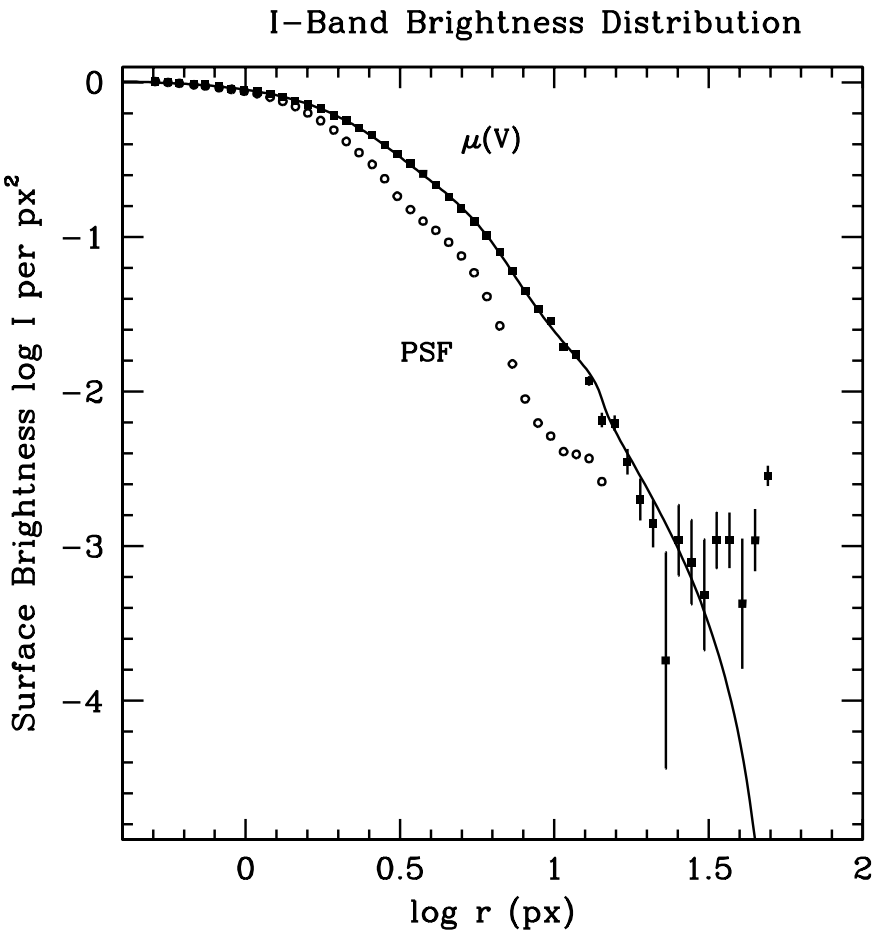

Figure 3.7: Background subtracted brightness distribution as determined by STSDAS ELLIPSE for a globular cluster in M87 in the I band, fit with a K62 model (solid line).Open circles represent the PSF.

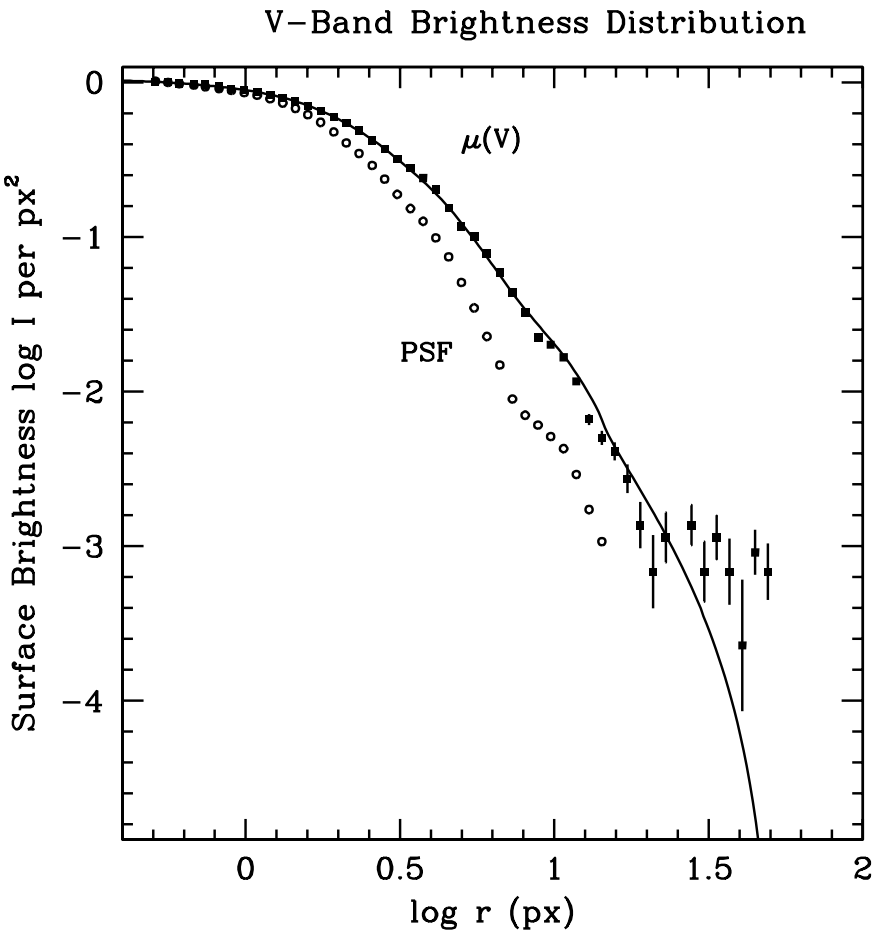

Figure 3.8: Background subtracted brightness distribution as determined by STSDAS ELLIPSE for a globular cluster in M87 in the V band, fit with a K62 model (solid line).Open circles represent the PSF.

Table 3.3: King (1962) Model Fitting to GC20

	F814W (I)	F606W (V)
c	2.18	2.32
r_o (pixels)	0.318	0.243
r_c (pixels)	0.316	0.242
r_h (pixels)	1.968	1.753
r_t (pixels)	48.145	50.798

the core radius, r_h is the effective (half light) radius, and r_t is the tidal radius (McLaughlin et al, 2008).

Averaging the two values and converting to parsecs, we get a half light radius of 3.721 pc and a tidal radius of 98.943 pc. Since the effective radius is more commonly used by observers and is more easily obtained, the remainder of this chapter will focus on the measured effective radii of each cluster. Repeating the process for each observed cluster, we can determine the half light radius and central concentration distribution for clusters in M87 in both the I and V filters (Figures 3.9 to 3.12). Not all objects were successfully fit with K62 Models. Upon visual inspection, these objects were either located in crowded areas, near the edge of the image, or were clearly not globular clusters based on their non-spherical shape. These objects were removed from the dataset.

From Figures 3.9 and 3.11, we see that the peaks of the central concentration distributions are at approximately 1.6 (I) and 1.8(V), which is similar to Galactic globular clusters which peak at 1.5 (Harris, 1996 (2010 Edition)). The distributions are also Gaussian, as expected, with the exception of a significant number of clusters with central concentrations of about 3.5. Central

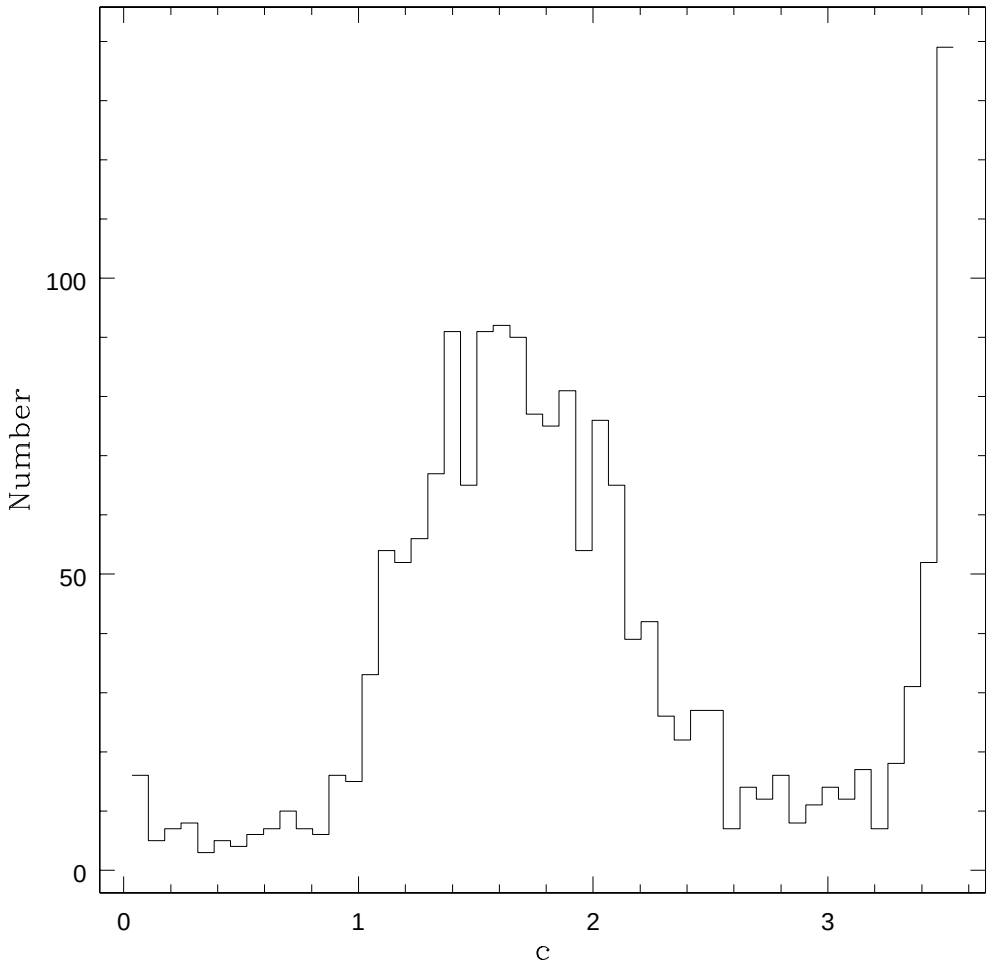

Figure 3.9: K62 central concentration distribution of observed globular clusters in the I-band.

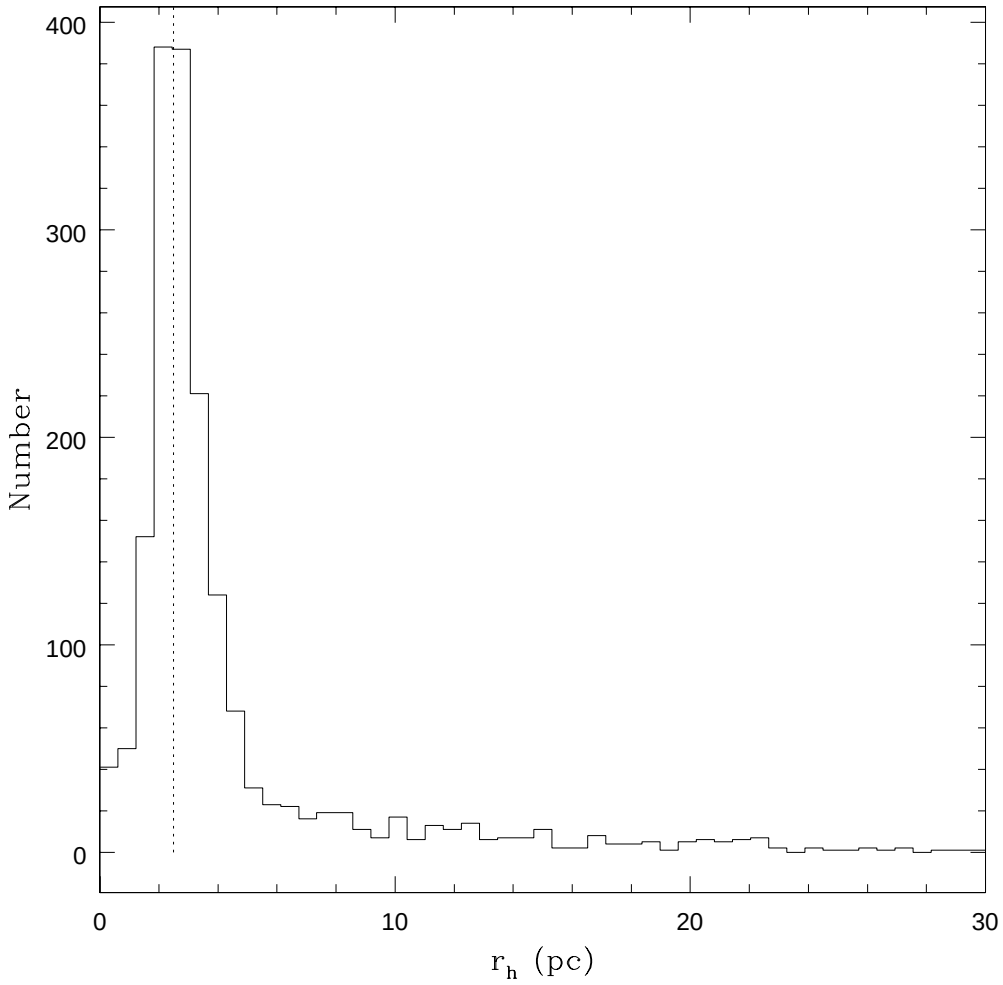

Figure 3.10: K62 effective radii distribution of observed globular clusters in the I-band. The dotted line represents r_h=2.5.

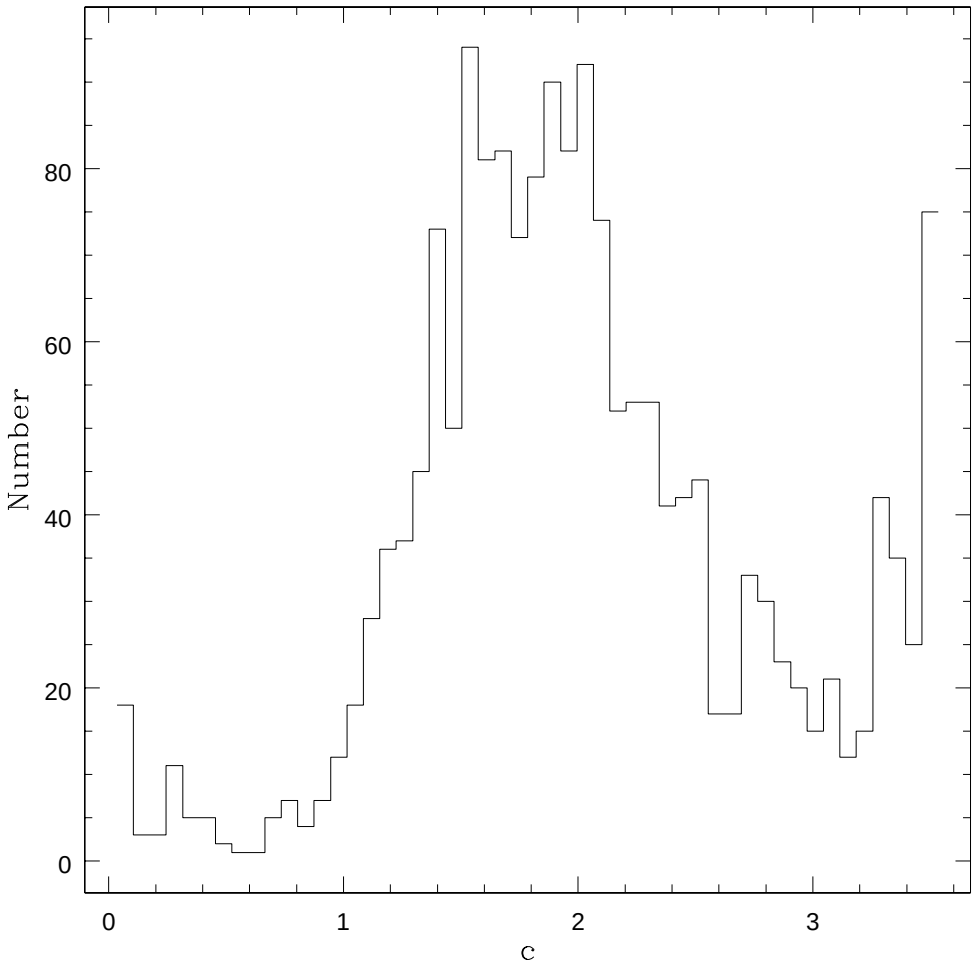

Figure 3.11: K62 central concentration distribution of observed globular clusters in the V-band.

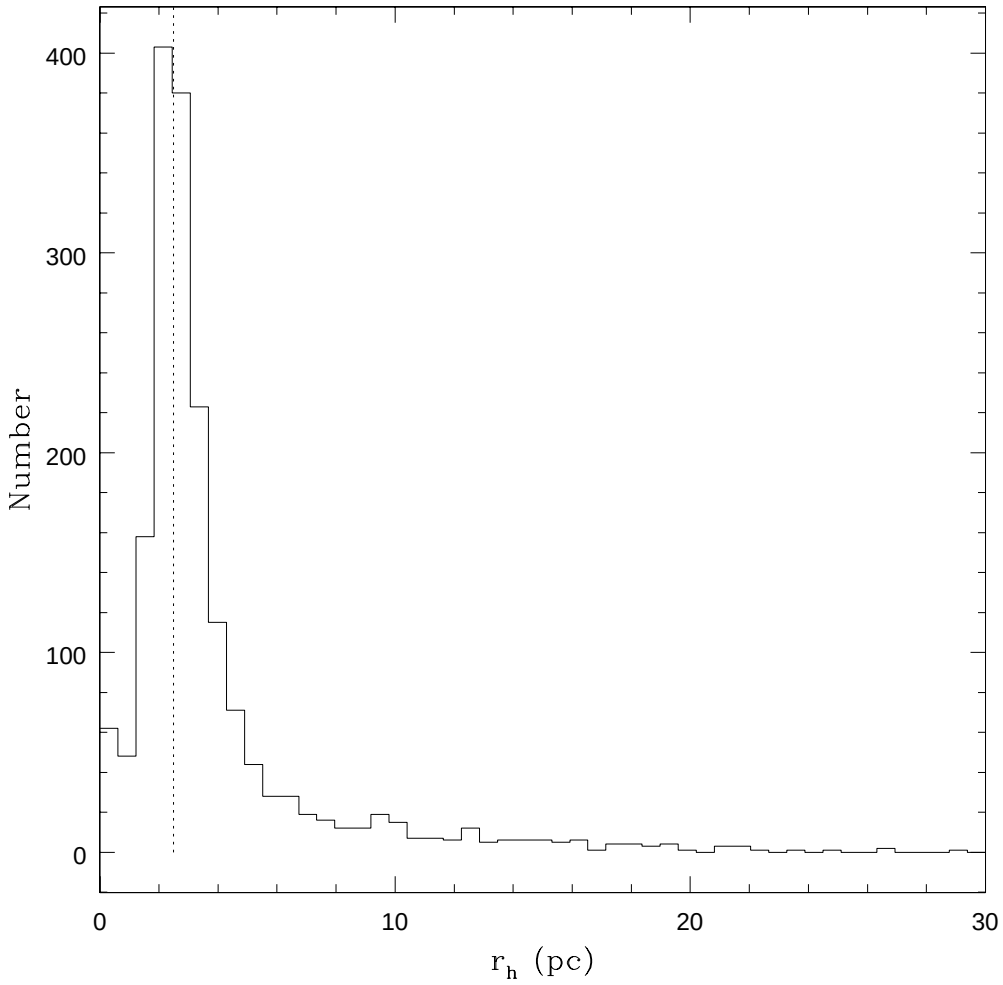

Figure 3.12: K62 effective radii distribution of observed globular clusters in the V-band. The dotted line represents r_h=2.5.

concentrations this high are not observed in MIlky Way clusters, which indicates that it is simply the result of the fitting routine not being able to fit a model to a certain number of globular cluster candidates. In addition, very few clusters are observed with central concentrations less than 0.5. Objects that are poorly fit by the models can either be background (non-spherical) galaxies, substructure in the inner regions of M87, two or more globular clusters which are crowded together, or clusters located near the edge of the image. Therefore, clusters that were fit with central concentrations less than 0.5 and greater than 3.0 were subsequently removed from the dataset.

The peak in the effective radius distributions (Figures 3.10 and 3.12) at 2.5 pc is comparable to the median value for the Milky Way of 3 pc (Harris, 1996 (2010 Edition)). This indicates both that the fitting code is properly fitting the observed clusters, and that globular clusters in M87 do not represent a unique population with respect to size and central concentration.

To examine how well a cluster has been fit by a K62 model, we examine the relationship between χ^2 and a cluster's central concentration (Figure 3.13) and effective radius (Figure 3.14). While both figures deal with parameters computed with the I dataset, the process was again repeated for the V dataset.

While it is known a poor fit is indicated by a large χ^2, we do not know how high a χ^2 is acceptable for this dataset. From Figure 3.13, we find that while 96% of clusters have $\chi^2 < 2$ with a mean value of 0.46, there are still a few objects lying above this threshold. Turning to Figure 3.14, we see that all of the objects with $\chi^2 > 10$ have very small effective radii. This suggests that the objects are either stars or background galaxies, as confirmed by visual

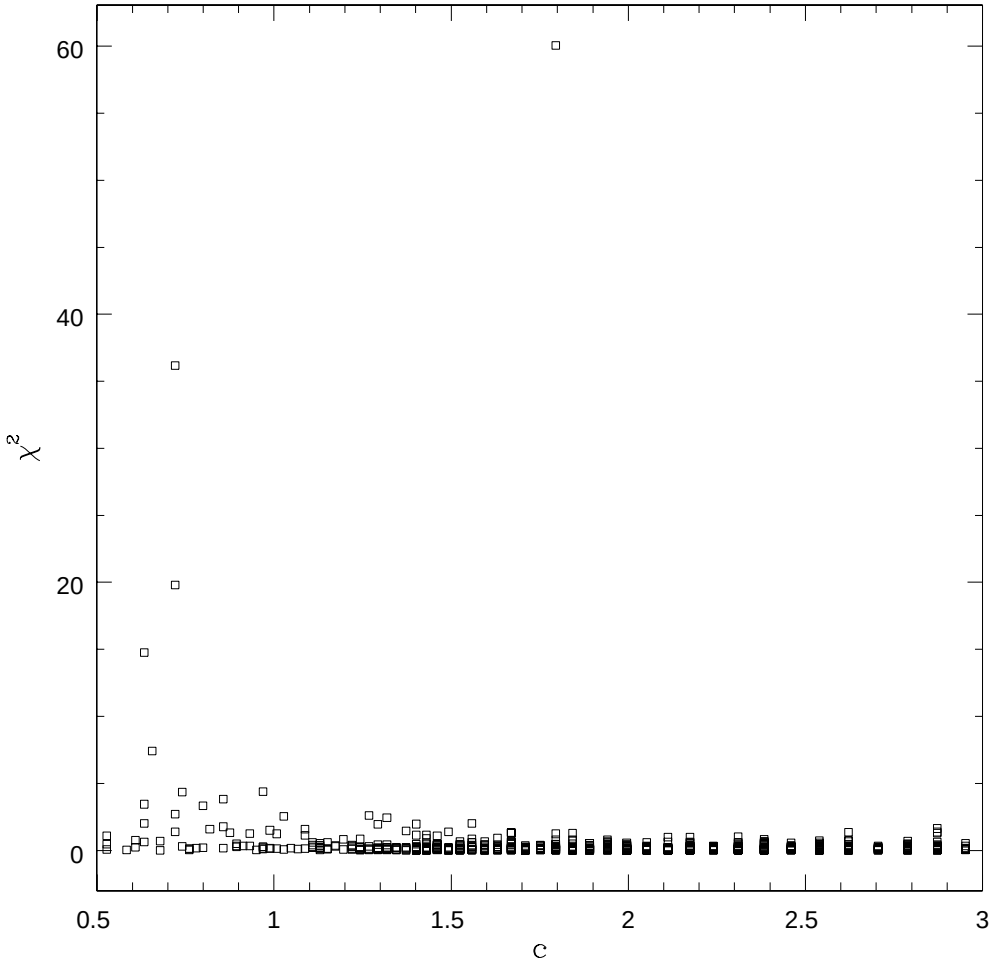

Figure 3.13: K62 χ^2 and central concentration of observed globular clusters in the I-band.

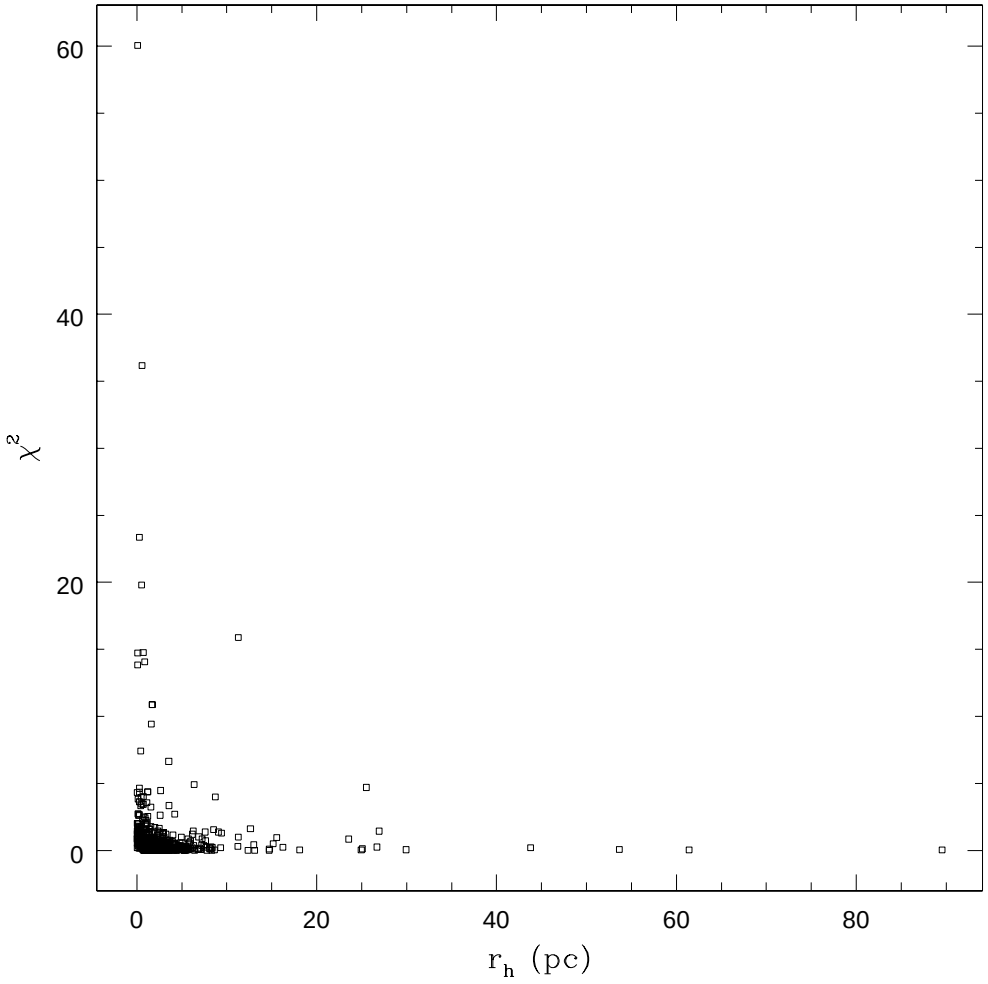

Figure 3.14: K62 χ^2 and effective radius of observed globular clusters in the I-band.

inspection. Therefore in both the V and I datasets, objects with $\chi^2 > 10$ were eliminated.

In order to get a sense of how accurate the central concentration and effective radii values from the K62 fitting are, we examine the value of each parameter as measured with the V and I images for candidates which were not removed from the list based on their position in M87 (see Section 3.1). More specifically, we can see the random measurement uncertainty in an effective radius measurement by comparing the K62 models fit to a given cluster in both V and I. Ideally, the effective radius in the V band ($r_h(V)$) should be the same as the effective radius in the I band ($r_h(I)$). Due to low foreground reddening and field contamination (Tamura et al., 2006), observational effects will not lead to clusters having different sizes as measured in different wavelengths. Figures 3.15 and 3.16 compare the central concentrations and effective radii of observed clusters respectively, as determined with the V and I images.

As seen in Figure 3.15, there is little agreement between the central concentration of a globular cluster as determined in the V and I. Figure 3.16 on the other hand indicates that despite the poor correlation in central concentrations, the effective radius of a cluster as determined with both the V and I image is quite similar. More specifically, despite clusters being fit with models with very different central concentrations, χ^2 is still minimized by similar values in effective radius. The mean difference between the V and I values of central concentration and effective radius, the uncertainty in the mean, and the root mean scatter about the V = I line are listed in Table 3.4, found in Section 3.3.5, for all model fits.

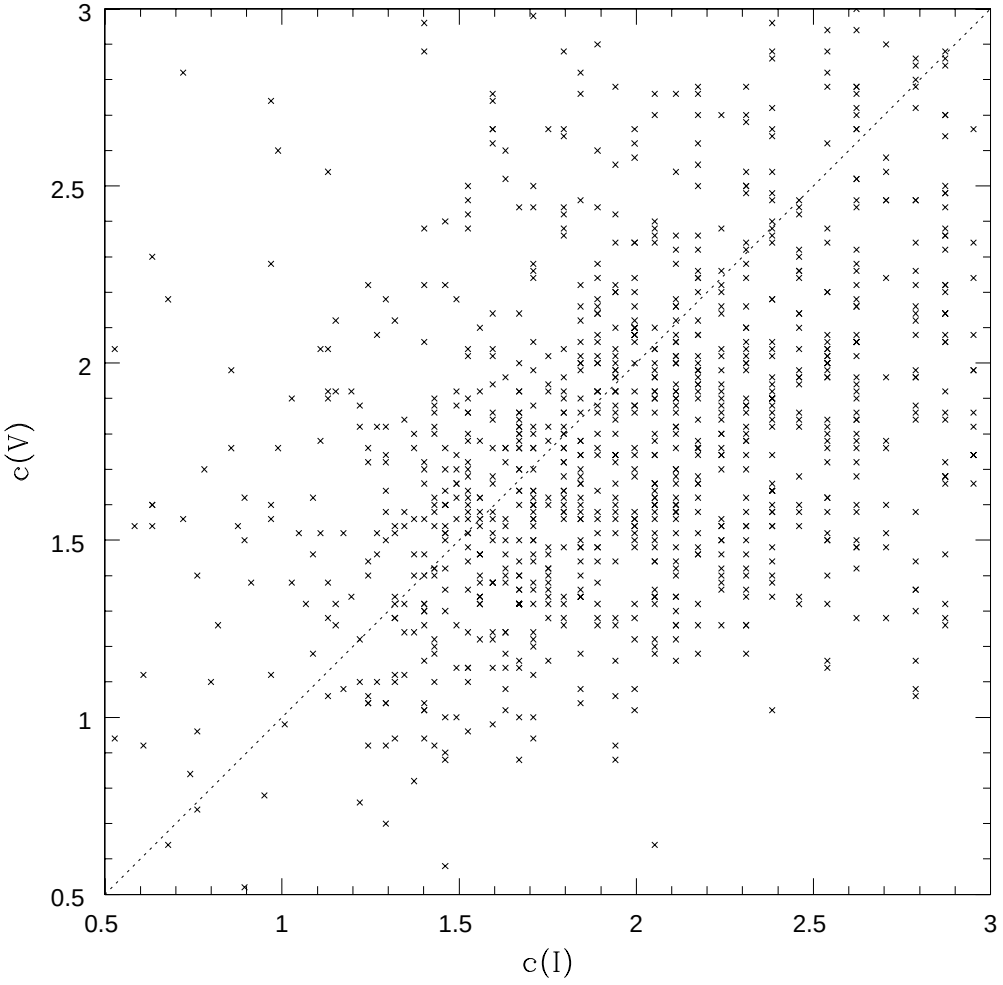

Figure 3.15: K62 central concentration of observed globular clusters as determined in both the V and I bands. The dotted line represents $c_V = c_I$.

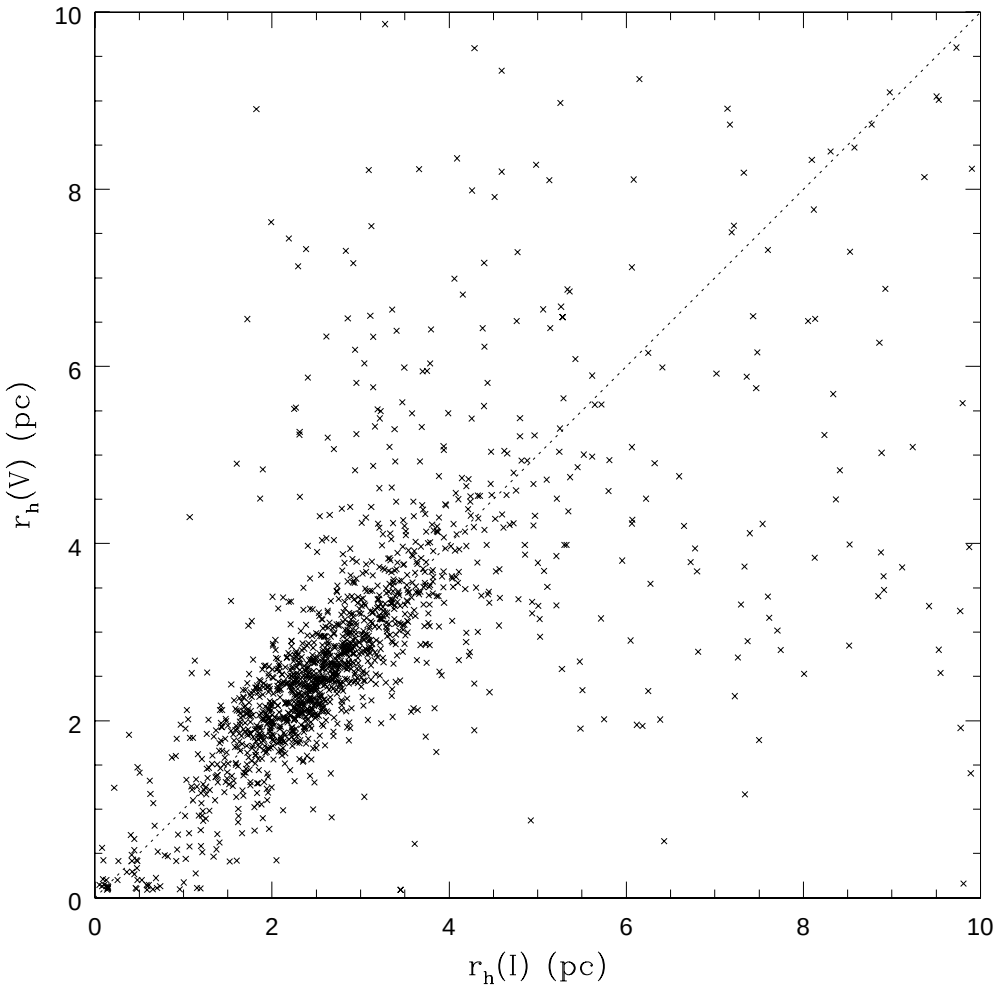

Figure 3.16: K62 effective radii of observed globular clusters as determined in both the V and I bands. The dotted line represents $r_h(V) = r_h(I)$.

To determine whether the central concentration has a strong influence on effective radius, we compare the two parameters in both the V and I bands. As seen in Figures 3.17 and 3.18, there is little correlation between the fit central concentration and the fit effective radius. Therefore the strong agreement between $r_h(V)$ and $r_h(I)$ is used to both determine a final cut to the dataset, and quantify the accuracy of the effective radius measurements. Despite a few outliers, whose non-spherical shape indicates they are not globular clusters, almost all clusters have $|r_h(V) - r_h(I)| < 2.0$, and it is this criteria that sets the final standard for whether an object is included in the final dataset. In summary, objects were removed based on their χ^2, central concentration, and $r_h(V) - r_h(I)$. The K62 model fits to the final cluster dataset had a mean χ^2 of 0.21.

The relationship that will eventually be compared to theory will be between each cluster's effective radius and its projected galactocentric distance (Figures 3.19 and 3.20).

3.3.2 King (1966) Results

In addition to K62 models, K66 models were also fit to each of the globular cluster candidates. Once the appropriate cuts were made, it was found that K66 model fits to the final cluster dataset had a mean χ^2 of 0.28. This value is larger than the mean χ^2 of the K62 model fits, suggesting K62 models are a better fit to the observations. Comparing the populations as a whole, Figure 3.21 illustrates that the K66 model predicts significantly more clusters with $1.7 < c < 2.0$ than the K62 model for the I image. The distributions

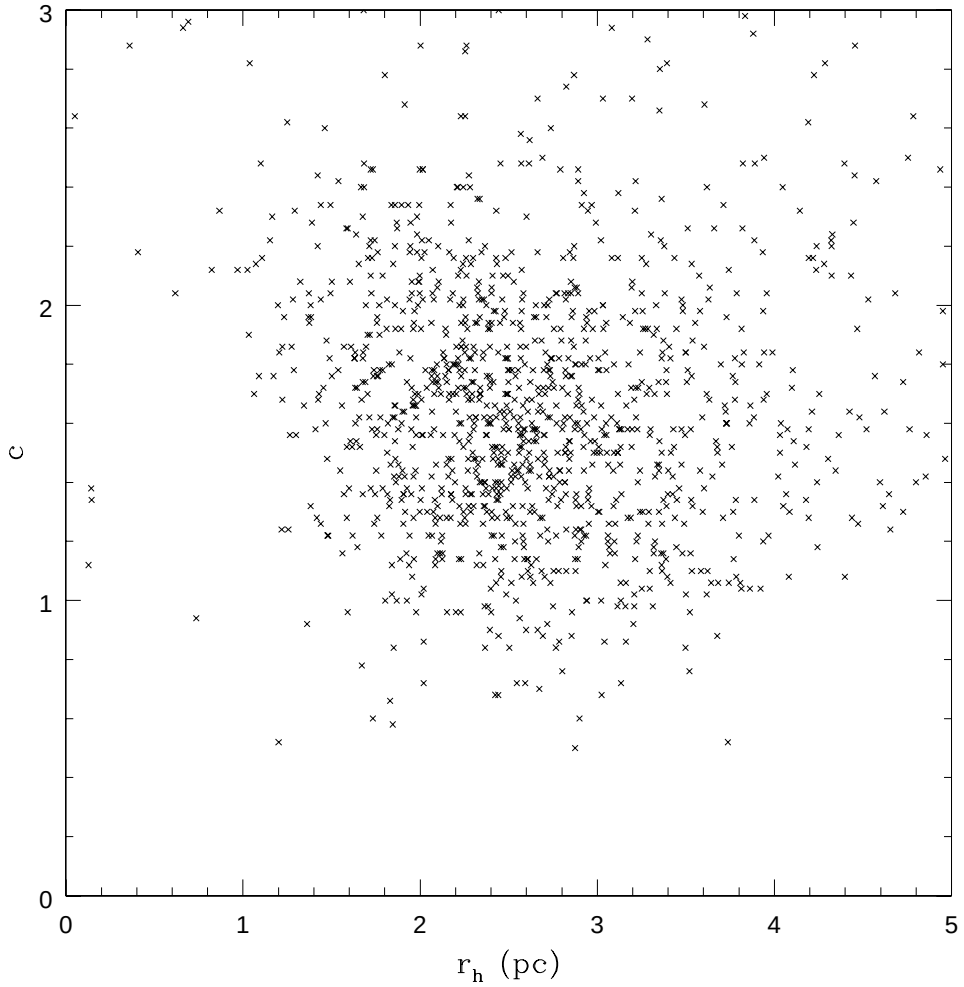

Figure 3.17: K62 central concentration and effective radius of each observed cluster in the I band.

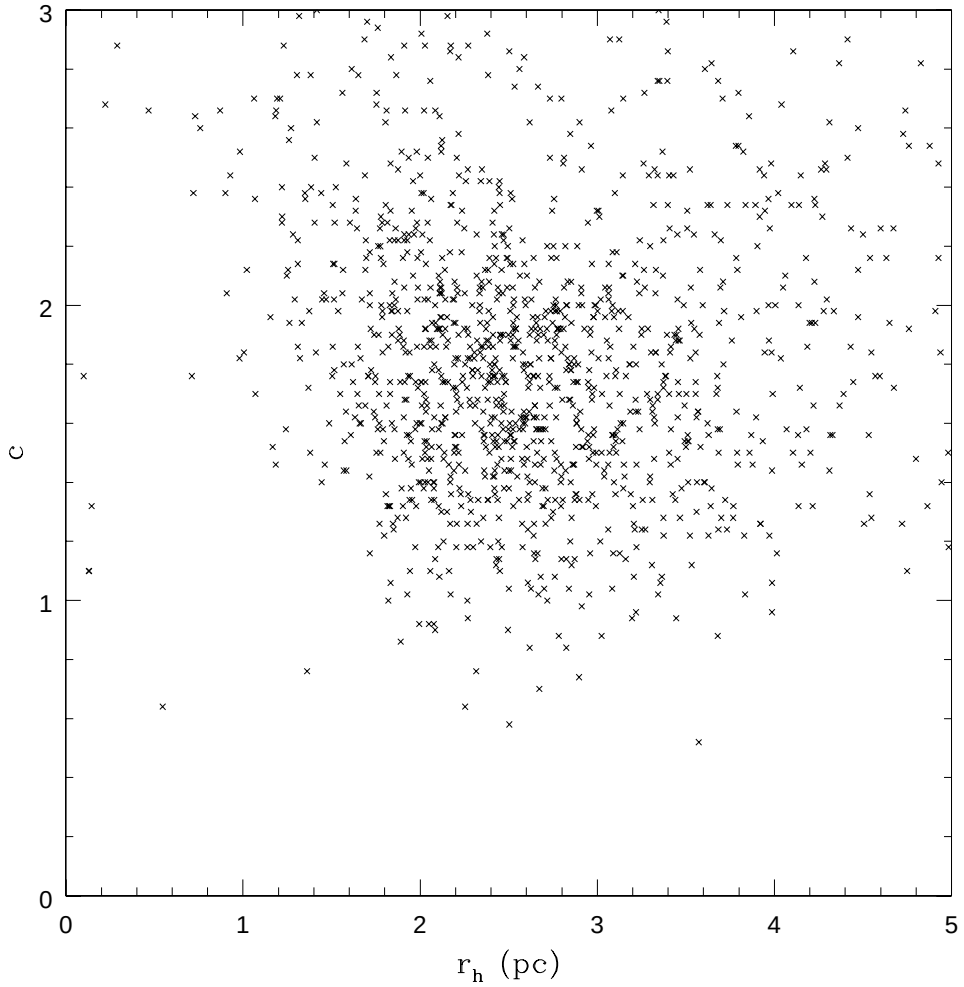

Figure 3.18: K62 central concentration and effective radius of each observed cluster in the V band.

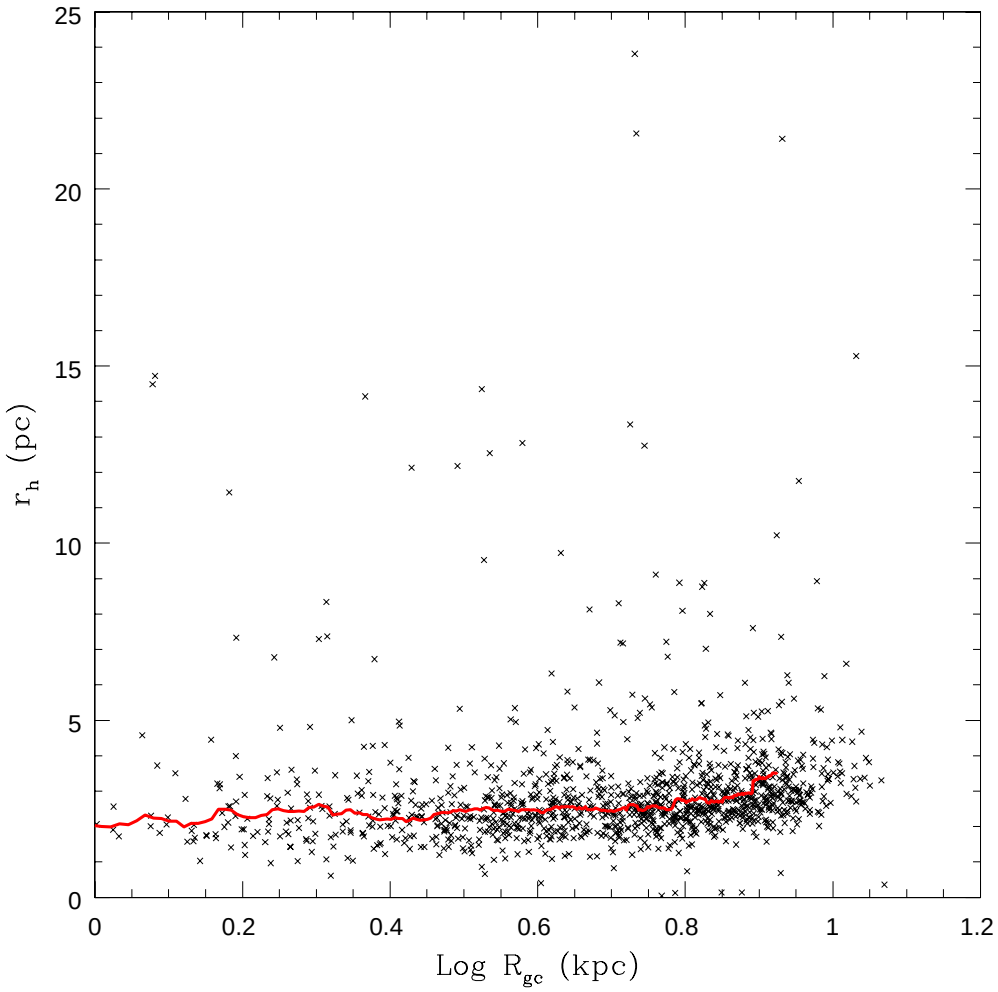

Figure 3.19: K62 effective radius vs. log projected distance for observed globular clusters in the I-band. The solid red line indicates the median effective radius.

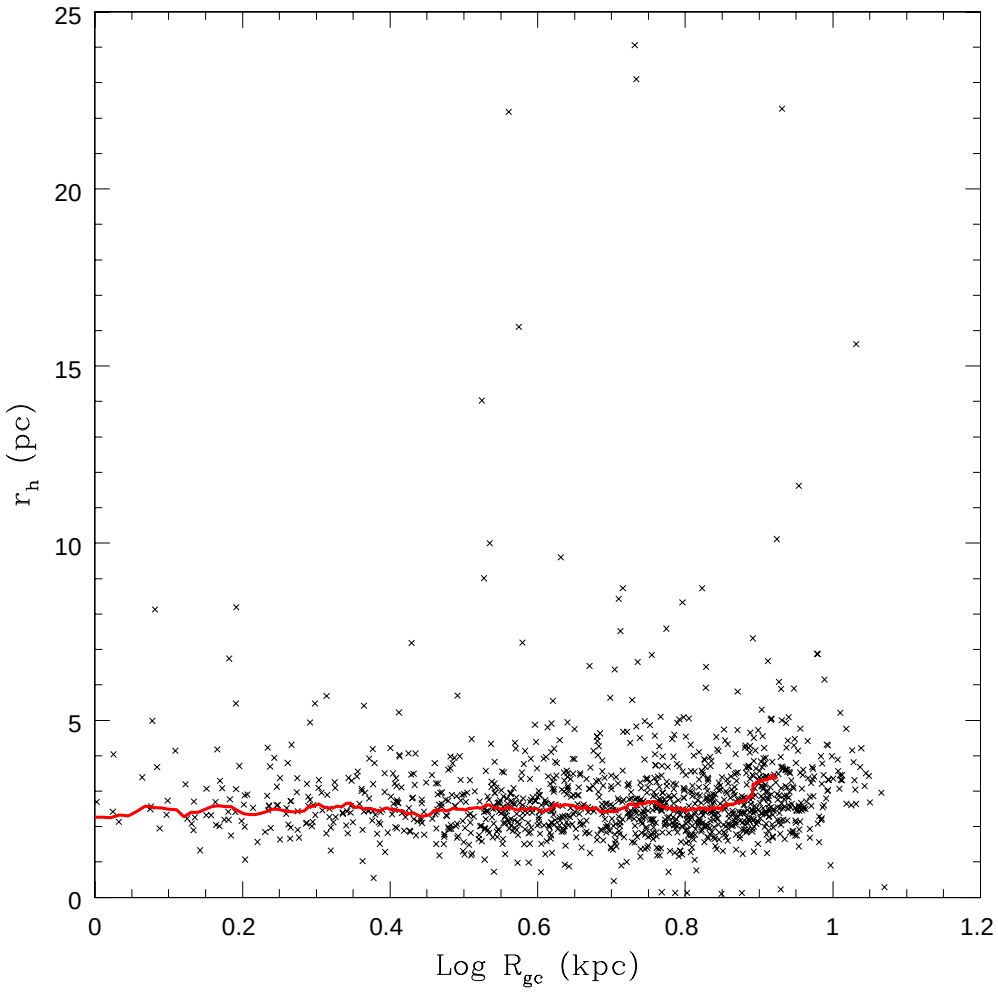

Figure 3.20: K62 effective radius vs. log projected distance for observed globular clusters in the V-band. The solid red line indicates the median effective radius.

are similar for the V image as well. Comparing the central concentrations of individual clusters (Figure 3.22) we see that for $c < 1.7$, both models are in agreement. However as central concentrations increase beyond 1.7, the K62 and K66 model fits no longer agree. As previously mentioned, the K62 central concentration distribution matches that of Galactic globular clusters. Hence for $c > 1.7$, K66 central concentrations do not.

Comparing the effective radii distributions as determined by K62 and K66 models (Figure 3.23), the two models appear to be in agreement. Both distributions peak at approximately the same effective radius ($r_h = 2.5$), which is comparable to the Milky Way (Harris, 1996 (2010 Edition)). Examining the effective radius of each cluster individually (Figure 3.24) we see that while the majority of clusters have the same effective radius as determined by both models, there is a significant population of clusters with K62 effective radii larger than K66 effective radii. Further investigation made it clear that these were the same clusters that are responsible for the central concentration discrepancy between the two models. This discrepancy in both central concentration and effective radius between the K62 and K66 models can be understood by considering Figure 3.25, which illustrates the relationship between the ratio of a cluster's effective radius to its tidal radius and cluster central concentration for both K62 (black) and K66 (models). In the case of K62 model fit clusters, we see a smooth monotonic relationship between r_h/r_t and central concentration. Hence the smaller the ratio of r_h/r_t, the larger the central concentration. This explains the Gaussian-like central concentration distribution observed in Figures 3.9 and 3.11. However for the K66 case, the relationship has a minimum around a central concentration of 1.7 or 1.8. This results in any clusters with

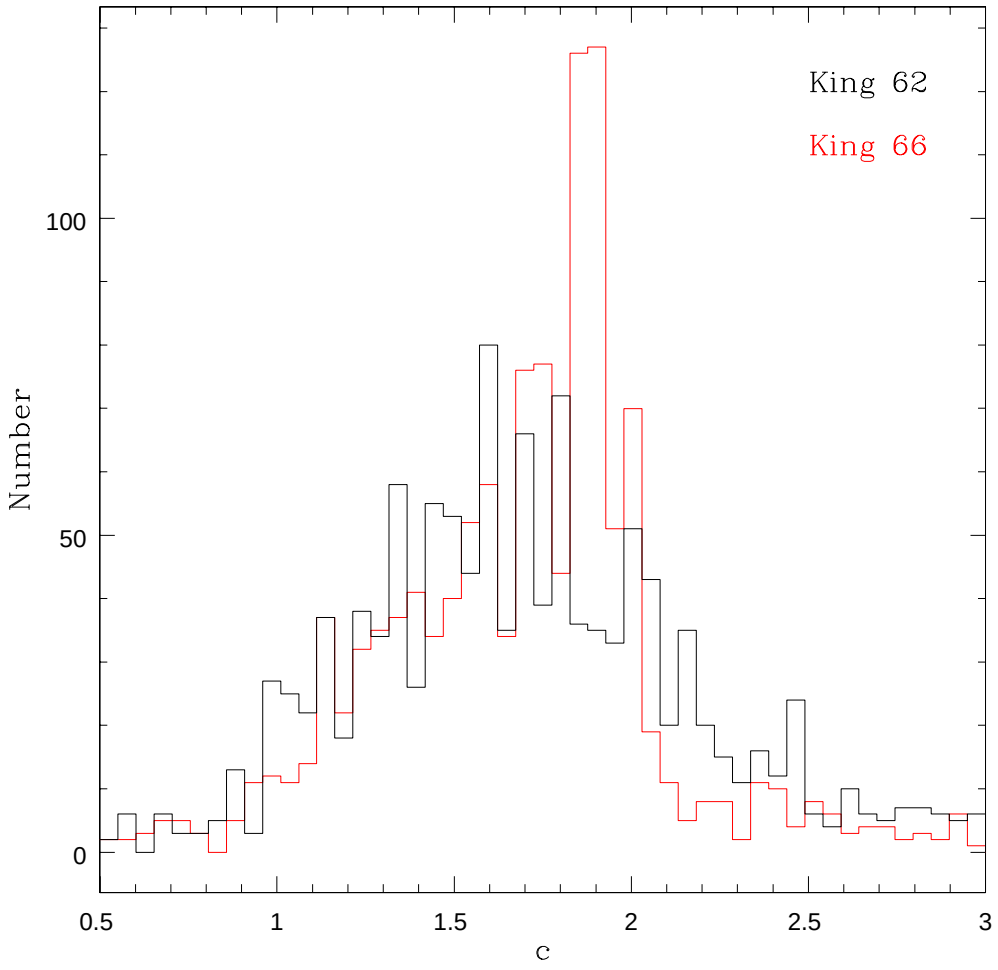

Figure 3.21: K62 (black) and K66 (red) central concentration distributions of observed globular clusters in the I-band.

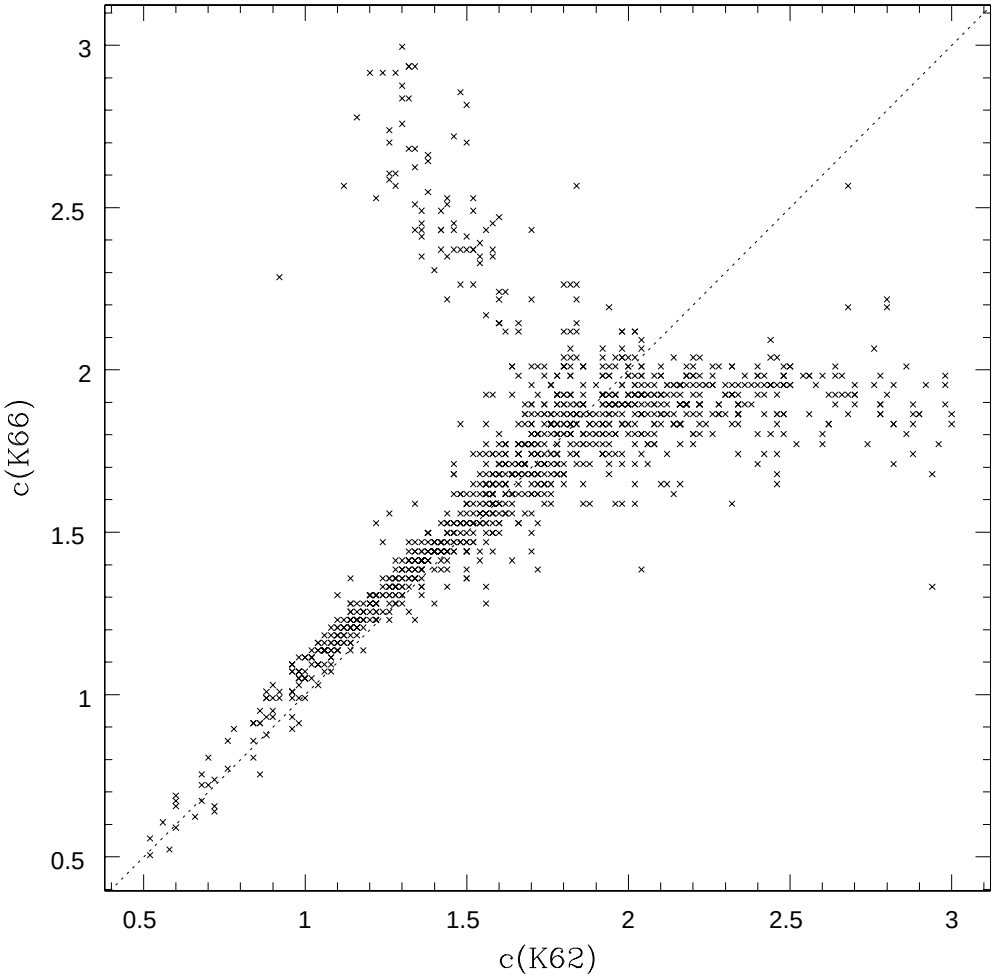

Figure 3.22: K62 vs. K66 central concentrations of observed globular clusters in the I-band.

small ratios of r_h/r_t being forced to have a central concentration of around 1.7 or 1.8. This explains both the clumping of K66 clusters at $c = 1.7$ in Figure 3.21 and the split at $c = 1.7$ between K66 and K62 central concentrations. In terms of effective radii, we see in Figure 3.25 that for clusters with $c > 1.7$, K62 models allow smaller values for r_h/r_t than K66 models. Hence for a fixed tidal radius, K62 effective radii will be smaller than K66 radii, as we observe in Figure 3.23.

To further compare K62 and K66 models, we can consider Figure 3.30 located at the end of this chapter, which illustrates how all four models (K62, K66, W75, and S68) are used to fit GC20. Comparing the K62 fit (black) and K66 fit (blue), we see that the K66 model favours a sharp tidal cutoff that results in a smaller tidal radius. The K62 model on the other hand favours a more gradual tidal cutoff, and a larger tidal radius. This supports our findings of certain globular clusters having K66 tidal radii less than K62 tidal radii. Furthermore, the issue of having measurements in the inner region of a cluster influence the outer tidal radius which was described in Chapter 2 is most evident in Figure 3.30, where we see that while all models are in agreement for the inner regions of the cluster, they all predict slightly different behaviours in the outer region.

Ultimately this comparison suggests that either the K62 or K66 models due not reflect the true brightness profiles of this sub-population of globular clusters. We will turn to the results of W75 and S68 model fitting and uncertainty calculations to identify which King model is best for comparison to

theory. More specifically, we must answer the question of whether K62 or K66 models yield the better estimate of the effective radius of each cluster.

3.3.3 Wilson (1975) Results

For an additional comparison, W75 models were fit to each of the globular cluster candidates. After the final cuts were made, the W75 model fits had a mean χ^2 of 0.29. This value is larger than the mean χ^2 of both the K62 and K66 model fits, suggesting K62 models are still the best fit to the observations. Since the central concentration parameter in a W75 model is defined differently than that of K62 and K66, a comparison of central concentrations would be meaningless. Instead only the effective radius as determined via a W75 model will be compared to the K62 results. Comparing the effective radii distributions as determined by K62 and W75 models (Figure 3.26), the two models appear to be in agreement. Both distributions peak at approximately the same effective radius ($r_h = 2.5$), which is comparable to the Milky Way (Harris, 1996 (2010 Edition)). Examining the effective radius of each cluster individually (Figure 3.27) we see that almost all of the clusters have similar effective radii as determined by both models. In contrast to the K66 comparison, there is no population of clusters that disagrees with the K62 effective radii. While both K66 and W75 models are dynamically motivated, K66 models prefer a sharp decrease in surface brightness to mark the tidal radius of a cluster. W75 models on the other hand prefer a more gradual decrease in surface brightness (See Chapter 2). Examination of the surface brightness profiles of the K66 clusters with effective radii smaller than K62 and W75

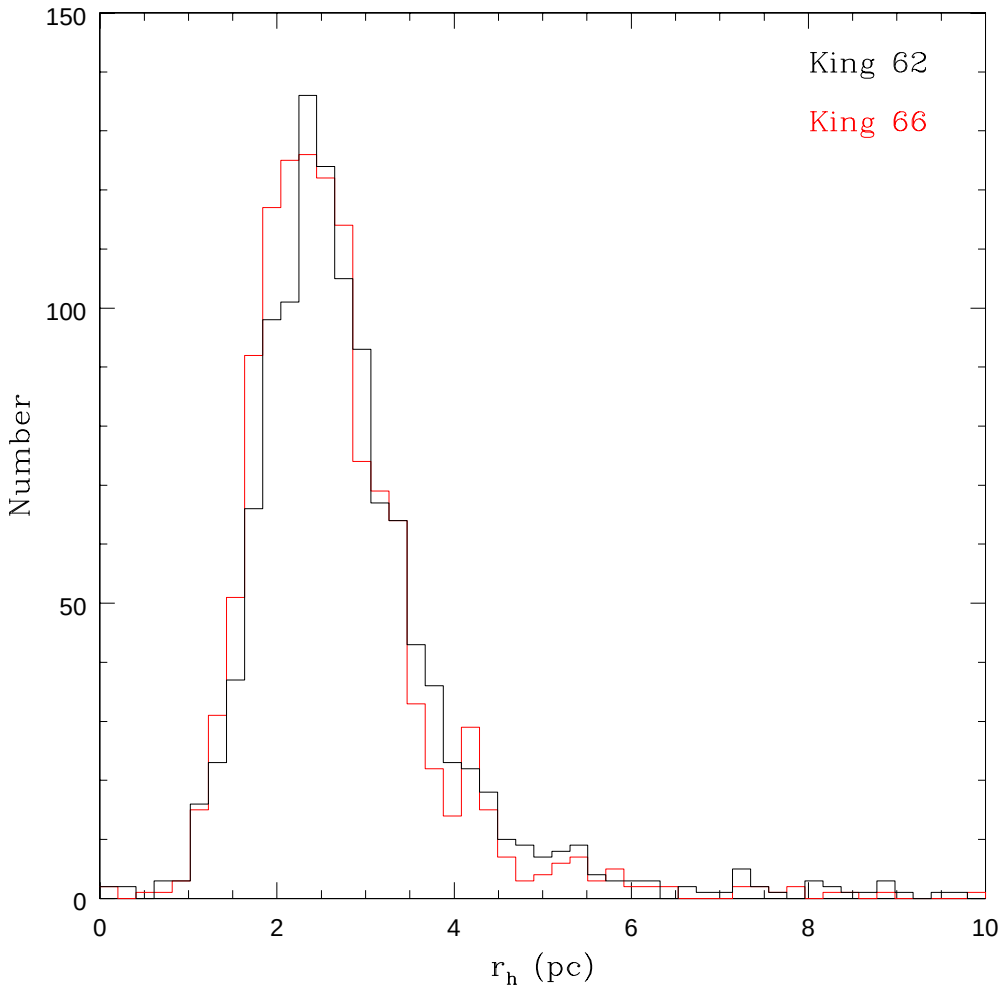

Figure 3.23: K62 (red) and K66 (black) effective radii distributions of observed globular clusters in the I-band.

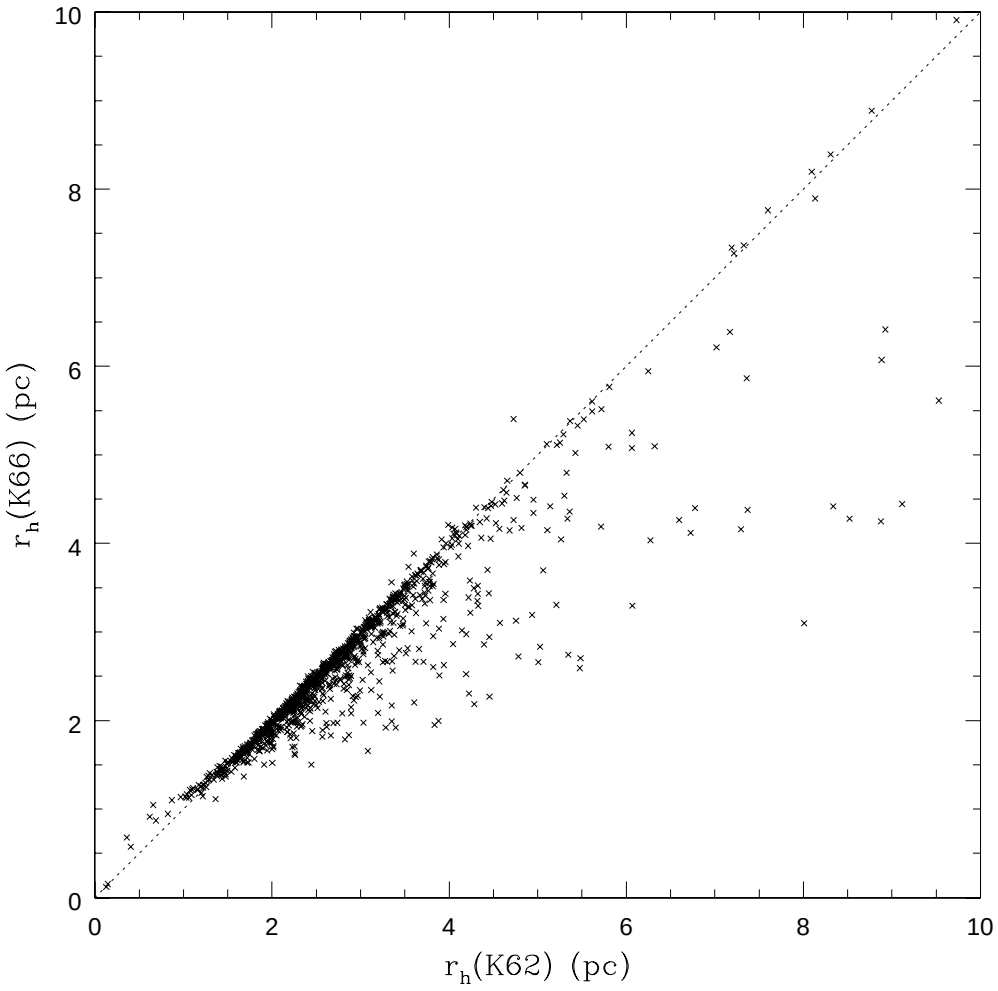

Figure 3.24: K62 vs. K66 effective radii of observed globular clusters in the I-band.

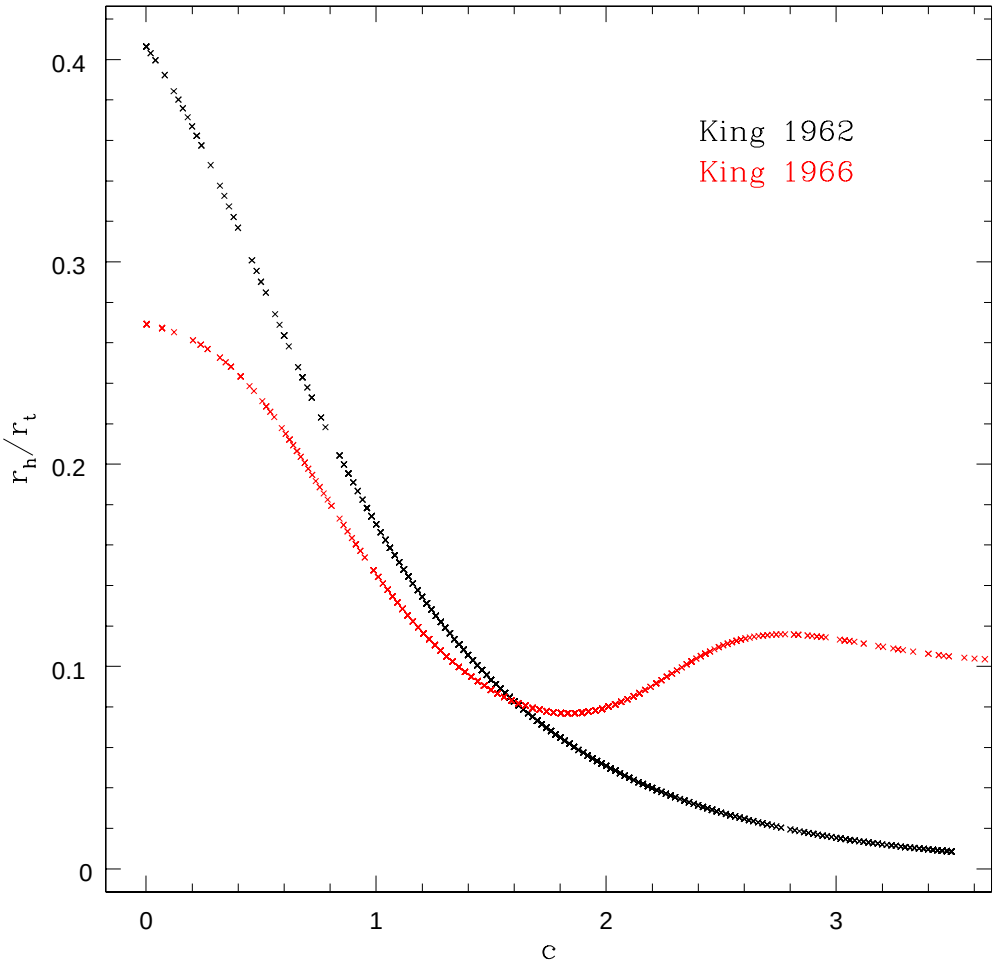

Figure 3.25: Ratio of effective radius to tidal radius vs. central concentration for clusters fit with K62 (black) and K66 (red) models.

(e.g Figure 3.30) shows that it is in fact clusters with gradual decreases in surface brightness that resulted in the population of clusters that had a poor agreement between K62 and K66 effective radii.

3.3.4 Sérsic (1968) Results

A final comparison was made between K62 and S68 models. As discussed in Chapter 2, similar to K62 models, S68 models are not dynamically motivated. Since S68 models are essentially power laws, it is impossible to predict a tidal radius as surface brightness does not go to zero. Therefore, only the effective radii of clusters as determined by K62 and S68 models can be compared. Furthermore, since the Sérsic index n is not comparable to cluster central concentration, there can be no central concentration comparison either. However, it is important to note that the distribution of the model fit Sérsic index is centered around 2, which from Chapter 2 is appropriate for globular clusters. Once the final cuts were made, the S68 model fits had a mean χ^2 of 0.30. S68 had the largest mean chi^2 of all four models, hence K62 models remain the best fit to the observations.

The effective radius distributions and individual effective radii are then compared in Figures 3.28 and 3.29 using the I dataset.

Both Figures 3.28 and 3.29 indicate that there is no apparent population of clusters with S68 effective radii larger than K62 effective radii, as seen in the K66 fit. This conclusion is supported by Figure 3.30, which illustrates how K62, W75, and S68 models predict similar cluster behaviour in their outer regions.

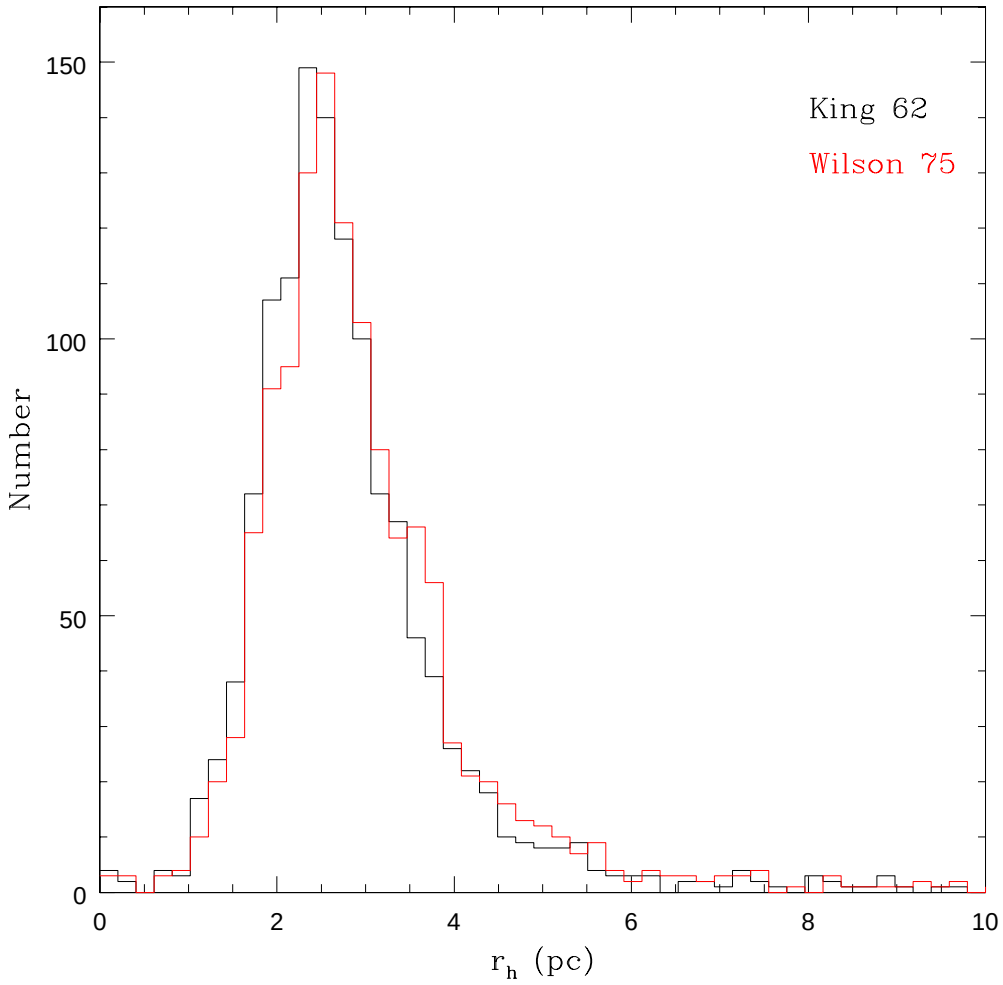

Figure 3.26: K62 (black) and W75 (red) effective radii distributions of observed globular clusters in the I-band.

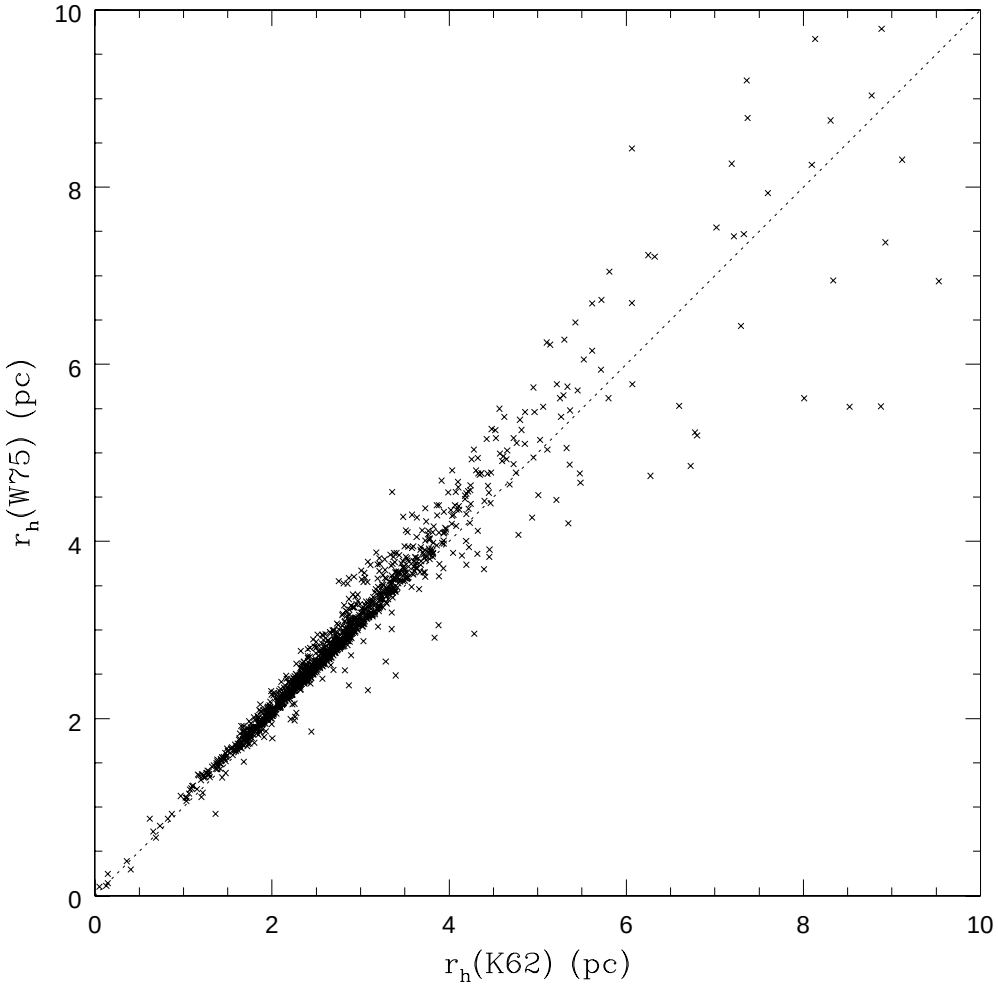

Figure 3.27: W75 vs. K62 effective radii of observed globular clusters in the I-band.

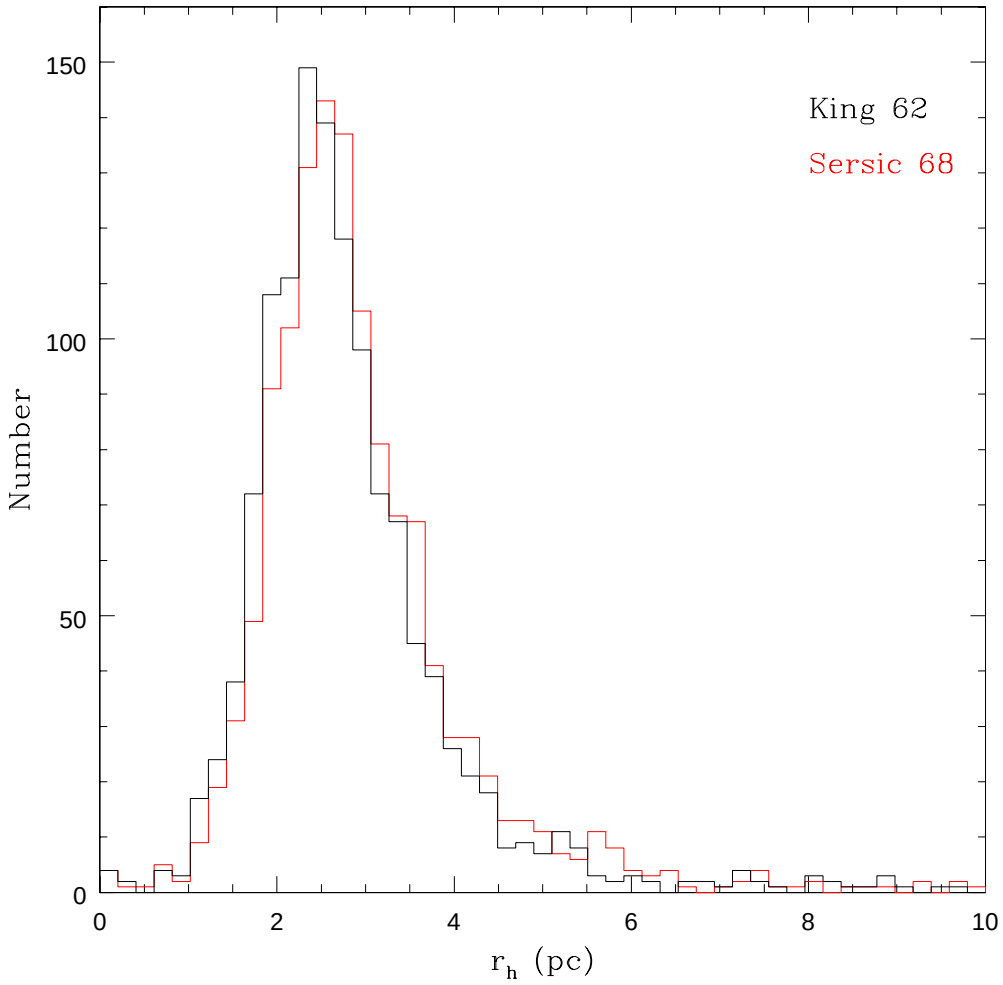

Figure 3.28: K62 (red) and S68 (black) effective radii distributions of observed globular clusters in the I-band.

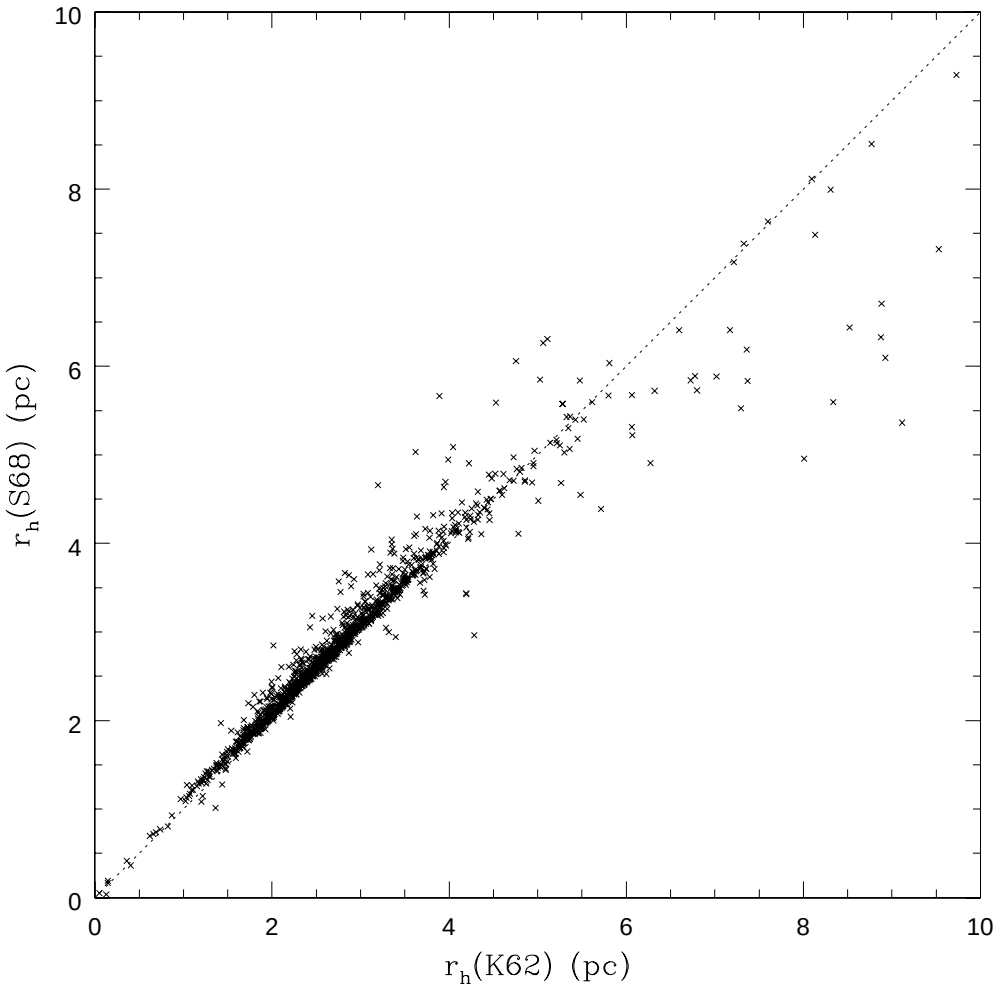

Figure 3.29: S68 vs. K62 effective radii of observed globular clusters in the I-band.

3.3.5 Uncertainty in Model Fits

Up until this point, we have been judging the results from K62, K66, W75, and S68 by comparing the mean chi^2 of each model fit, as well as the effective radii and central concentrations as determined by each model. What we have yet to consider is the uncertainty in each parameter. After each model was fit to the observations and objects were removed based on their χ^2, central concentration, and $r_h(V) - r_h(I)$, the mean and root mean square(RMS) $r_h(V) - r_h(I)$ and $c_v - c_i$ were determined. The results are summarized in Table 3.4. It is important to note that since the W75 central concentration and Sérsic index parameters are not the same as the K62 and K66 central concentration parameter, their mean and root mean square difference are not included in Table 3.4.

From the RMS of the K62 model fitting, we find that central concentrations have uncertainties of +/- 0.50. With central concentrations ranging from 0.5 to 3.0, an uncertainty of 0.50 is rather significant $(15 - 90\%)$. While K66 central concentrations have slightly less uncertainty, the K66 central concentration does not match either the K62 distribution or that of the Milky Way (Figure 3.21). This suggests that the central concentration values as determined by both the K62 and K66 models are unreliable. Therefore no comparisons between theoretical and observed central concentrations will be made.

Comparing the mean $r_h(V) - r_h(I)$ of each model, we find that K62 models have the smallest difference. Comparing the RMS $r_h(V) - r_h(I)$ of each model, we find that while the K62 and K66 models yield similar values, the W75 and

Table 3.4: Variance between I-based and V-based model parameters

	Value (pc)
K62	
Mean $r_h(V) - r_h(I)$	0.379
RMS $r_h(V) - r_h(I)$	0.518
Error in Mean	0.014
Mean $c_V - c_I$	0.389
RMS $c_V - c_I$	0.501
Error in Mean	0.014
K66	
Mean $r_h(V) - r_h(I)$	0.390
RMS $r_h(V) - r_h(I)$	0.509
Error in Mean	0.013
Mean $c_V - c_I$	0.307
RMS $c_V - c_I$	0.463
Error in Mean	0.012
W75	
Mean $r_h(V) - r_h(I)$	0.441
RMS $r_h(V) - r_h(I)$	0.588
Error in Mean	0.015
S68	
Mean $r_h(V) - r_h(I)$	0.434
RMS $r_h(V) - r_h(I)$	0.597
Error in Mean	0.016

S68 models yield much larger RMS $r_h(V) - r_h(I)$. This suggests that K62 and K66 effective radii have the least amount of uncertainty.

Ultimately, the result from the W75 and S68 model fitting suggests that the dynamically motivated K66 models are not the best method of determining cluster radii. The W75 and S68 effective radii of individual clusters both agree with K62 effective radii, disagreeing with K66 models which suggested a sub-population of clusters with $r_h(K66) < r_h(K62)$. As previously discussed, this discrepancy can be attributed to clusters which have brightness profiles that smoothly go to zero. Since K66 models prefer a sharp tidal cutoff, they do not accurately fit some clusters. Since K62 models are simple analytic functions, they better fit the brightness profile of each cluster as opposed to the more complicated K66 models which have the potential to diverge. This is supported by the fact that K62 model fits had the lowest mean chi^2 of all four models. Therefore the K62 results will be used when comparing theory to observations. The average of the V-magnitude and I-magnitude effective radii from the K62 model fits will be taken as our final estimates.

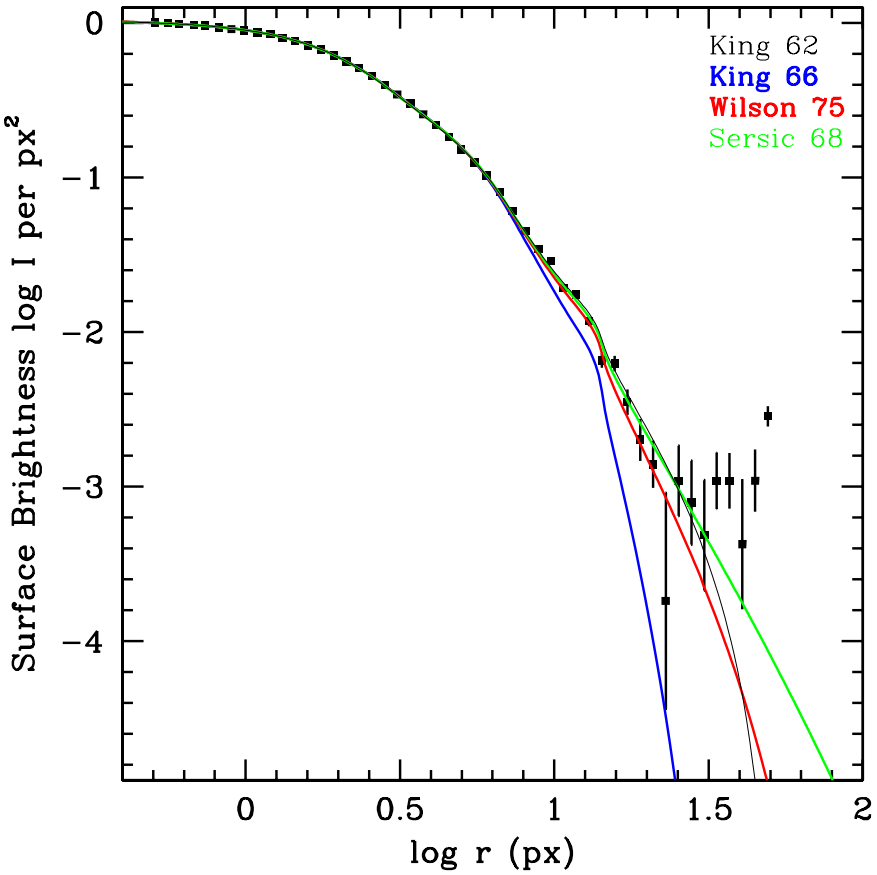

Figure 3.30: Background subtracted brightness distribution as determined by STSDAS ELLIPSE for a globular cluster in M87 in the I band (squares), fit with a K62 model (black), K66 model (blue), W75 model (red), and S68 model (green).

Bibliography

Binney, J. & Tremaine, S. 2008, Galactic Dynamics, 2^{nd} edition (Princeton, NJ, Princeton University Press)

Bird, S., Harris, W. E., Blakeslee, J. P., Flynn, C. 2010, A&A, 524, id.A71

Blakeslee, J. P., Anderson, K. R., Meurer, G. R., Bentez, N., Magee, D. 2003, ASPC, 295

Harris, W. E. 1996, AJ, 112, 1487, 2010 Edition

King, I. R. 1962, AJ, 67, 471

King, I. R. 1966, AJ, 71, 64

Madrid, J. P., Harris, W. E., Blakeslee, J. P., Gómez, M 2009, ApJ, 705, 237

McLaughlin, D. E., Barmby, P., Harris, W. E., Forbes, D.A., & Harris, G.L.H. 2008, MNRAS, 384, 563

Sérsic, J. L. 1968, Atlas de galaxias australes. Observatorio Astronomico, Cordoba

Tamura, N., Sharples, R. M., Arimoto, N., Onodera, M., Ohta, K., Yamada, Y., 2006, MNRAS, 373, 601

Wilson, C. P. 1975, AJ, 80, 175

Chapter 4

Simulating M87

Now that we have determined the observational tidal radii of nearly 2000 globular clusters in M87, we wish to simulate a globular cluster population orbiting within the galactic potential of M87, in order to calculate theoretical tidal radii. A direct comparison between the observational and theoretical distribution of globular cluster sizes with respect to projected galactocentric distance will illustrate the accuracy of the assumption that a cluster's observed limiting radius is equal to its theoretical tidal radius.

4.1 The Gravitational Field of M87

As stated in Chapter 2, this study will use the theoretical definition for the tidal radius of a globular cluster as derived by Bertin & Varri (2008). The first step towards using this equation for the calculation of theoretical tidal radii is to determine the gravitational field of M87.

McLaughlin (1999) has developed a mass model for the Virgo Cluster, which can be described by Equations 4.2 - 4.4. Since it is assumed that the Virgo Cluster is spherically symmetric and centered on M87, the mass model

is applicable to M87 as well. This assumption also makes the mass profile compatible with Equation 2.22, where Ψ_G is assumed to be spherically symmetric.

McLaughlin (1999) determined the stellar mass density profile of M87 from B-band photometry of de Vaucouleurs & Nieto (1978), assuming the stellar mass-to-light ratio of M87 is independent of radius. The mass profile extends out to a distance of approximately 100 kpc. Equation 4.3 was then determined by fitting the mass density profile with profiles of the type in Dehnen (1993) and Tremaine et al. (1994), which are models for spherical stellar systems of the form:

$$\rho_\eta(r) \propto \frac{1}{r^{3-\eta}(1+r)^{1+\eta}} \qquad 0 < \eta \leq 3 \tag{4.1}$$

As summarized in McLaughlin (1999), many additional sources were used to compile a mass profile for Virgo beyond 100 kpc. These sources include x-ray observations of the hot gas in the extended M87 halo, dwarf elliptical galaxies, and early-type Virgo galaxies. Combining the data, a Navarro-Frenk-White profile (Navarro,Frank & White, 1997) was used to fit the dark matter halo (Equation 4.4).

These mass models are defined in Equations 4.2-4.4 and illustrated in Figure 4.1. Since we are only interested in the mass profile of M87 and not the entire Virgo cluster, we focus on the inner 100 kpc of the mass profile as this is the limit of the stellar observations made by de Vaucouleurs & Nieto (1978) and our observed globular clusters only go out to 12 kpc.

$$M_{total}(r) = M_{stars}(r) + M_{dark}(r) \tag{4.2}$$

$$M_{stars}(r) = 8.10 \times 10^{11}\ M_{\odot}\ [\frac{(r/5.1kpc)}{(1 + r/5.1kpc)}]^{1.67} \tag{4.3}$$

$$\begin{aligned} M_{dark}(r) =& 7.06 \times 10^{14}\ M_{\odot} \\ & \times [\ln(1 + r/560kpc) - \frac{(r/560kpc)}{(1 + r/560kpc)}] \end{aligned} \tag{4.4}$$

The mass distribution of M87 (Equation 4.2) can then be used to determine the gravitational potential as a function of galactocentric distance. Newton's theorems regarding the gravitational potential of a spherically symmetric distribution of matter are (Binney & Tremaine, 2008):

1. A body that is inside a spherical shell of matter experiences no net gravitational force from that shell.

2. The gravitational force on a body that lies outside a spherical shell of matter is the same as it would be if all the shell's matter were concentrated into a point at its center.

Considering a spherical shell of mass m located at a distance r from the center of the sphere, Newton's theorems suggest that acceleration interior to the shell is zero, and acceleration outside of the shell is $-Gm/r^2$. Hence the potential for a spherically symmetric mass distribution can be taken to be:

$$\begin{aligned} \Phi_G(r) &= -G \int_r^{\infty} M(r)/r^2\, dr \\ &= G \int_{R_0}^{r} M(r)/r^2\, dr \end{aligned} \tag{4.5}$$

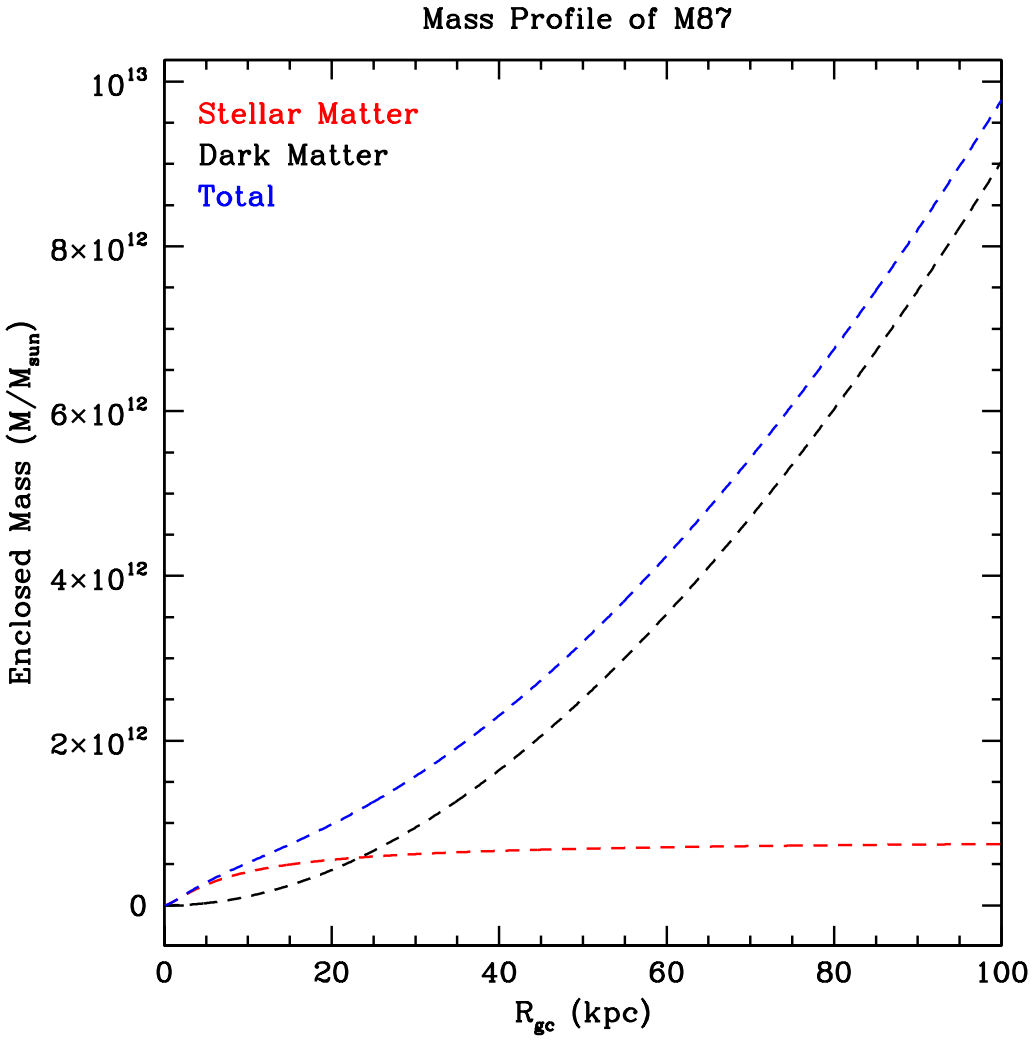

Figure 4.1: Mass model for the central regions of the Virgo cluster showing stellar mass (red), dark matter mass (black), and total mass (blue) distributions. Adopted from McLaughlin (1999).

where R_0 is a sufficient distance from the center of the distribution such that $\Phi(R_0) = 0$ (Binney & Tremaine, 2008).

Utilizing Equations 4.2, 4.3, and 4.4 for M(r), the spherical potential of M87 is derived to be:

$$\Phi_G = \Phi_{Gstars} + \Phi_{Gdark} \tag{4.6}$$

$$\begin{aligned} \Phi_{Gstars} =& G\ 8.10 \times 10^{11}\ M_\odot \\ & \times ((\frac{1}{0.67})(5.1kpc + r)\frac{(\frac{r}{5.1kpc+r})^{1.67}}{(r \times 5.1kpc)} \\ & - (\frac{1}{0.67})(5.1kpc + R_0)\frac{(\frac{R_0}{5.1kpc+R_0})^{1.67}}{(R_0 \times 5.1kpc)}) \end{aligned} \tag{4.7}$$

$$\begin{aligned} \Phi_{Gdark} =& -G\ 7.06 \times 10^{14}\ M_\odot \\ & \times (\frac{\ln(1 + \frac{r}{560kpc})}{r} - \frac{\ln(1 + \frac{R_0}{560kpc})}{R_0}) \end{aligned} \tag{4.8}$$

Since the tidal radius is only dependent on the spatial gradient and second derivative of the potential and not the potential directly, we do not need to determine a value for R_0.

4.2 Input Parameters

With the gravitational potential of M87 in hand (Equations 4.7 and 4.8), it is now possible to simulate a globular cluster population that would exist within such a potential. When simulating such a population, the goal is to

have the clusters in the simulation have the same characteristics as the observed clusters in M87. This allows us to determine an expected observational relationship between tidal radii and projected galactocentric distance.

Each globular cluster was given a position (R, θ, ϕ), velocity (v_r, v_θ, v_ϕ), mass and central concentration which were each drawn from an appropriate distribution from observations of M87. The distribution parameters used in the simulation are summarized in Table 4.1. The radial distribution was taken from Harris (2009), who found that the projected radial profile of the blue and red globular cluster subpopulations could be fit with a standard Hubble profile (Equation 4.9) relating density (σ_{cl}) to projected distance (R). The appropriate values for σ_0, R_o, and a are listed in Table 4.1 for the blue and red subsystems. The angular distribution was assumed to be spherically symmetric.

$$\sigma_{cl}(R) = \sigma_0/(1 + \frac{R}{R_0})^{-a} \tag{4.9}$$

The mass distribution of globular clusters was taken from the near universal luminosity function for globular clusters. The luminosity function is approximately Gaussian, symmetric about an absolute visual magnitude of -7.3, with a standard deviation of 1.3 (e.g. Brodie & Strader (2006)). Assuming a mass-to-light ratio of 2 (e.g. McLaughlin & van der Marel (2005)), this results in a Gaussian mass distribution about a mean of 5.5 and a standard deviation of 0.52 in $\log(M/M_\odot)$. In assigning a central concentration parameter to each globular cluster, the distribution of central concentrations in the Milky Way (Harris, 1996 (2010 Edition)) was used to indicate the appropriate distribution

(Figure 4.2). Ignoring clusters with $c > 2.5$ (believed to have undergone core collapse), a Gaussian distribution with a mean of 1.5 and standard deviation of 0.4 fits the data. This Gaussian distribution is plotted with the Milky Way data as a solid line in Figure 4.2.

The velocity dispersion is taken from the observed line of sight velocity dispersion of globular clusters in M87 (Côté et al., 2001). We have initially assumed the distribution of orbits to be isotropic, such that the anisotropy parameter discussed in Chapter 2 was zero. Hence the radial, theta, and phi components of each globular cluster's velocity all come from the same velocity dispersion. This is a reasonable initial assumption as the solved orbits of Milky Way globular clusters (Dinescu et al., 1999; Casetti-Dinescu et al., 2007) do not indicate a preference towards circular orbits. While it is a logical first step to assume the population is isotropic in velocity, Section 4.6 will explore how varying the parameter β affects tidal radii.

Exactly 10000 globular clusters were simulated. Not only does this provide a statistically significant amount of clusters, but is also an approximation of the number of clusters within 100 kpc of M87 (Harris, 2009). Half were designated as "red" clusters and had positions drawn from the red Hubble profile from Harris (2009). The second half were designated as "blue" clusters and were drawn from the appropriate Harris (2009) observed parameters. The radial distribution (Figure 4.3), mass distribution (Figure 4.4), radial velocity distribution (Figure 4.5), central concentration distribution (Figure 4.6) are all illustrated. Additionally, converting each cluster's position in spherical coordinates to Cartesian coordinates, we can assume the $x-y$ plane is the plane

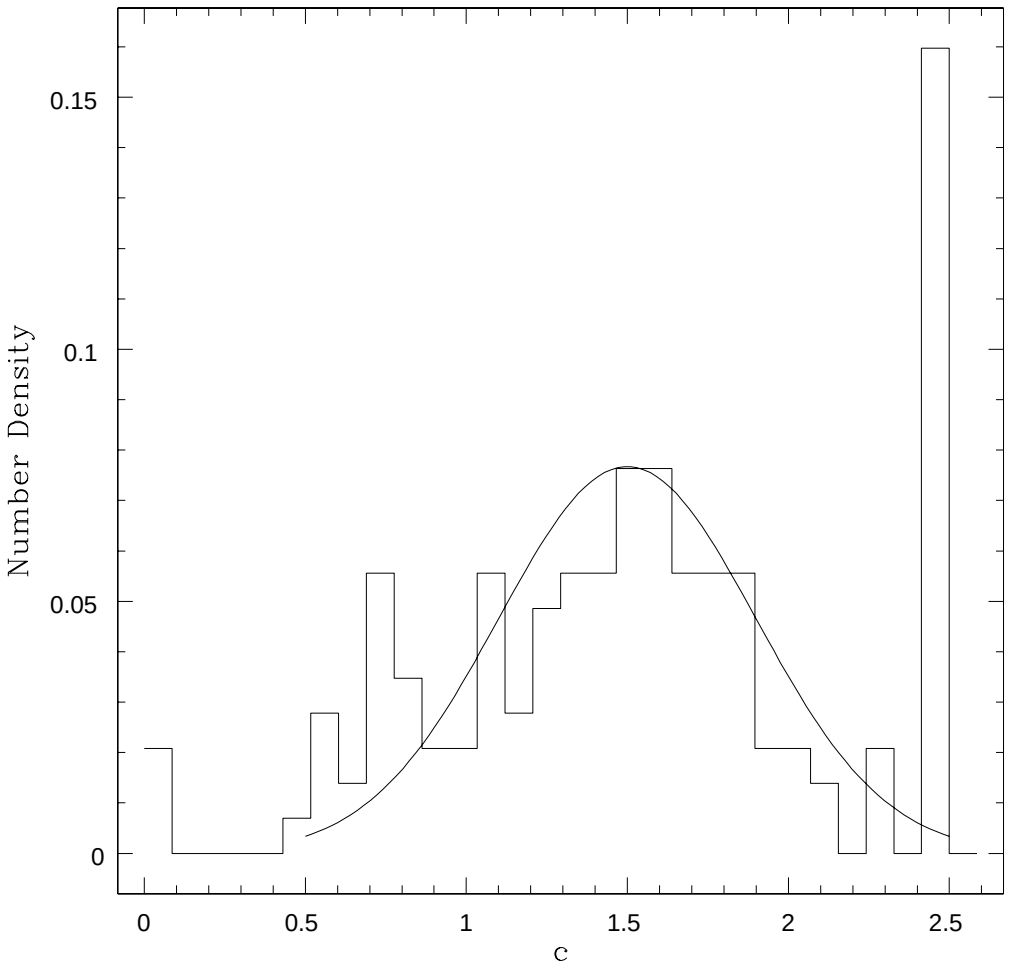

Figure 4.2: Distribution of globular cluster central concentrations in the Milky Way (Histogram). The solid line represents a Gaussian fit with a mean of 1.5 and standard deviation of 0.4. Data taken from Harris (1996) (2010 Edition).

Table 4.1: Simulated Globular Cluster Population Input Parameters

Parameter	Value
Radial Distribution	Hubble Profile
Blue Population	
σ_0	66 arcmin^{-2}
R_0	2.0'
a	1.8
Red Population	
σ_0	150 arcmin^{-2}
R_0	1.2'
a	2.1
Angular Distribution	Spherically Symmetric
Mass-To-Light Ratio	M/L = 2
Mass Distribution	Gaussian
$\langle log(M/M_0) \rangle$	5.5
$\sigma_{log(M/M_0)}$	0.52
Velocity Dispersion	Gaussian
$\langle v \rangle$	-19 km/s
σ_v	401 km/s
β	0
Central Concentration	Gaussian
$\langle c \rangle$	1.5
σ_c	0.4

of the sky. Figure 4.7 then illustrates the simulated population as projected onto the plane of the sky.

4.3 Orbit Integration

As discussed in Chapter 2, it is incorrect to calculate the theoretical tidal radius of each globular cluster based on its present galactocentric position. Globular clusters will not necessarily have circular orbits, and more than likely have elliptical orbits. In this case, the tidal radius will be dependent on the globular cluster's perigalactic distance, where the tidal field of the galaxy is strongest.

To determine the perigalactic distance of each simulated globular cluster, the globular cluster is assumed to be a point mass moving in an orbital plane in the static spherical potential of M87. The derivation of perigalactic distance is taken from Binney & Tremaine (2008), who derive the pericenter distance and apocenter distance of a star orbiting in a centrally directed, static spherical potential. The Lagrangian per unit mass of such a globular cluster is then:

$$Ł = \frac{1}{2}\left[\dot{r}^2 + (r\dot{\varphi})^2\right] - \Psi(r) \tag{4.10}$$

where r is the globular cluster's present distance from the center of the galaxy and $\Psi(r)$ is the gravitational potential of the galaxy. The equations of motion are:

$$0 = \ddot{r} - r\dot{\varphi}^2 + \frac{d\Psi(r)}{dr} \tag{4.11}$$

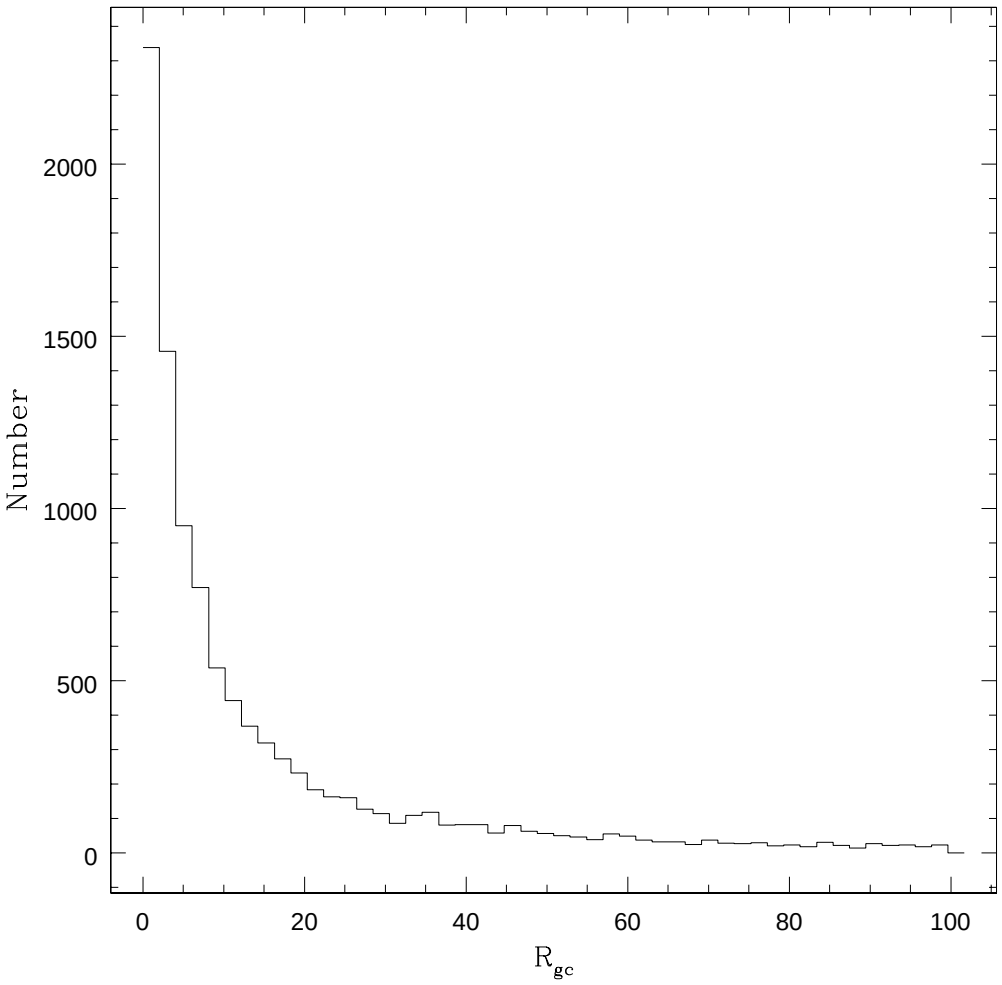

Figure 4.3: Radial distribution of simulated globular cluster population.

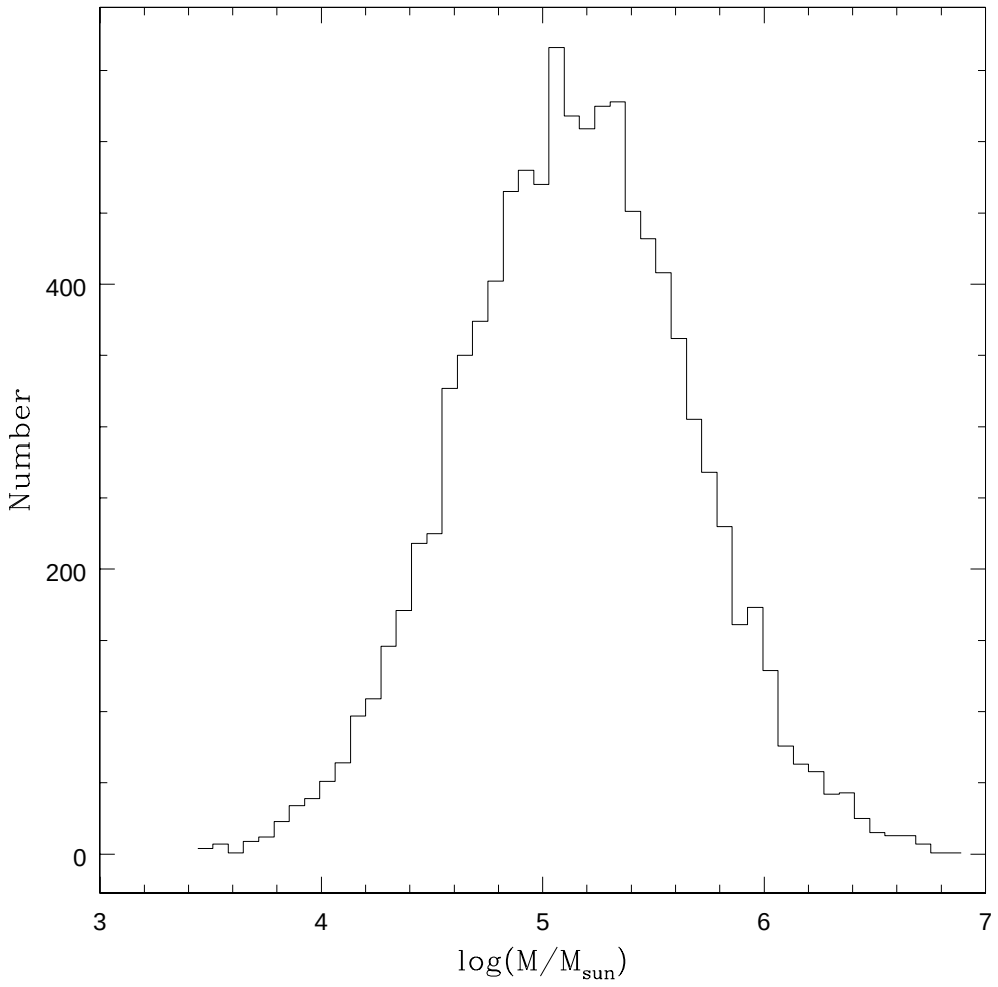

Figure 4.4: Mass distribution of simulated globular cluster population.

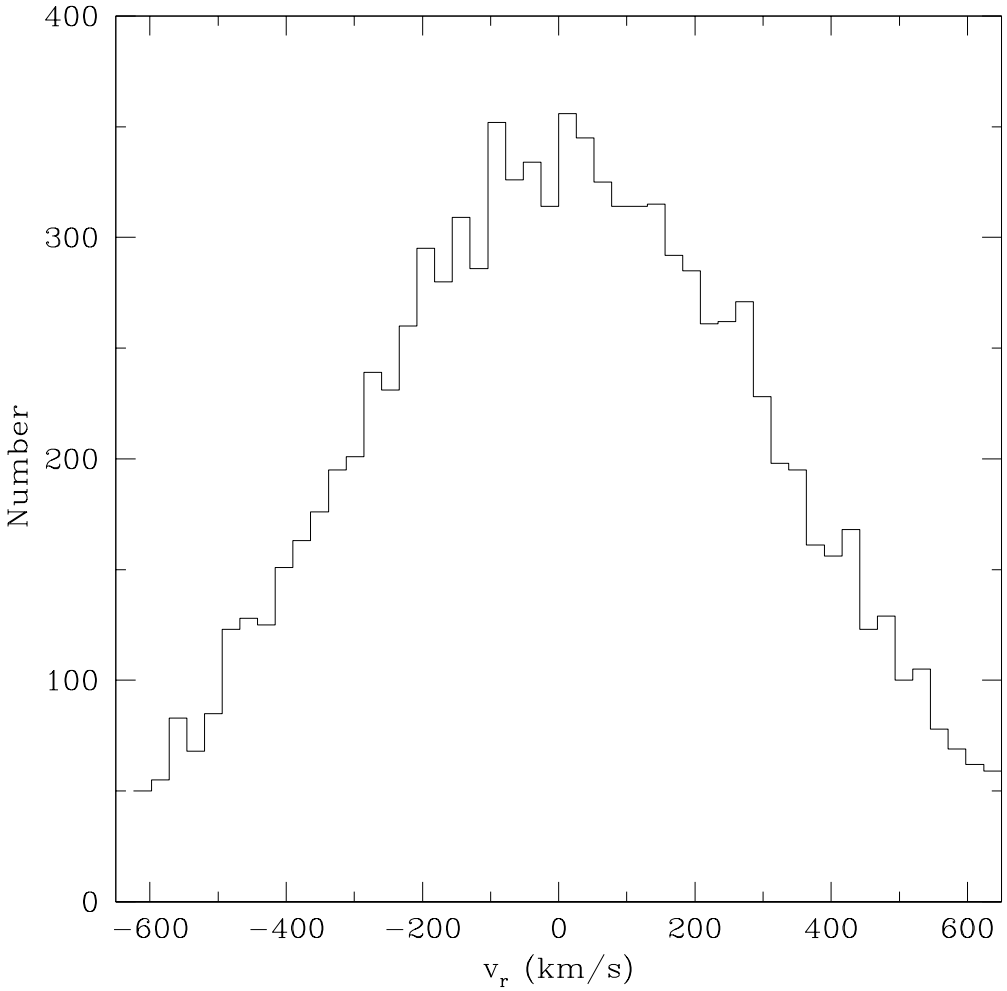

Figure 4.5: Radial velocity distribution of simulated globular cluster population.

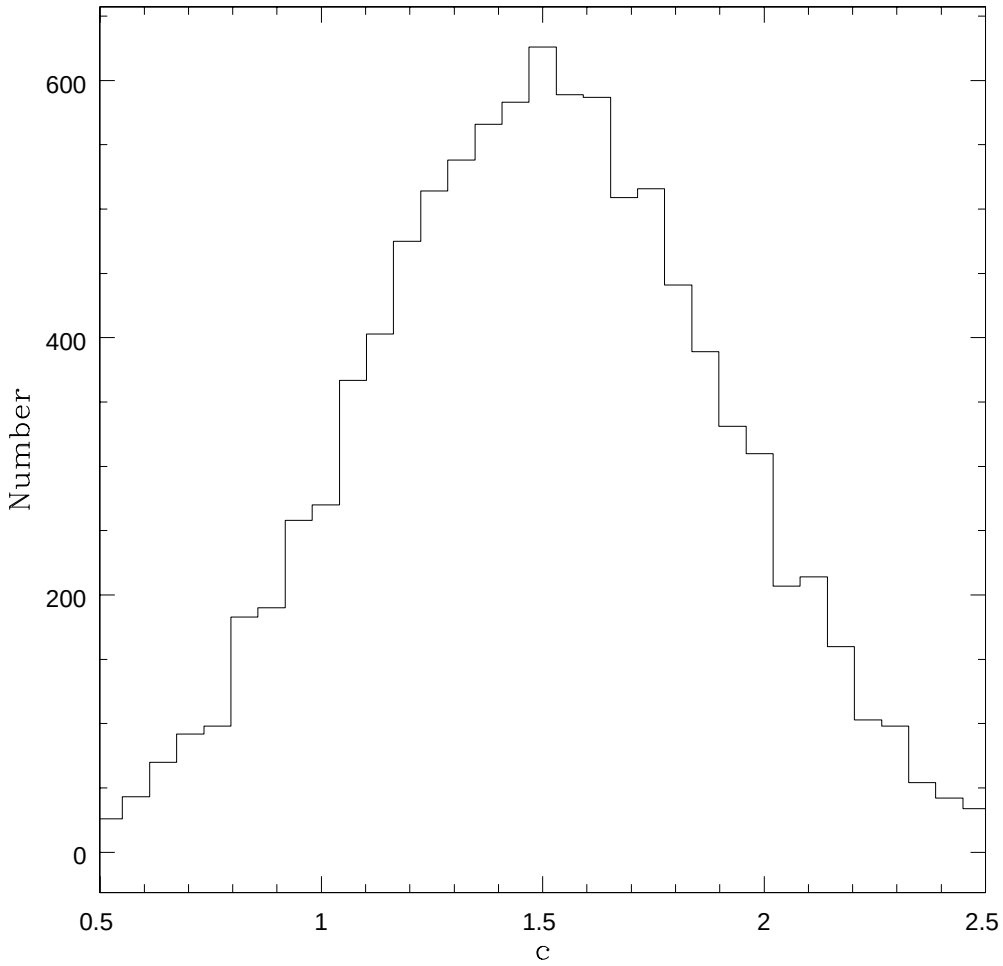

Figure 4.6: Central concentration distribution of simulated globular cluster population.

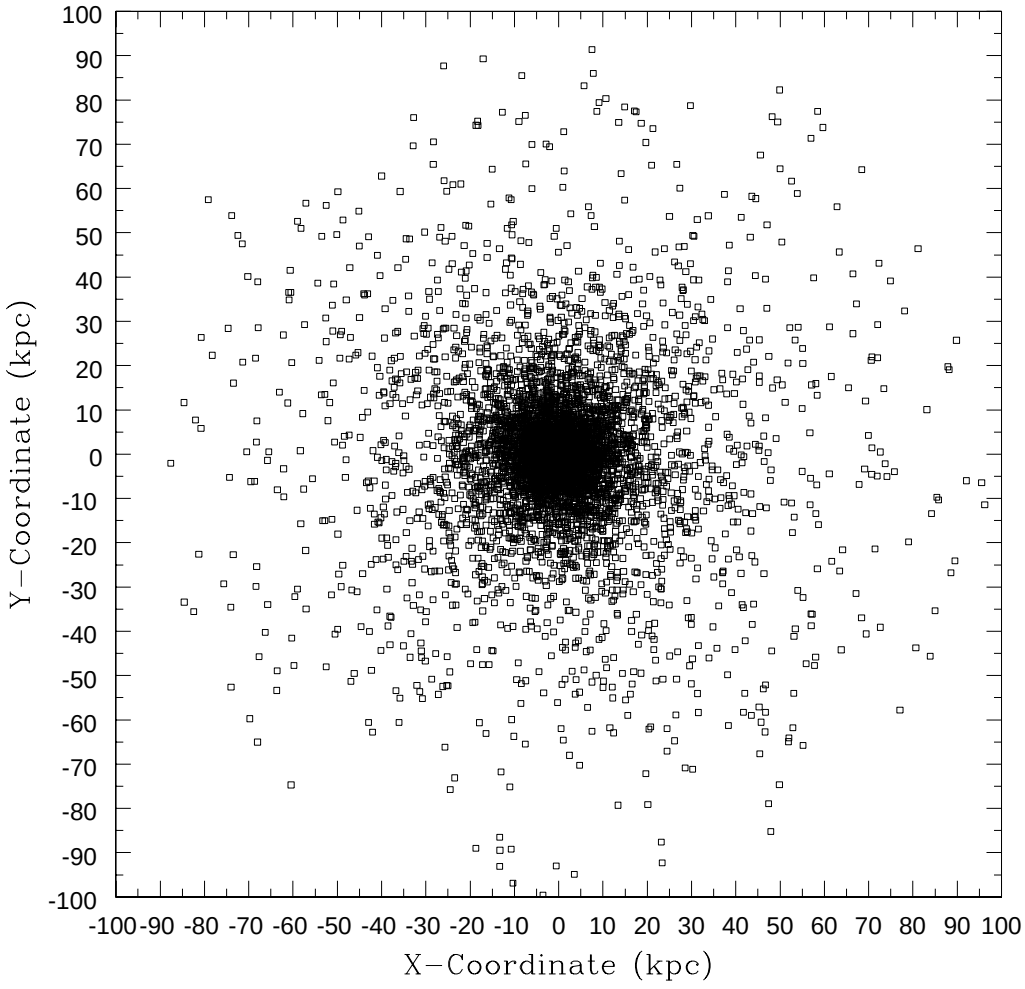

Figure 4.7: Projected view of simulated globular cluster population.

$$0 = \frac{d\ (r^2\dot{\varphi})}{dt} \tag{4.12}$$

Equation 4.12 implies that $r^2\dot{\varphi}$ is constant. This constant is actually the angular momentum per unit mass (L) of the globular cluster. Rewriting this relationship as:

$$\frac{d}{dt} = \frac{L}{r^2}\ \frac{d}{d\varphi} \tag{4.13}$$

and substituting into Equation 4.11 we get:

$$\frac{L^2}{r^2}\ \frac{d}{d\varphi}(\frac{1}{r^2}\ \frac{dr}{d\varphi}) - \frac{L^2}{r^3} = -\frac{d\Psi}{dr} \tag{4.14}$$

For $u = 1/r$, we can put the above equation into the form:

$$\frac{d^2u}{d\varphi^2} + u = \frac{1}{L^2u^2}\ \frac{d\Psi}{dr}(\frac{1}{u}) \tag{4.15}$$

Equation 4.15 can then be used to determine the radial energy equation. Multiplying Equation 4.15 by $du/d\varphi$ and integrating over φ results in:

$$(\frac{du}{d\varphi})^2 + \frac{2\Psi}{L^2} + u^2 = constant = \frac{2E}{L^2} \tag{4.16}$$

The radial energy equation can also be derived with Hamiltonians. With Equation 4.10 to determine the momenta ($p_q = d\text{Ł}/d\dot{q}$), the Hamiltonian per unit mass is then:

$$\begin{aligned} H(r, p_r, p_\varphi) &= p_r\dot{r} + p_\varphi\dot{\varphi} - Ł \\ &= \frac{1}{2}\ (p_r^2 + p_\varphi^2/r^2) + \Psi(r) \\ &= \frac{1}{2}(\frac{dr}{dt})^2 + \frac{1}{2}(r\ \frac{d\varphi}{dt})^2 + \Psi(r) \end{aligned} \tag{4.17}$$

Comparing the Hamiltonian above to Equation 4.16, it is clear that the constant E is the energy of the cluster's orbit, which is essentially the numerical value of the Hamiltonian. With a globular cluster's current radius, radial velocity and tangential velocity, the constants E and L in Equation 4.16 can be found.

For a bound orbit, $du/d\varphi = 0$. Under that assumption, Equation 4.16 then becomes:

$$u^2 + \frac{2[\Psi(\frac{1}{u}) - E]}{L^2} = 0 \tag{4.18}$$

The roots of Equation 4.18 represent the pericenter distance and apocenter distance between which the cluster oscillates. Due to the complicated nature of the gravitational potential of M87 (Equations 4.7 and 4.8), once E and L for a simulated globular cluster are found, the roots of Equation 4.18 must be found numerically.

This process can be illustrated with a sample globular cluster taken from the simulation. The simulated parameters of the sample globular cluster are listed in Table 4.2. This sample cluster will also be used for future examples.

Figure 4.8 illustrates Equation 4.18 for the sample globular cluster. The roots of this function were numerically determined to be 13.00 kpc and 65.83

Table 4.2: Simulated Parameters of a Sample Globular Cluster in M87

Parameter	Value
Current Galactocentric Distance	18.63 kpc
Angular Position (θ,ϕ)	-55.56^o,53.35^o
Mass (Log($M/M_\odot$))	4.07
Radial Velocity	-510.44 km/s
Tangential Velocity ($\sqrt{v_\varphi^2 + v_\theta^2}$)	626.62 km/s
Central Concentration	1.67

kpc, yielding the pericenter and apocenter distances respectively. The roots also agree visually with Figure 4.8, as the dotted vertical lines represent the roots and the dotted horizontal line shows y=0.

It is also of interest to determine a cluster's radial velocity as a function of distance and its radial period. Combining Equation 4.17 with the previously established fact that $L = r^2\dot{\varphi}$, we find that:

$$(\frac{dr}{dt})^2 = 2(E - \Psi(r)) - (L/r)^2 \tag{4.19}$$

$$\frac{dr}{dt} = \pm\sqrt{2(E - \Psi(r)) - (L/r)^2} \tag{4.20}$$

where dr/dt is the cluster's radial velocity, and the $\pm$ is a result of the fact that a cluster moves towards and away from the galaxy's center during different times of its orbit. Utilizing the simulated globular cluster from Table 4.2, the cluster's radial velocity as a function of its galactocentric distance is illustrated below in Figure 4.9.

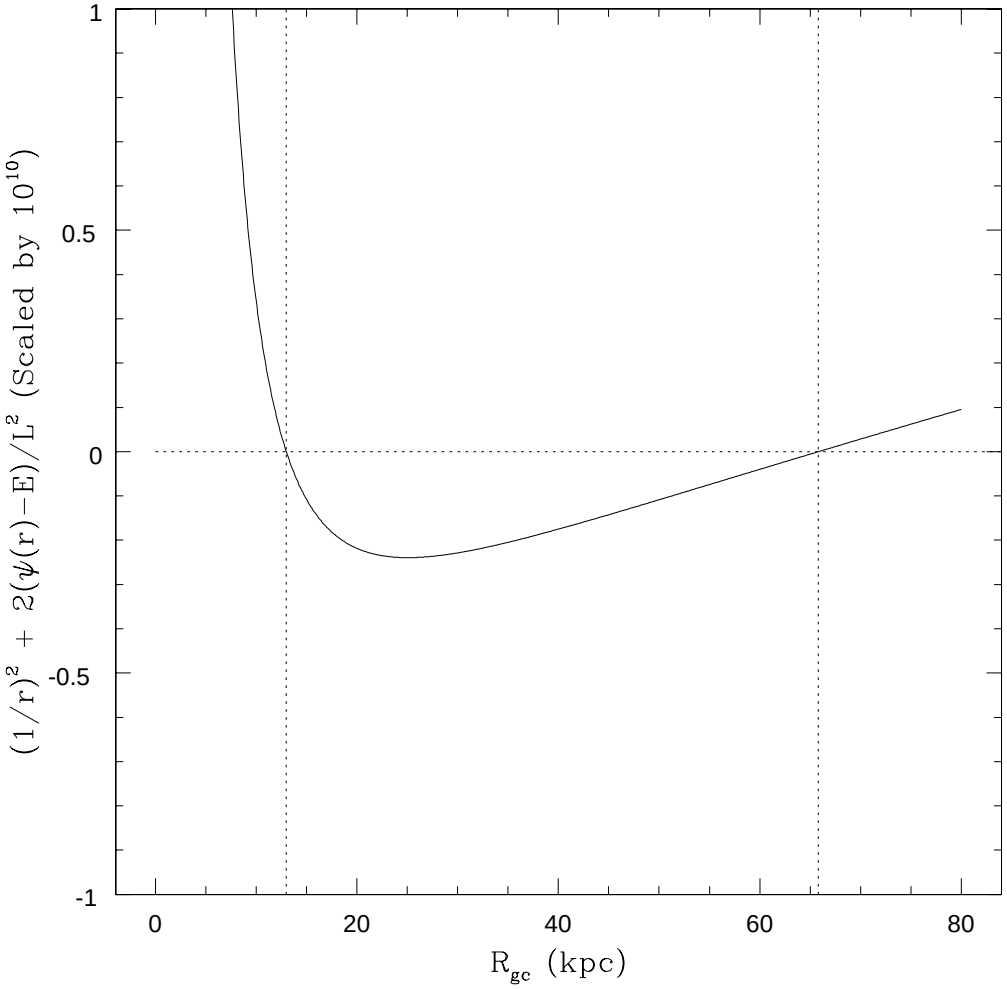

Figure 4.8: Plot of Equation 4.18 for a simulated globular cluster orbiting in the potential of M87. The values on the y-axis are scaled up by 10^{10}.

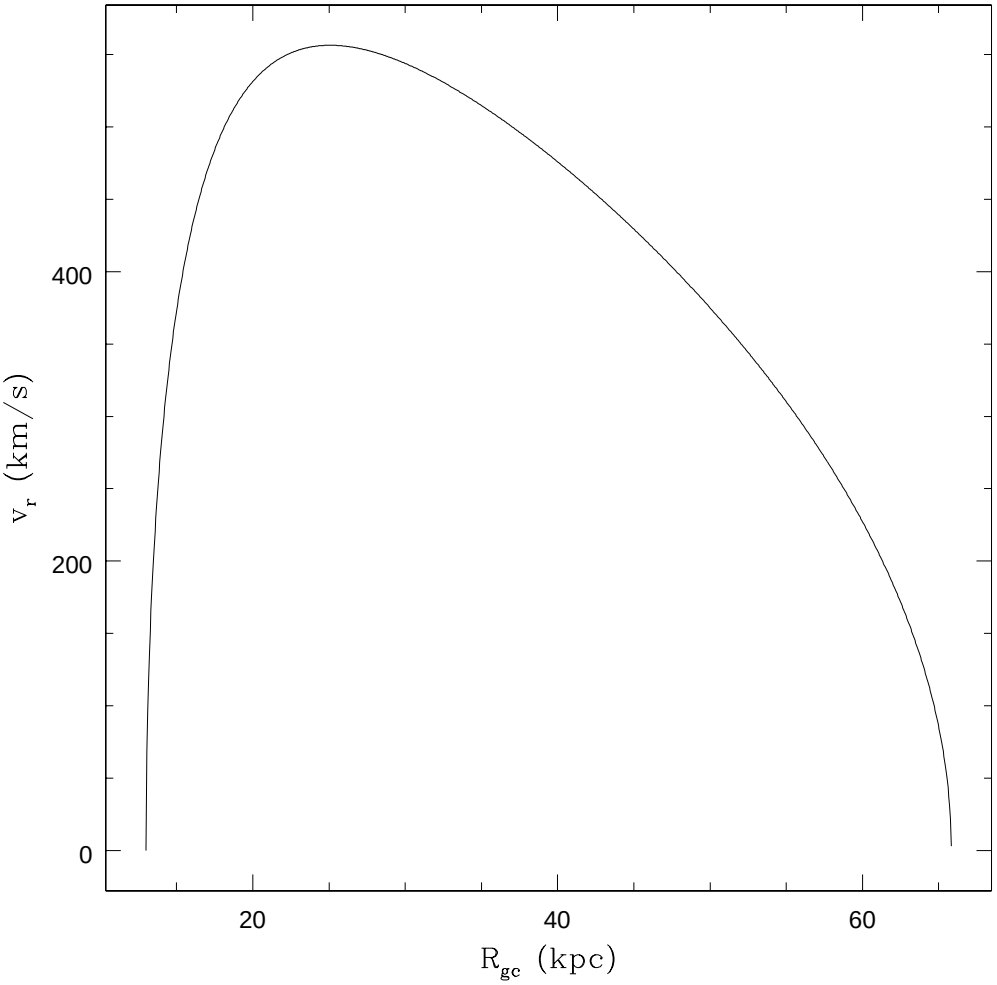

Figure 4.9: Globular cluster's radial velocity at all galactocentric distances of its orbit.

Rearranging Equation 4.20, we can now solve for the radial period of a globular cluster.

$$\begin{aligned} T_r &= \int_0^{T_r} dt \\ &= \int_{r_p}^{r_{ap}} 1/\sqrt{2(E - \Psi(r)) - (L/r)^2}\, dr \end{aligned} \tag{4.21}$$

Plotting the function inside the integral of Equation 4.21 in Figure 4.10, the area underneath the plot represents the cluster's radial period. The plot behaves as expected, as there is more area underneath the curve at higher galactocentric distances as the cluster spends a longer portion of its orbit near apocenter. The equation can then be numerically integrated between the cluster's perigalactic and apocentric distances to determine its radial period. The radial period for the simulated globular cluster was determined to be 1.65434×10^8 years.

Repeating this process for the entire simulated M87 globular cluster population, Figure 4.11 shows the present distance of a globular cluster (x-axis) compared to its perigalactic distance (y-axis). As expected, a globular cluster's perigalactic distance is less than or equal to its present distance from the center of the galaxy. Similarly, Figure 4.12 shows how apogalactic distance compares with present distance. Not only is the apogalactic distance greater then or equal to present distance, but the majority of clusters appear to be very near their apocenter. This is also expected as orbiting bodies on non-circular orbits spend a longer portion of their orbit closer to apocenter than pericenter.

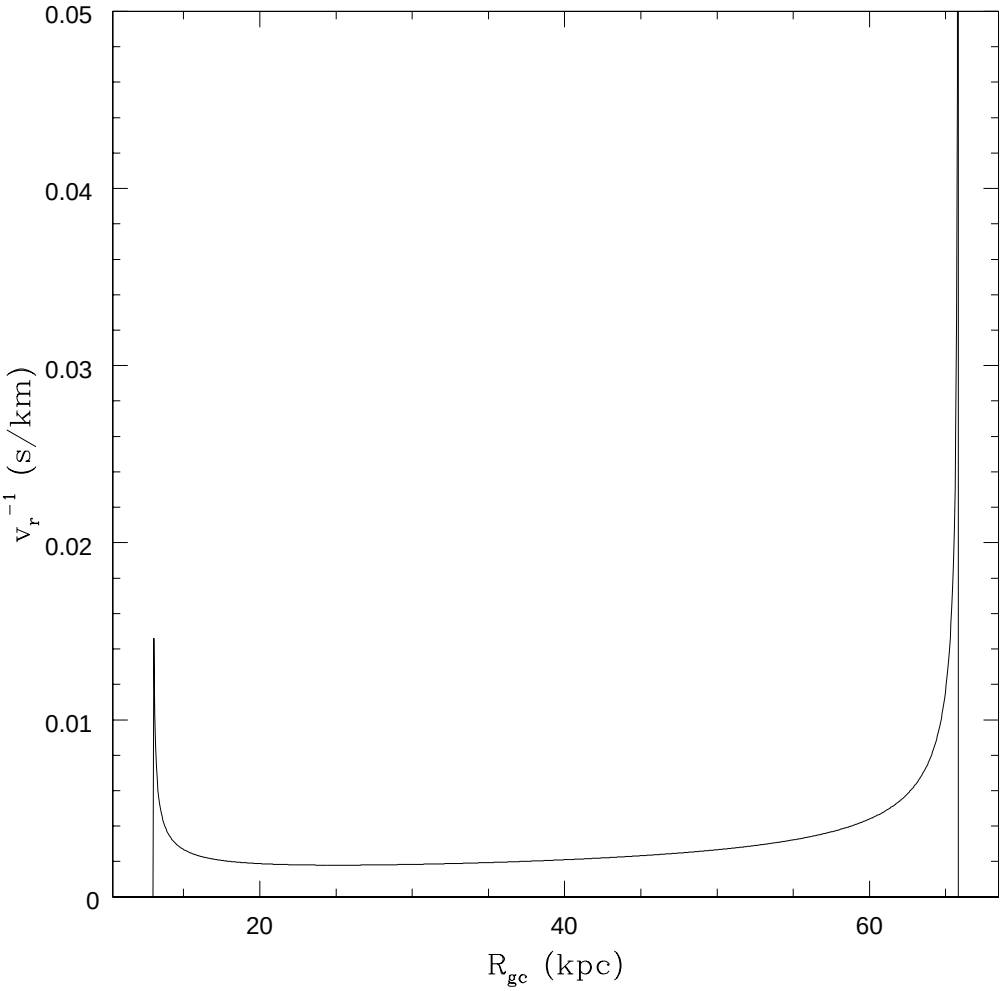

Figure 4.10: Function inside integral of Equation 4.21.

The perigalactic and apogalactic distances can also be used to determine the eccentricity of each cluster's orbit, which is a measure of how circular or elliptical the orbit of the cluster is. Equation 4.22 gives the mathematical definition of eccentricity.

$$e = \frac{r_{ap} - r_p}{r_{ap} + r_p} \tag{4.22}$$

Equation 4.22 can be applied to each simulated cluster, and the eccentricity distribution of the simulated globular cluster population (Figure 4.13) can be found. This distribution is roughly symmetric, and centered at an average eccentricity of 0.5. This is expected since globular cluster velocities were selected assuming the velocity dispersion is isotropic. Finally, Figure 4.14 illustrates the distribution of radial periods for the simulated globular clusters.

From Figure 4.14 we see that the majority of clusters have periods between 10^6 and $10^{8.5}$ years, however there is a significant number of clusters with smaller radial periods. As seen in Figure 4.15, these clusters with small radial periods have very small perigalactic distances. It is possible that some of these low period, low perigalactic distance clusters should be removed from the simulation as they will have either been destroyed by dynamical friction or possibly ejected from the galaxy. This is explored further in Section 4.5.

4.4 Tidal and Effective Radii Calculation

From the equation for the galactic potential of M87 (Equations 4.7 and 4.8) , it is possible to calculate all the elements of Equation 2.22 (Ω^2, κ^2, and

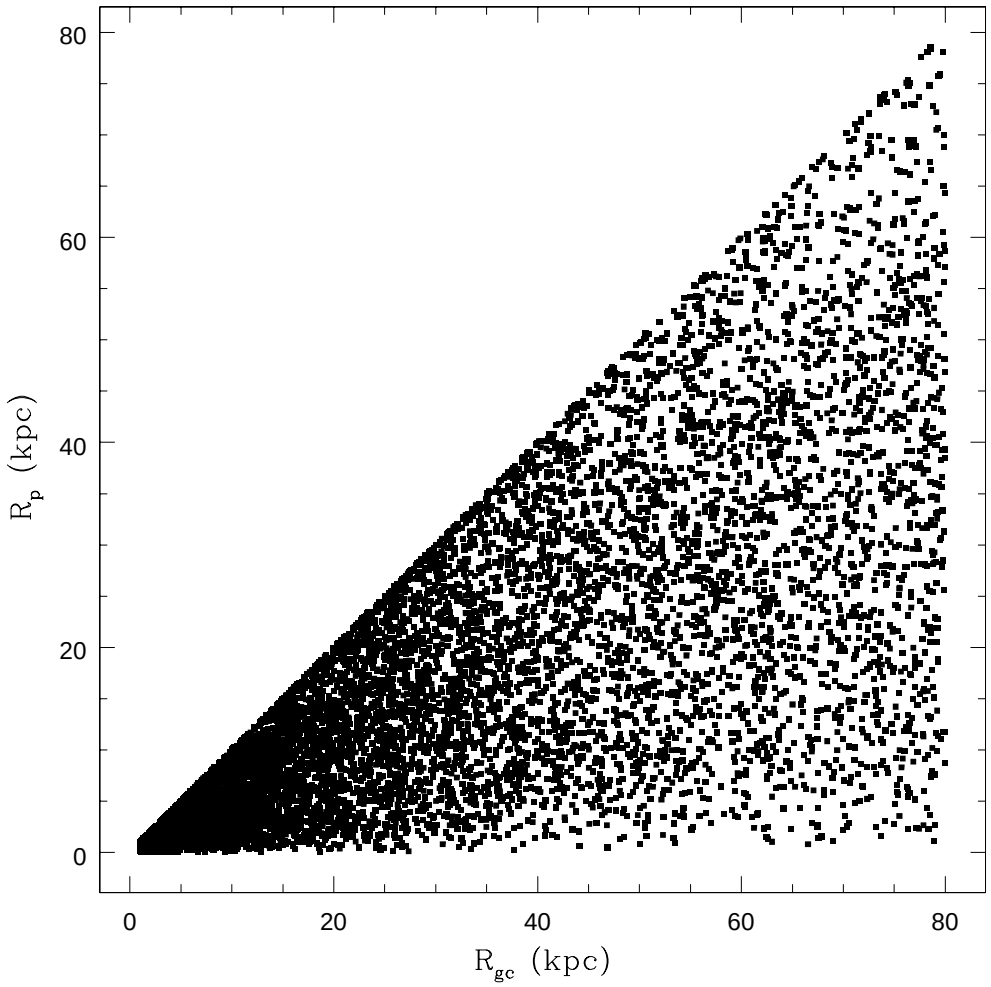

Figure 4.11: Perigalactic distance of each simulated globular cluster compared with its current galactocentric distance.

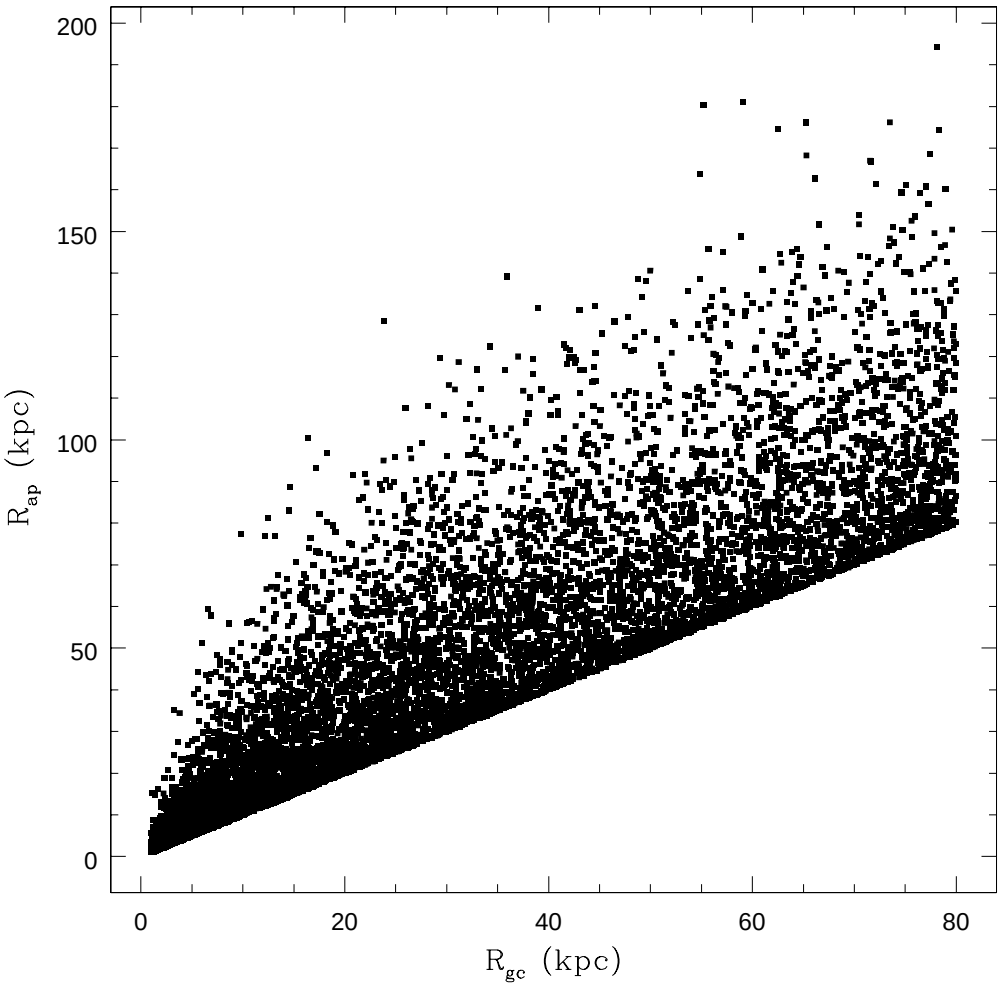

Figure 4.12: Apogalactic distance of each simulated globular cluster compared with its current galactocentric distance.

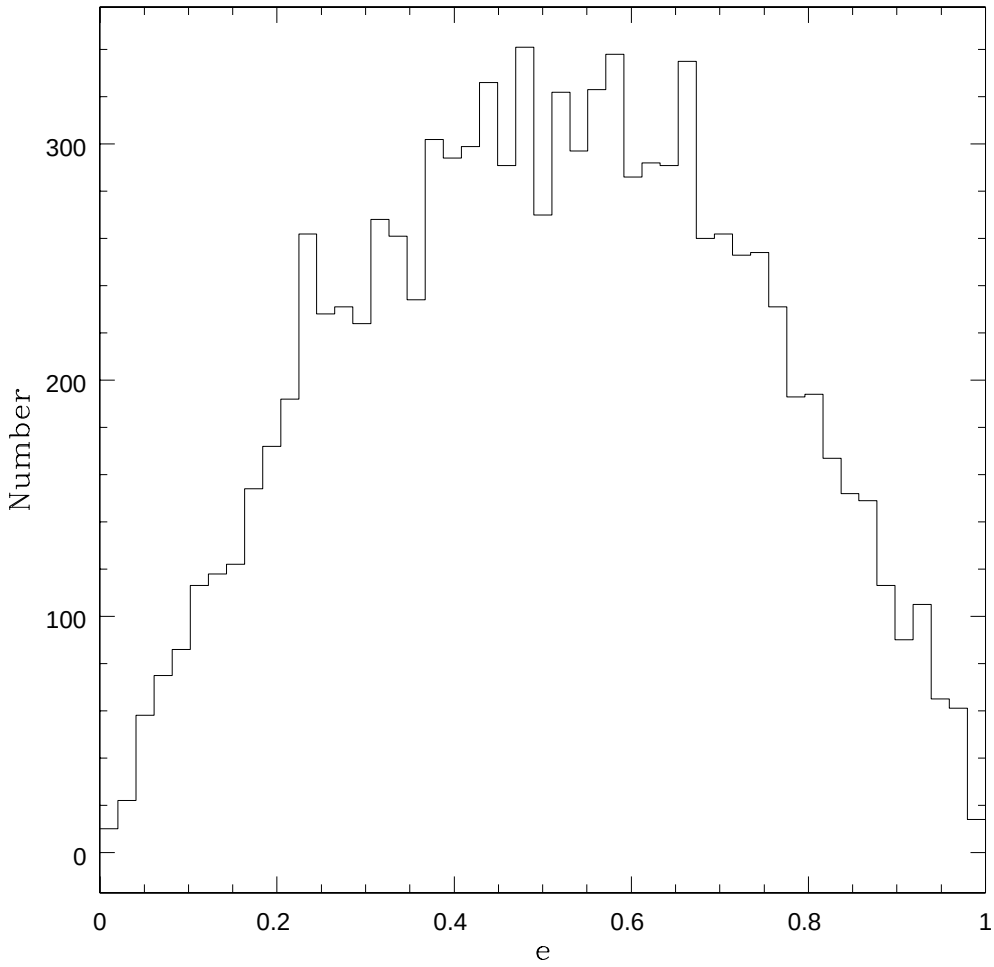

Figure 4.13: Eccentricity distribution of the simulated globular cluster population.

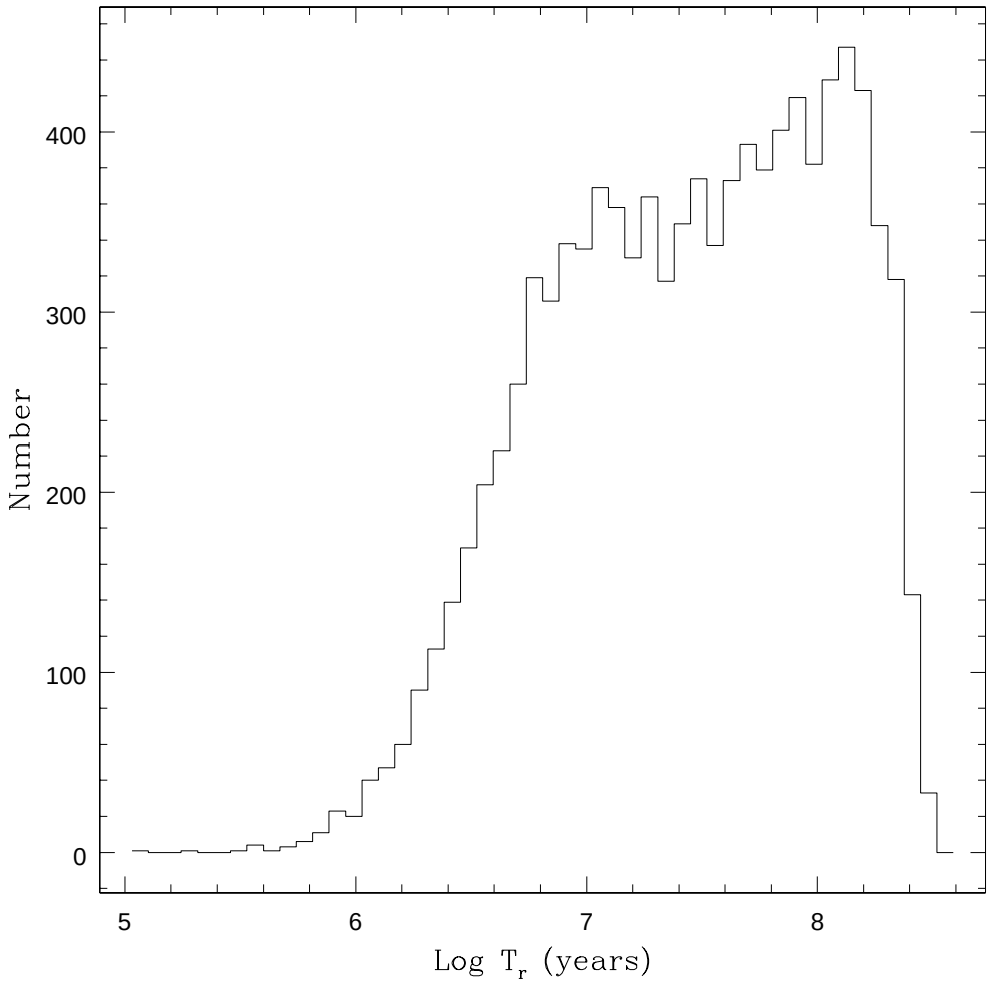

Figure 4.14: Radial period distribution of the simulated globular cluster population.

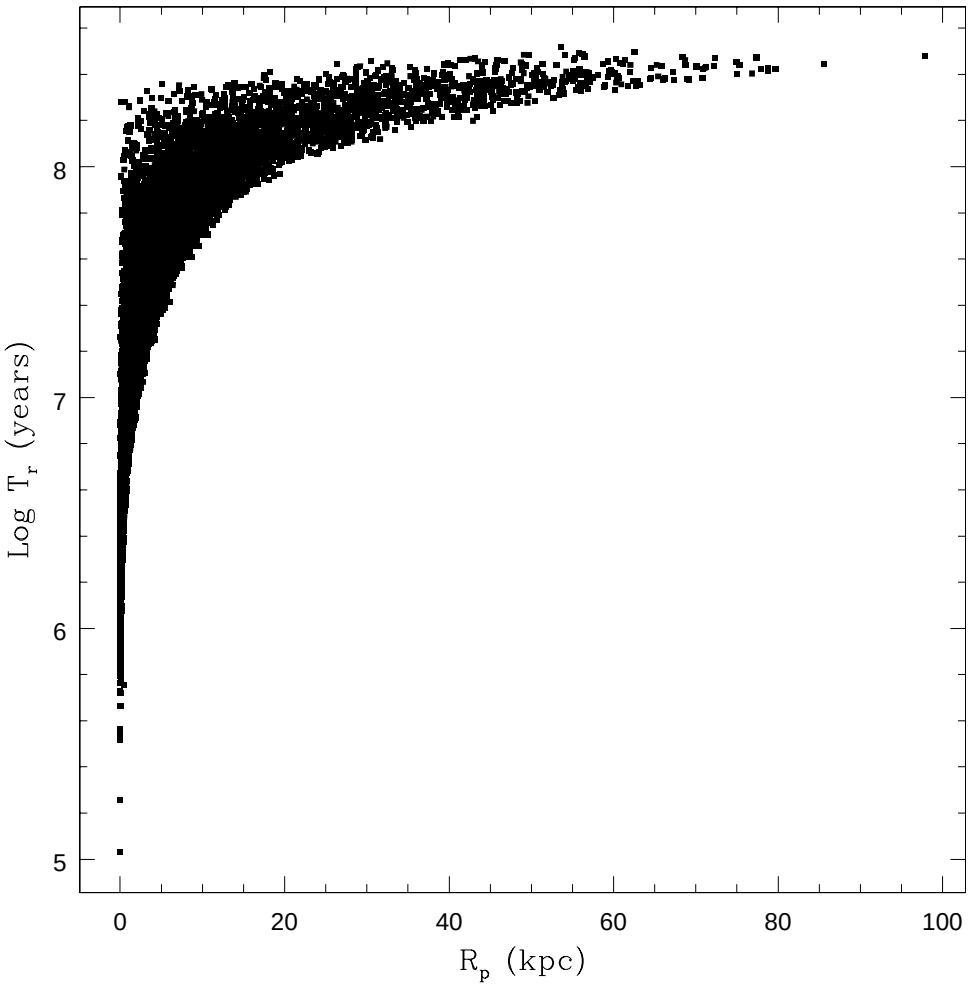

Figure 4.15: Radial period versus perigalactic distance of the simulated globular cluster population.

υ). For a globular cluster located within M87, its tidal radius as a function of its perigalactic distance (r) and mass (M) is then:

$$r_t = (\frac{GM}{\Omega^2 \upsilon})^{1/3} \tag{4.23}$$

Where Ω, κ and υ are now specifically defined as:

$$\begin{aligned}\Omega^2 =& \frac{G\ M_\odot}{(r\ k)^3} \\ & \times [8.10 \times 10^{11}\ [\frac{r/5.1kpc}{1 + r/5.1kpc}]^{1.67} \\ & + 7.06 \times 10^{14}\ [\ln(1 + r/560kpc) \\ & - \frac{(r/560kpc)}{(1 + r/560kpc)}]]\end{aligned} \tag{4.24}$$

$$\begin{aligned}\kappa^2 =& 3\Omega^2 - \frac{2\ G\ M_\odot}{(r\ k)^3} \\ & \times [8.10 \times 10^{11}\ [\frac{\frac{r}{5.1kpc}}{1 + \frac{r}{5.1kpc}}]^{1.67} \\ & + 7.06 \times 10^{14}\ [\ln(1 + \frac{r}{560kpc}) - \frac{\frac{r}{560kpc}}{1 + \frac{r}{560kpc}}]] \\ & + \frac{G\ M_\odot}{(r\ k^2)^2}\ [8.10^{11} \times 1.67 \times (\frac{\frac{r}{5.1kpc}}{1.0 + \frac{r}{5.1kpc}})^{0.67} \\ & \times [\frac{1}{5.1\ (1 + \frac{r}{5.1kpc})} - \frac{r}{5.1^2\ (1 + \frac{r}{5.1kpc})^2}] \\ & + 7.06 \times 10^{14}\ \frac{r}{560\ (1 + \frac{r}{560})^2}]\end{aligned} \tag{4.25}$$

$$\upsilon = 4 - \kappa^2/\Omega^2 \tag{4.26}$$

where $k = 3.08 \times 10^{19} \frac{m}{kpc}$, r is in kiloparsecs, and M is in kilograms.

For arbitrary globular clusters of mass 2×10^4 $M_\odot$, 2×10^5 $M_\odot$, and 2×10^6 $M_\odot$, Figure 4.16 illustrates how the tidal radius of the globular cluster depends on its perigalactic distance. Figure 4.16 indicates that for a given globular cluster mass, tidal radius increases with perigalactic distance. This is in agreement with the derivations of cluster tidal radii discussed in Chapter 2. Essentially the tidal field of a galaxy is weaker as you move farther from its center, allowing clusters to reach greater sizes. Additionally, it is obvious that for a given perigalactic distance, globular clusters of higher mass will have larger tidal radii. This is also in agreement with derivations from Chapter 2, which predict $r_t \ \alpha \ M^{1/3}$ for a set distance.

Equation 4.23 is then applied to each member of the simulated globular cluster population, with each cluster's perigalactic distance calculated as described in Section 4.3. The results are illustrated in plots of Tidal Radius vs. Perigalactic Distance and Tidal Radius vs. Current Distance (Figure 4.17).

The general trend observed in Figure 4.17 is that the tidal radius of globular clusters increases with distance. This is especially apparent in the upper panel of Figure 4.17, where clusters with larger perigalactic distances tend have larger tidal radii. The spread in tidal radius at a given perigalactic distance is the result of having globular clusters of different masses. This is best illustrated in the upper panel of Figure 4.18, where the y-axis in Figure 4.17 has been normalized by cluster mass to the power of 1/3. From Equation 4.23 we see that tidal radius depends on cluster mass to the power of 1/3, but has a much more complex relationship with perigalactic distance as it involves the single and double derivatives of the galactic potential. By dividing each cluster's

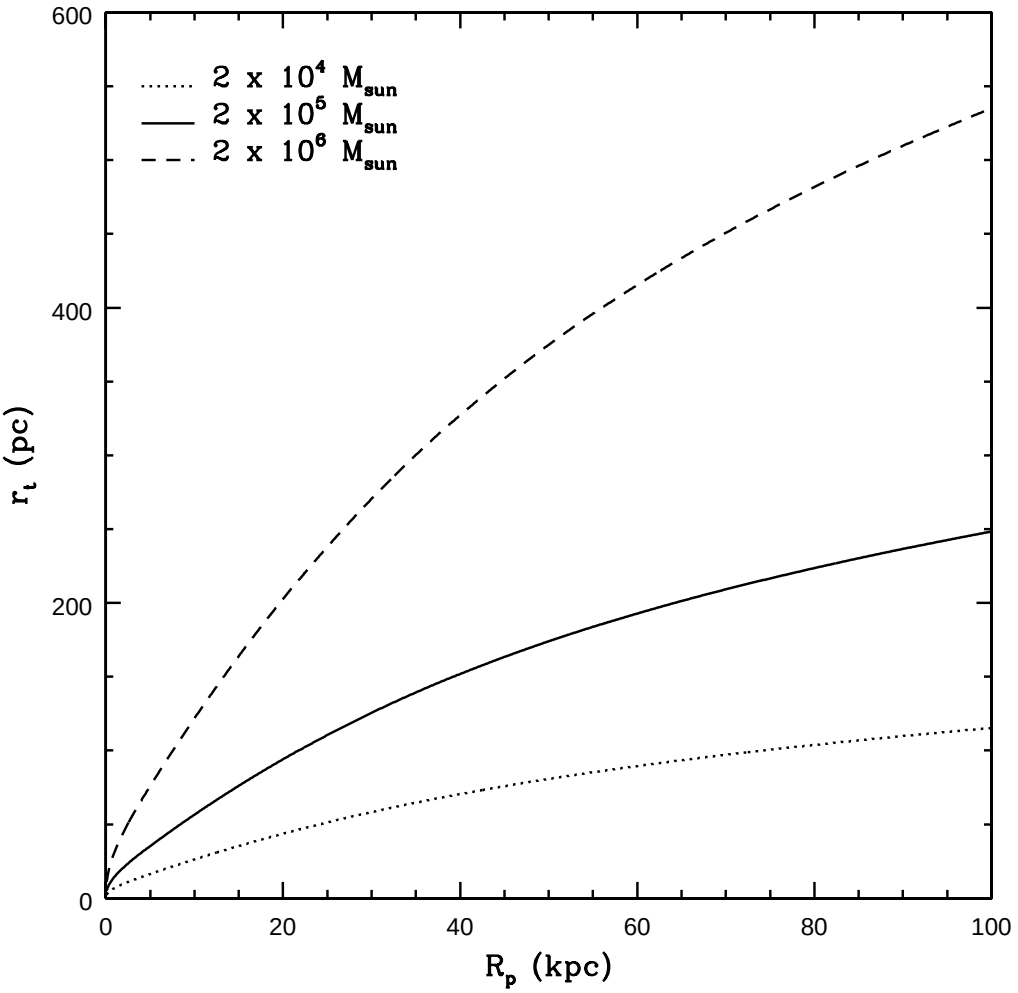

Figure 4.16: Relationship between tidal radius and galactocentric distance for globular clusters of mass 2×10^4 $M_\odot$, 2×10^5 $M_\odot$, and 2×10^6 $M_\odot$within M87.

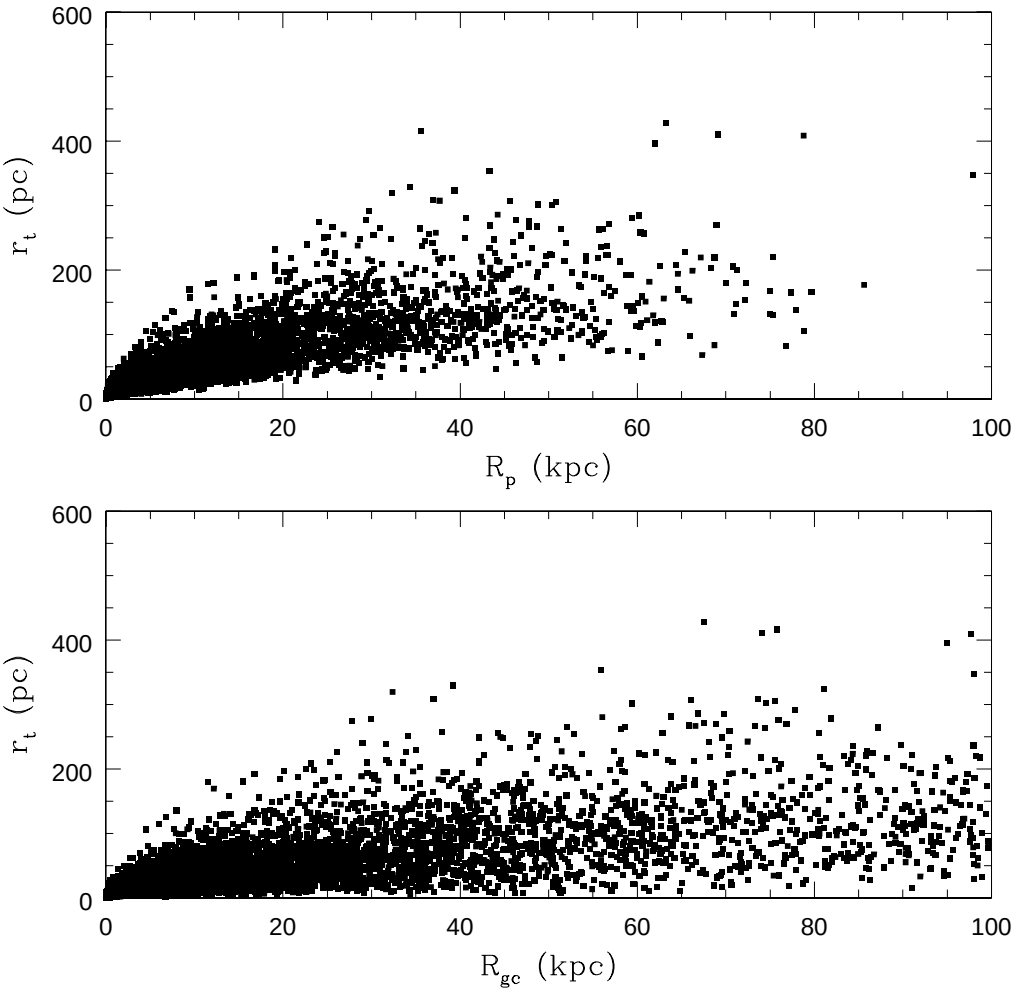

Figure 4.17: Tidal radius of each globular cluster vs. its perigalactic distance (upper) and current galactocentric distance (lower).

tidal radius by its mass to the power of 1/3, we have essentially eliminated the spread due to cluster masses. This is why the upper panel of Figure 4.18 appears to be a smooth line. The scatter in the lower panel of Figure 4.18 is then due to the difference between a cluster's perigalactic distance and current distance. Comparing the upper and lower panels of Figure 4.18, we see that they behave as expected. Since a cluster's current galactocentric distance will always be equal to or larger than its perigalactic distance, all data points in upper panel will be shifted away from the origin to larger distances by varying amounts.

Unfortunately it is not possible to observe real globular clusters at their three-dimensional distance from the galactic center. The three dimensional globular cluster population of M87 is projected onto the two dimensional plane of the sky when observations are made. It is therefore useful to observe the relationship between simulated tidal radius and projected two dimensional galactocentric distance. Observationally a globular cluster's tidal radius will not change, but it may be observed at a distance equal to or less then its true distance from the center of the galaxy. Assuming the $x-y$ plane of the galaxy is parallel with the plane of the sky, projected distance is taken to be $\sqrt{x^2+y^2}$. Since M87 is spherically symmetric, any two-dimensional plane can be taken to be the plane of the sky without influencing the results. The upper plot in Figure 4.19 demonstrates the relationship between tidal radius and projected galactocentric distance for the same simulated globular cluster population in Figure 4.17. Normalizing the tidal radius by cluster mass, we can compare the lower plot in Figure 4.19 to Figure 4.18 and see how going from a cluster's perigalactic distance, to current distance, to projected current

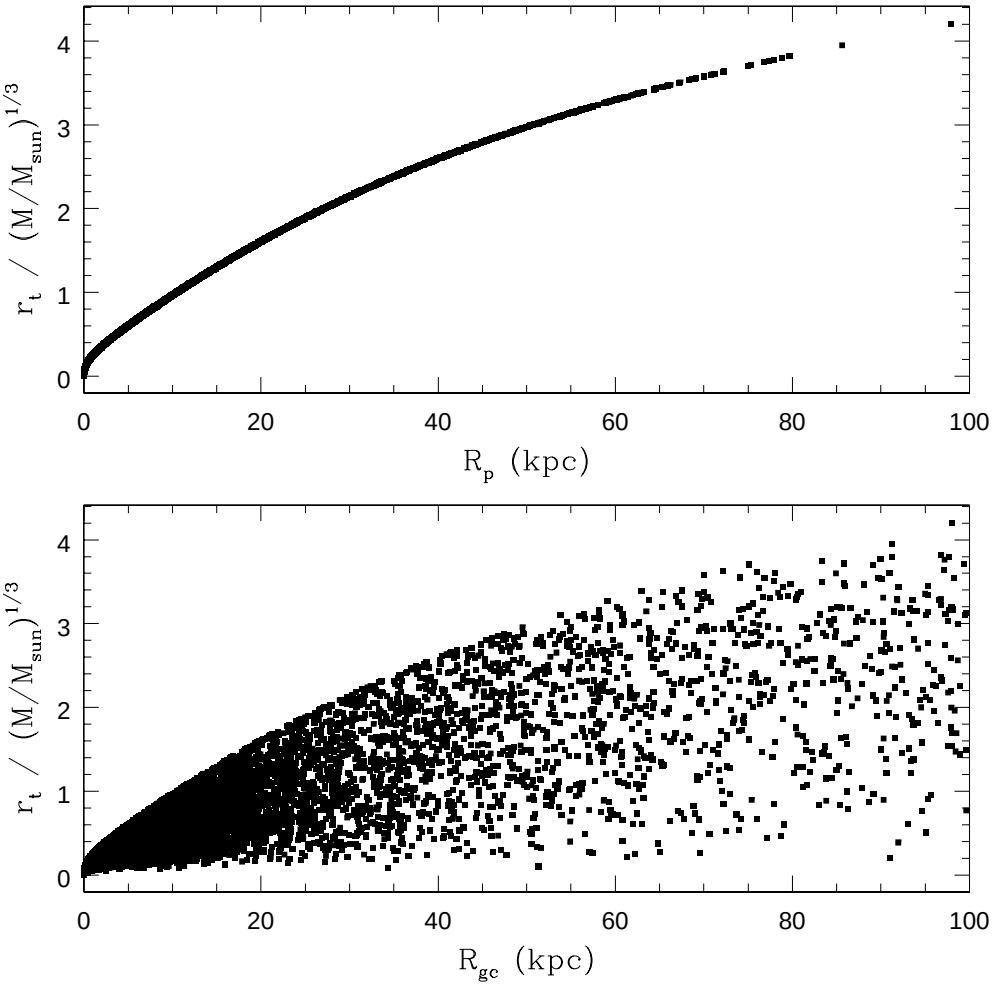

Figure 4.18: The ratio of cluster tidal radius to $(M/M_{\odot})^{\frac{1}{3}}$ vs. its perigalactic distance (upper) and current galactocentric distance (lower).

distance increases the amount of scatter about the curve in the upper plot of Figure 4.18.

When comparing the lower panels of Figure 4.17 and Figure 4.19, it is clear that many of the globular clusters will have an observed two-dimensional distance smaller than their true distance. A globular cluster in Figure 4.17 will be located in the same horizontal position in Figure 4.19 only if its orbital plane is parallel with the plane of the sky. In terms of Cartesian coordinates, if we assume the plane of the sky and the $x - y$ plane of the simulated galaxy are parallel, globular clusters with a z coordinate of zero are not subject to projection effects. On the other hand, any globular cluster with a z coordinate not equal to zero will be observed at a smaller galactocentric distance. Figure 4.19 confirms this as the majority of data points are shifted horizontally towards the origin. However, since projection has no effect on the tidal radius of a globular cluster, a data point's vertical position in Figures 4.17 and 4.19 remains unchanged.

This point is extremely relevant to observations. When the tidal radius of an observed globular cluster is measured, the observationally and theoretically determined tidal radii will not agree if we assume its current distance is its perigalactic distance. Since the perigalactic distance of an extragalactic globular cluster cannot be determined, the theoretical tidal radius can only be calculated with the cluster's present projected distance. In the case where the projected distance is greater than the perigalactic distance, an overestimation of the actual tidal radius will occur. Hence it is expected that observationally determined tidal radii will be less than or equal to its theoretically determined

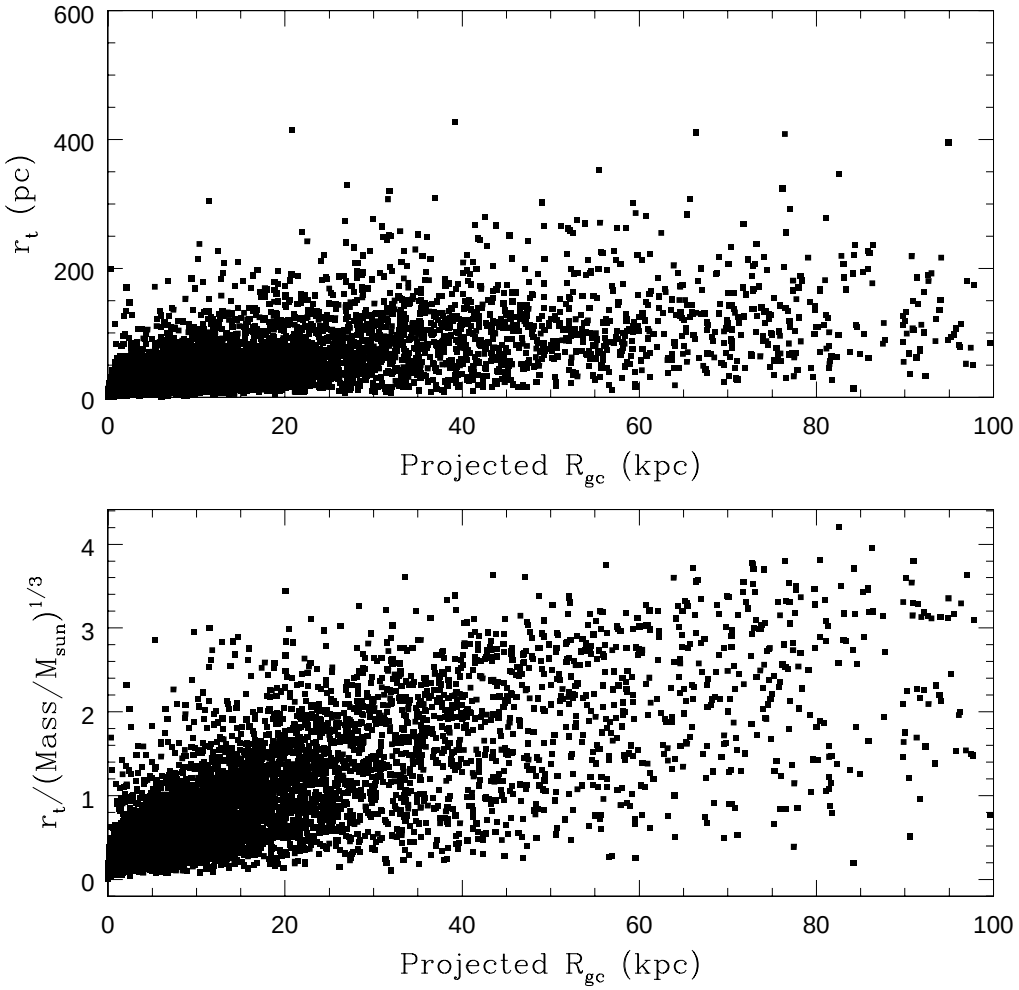

Figure 4.19: Cluster tidal radius (upper) and the ratio of cluster tidal radius to $(M/M_{\odot})^{\frac{1}{3}}$ (lower) vs. its projected distance.

counterpart. In the case where the cluster's projected distance is smaller than its perigalactic distance, the theoretical tidal radius will be underestimated. However, instead of theoretically determining tidal radii of observed projected globular clusters, the simulated distribution makes it possible to compare observationally determined tidal radii in M87 to simulated tidal radii. This will act as a test to determine if observationally determined King tidal radii are equivalent to the theoretical Jacobi radius of a cluster, as was assumed in Chapter 2.

To better compare with observations, tidal radii are converted to effective radii. Since we will be comparing our simulation to observed clusters fit with K62 profiles, we convert theoretical tidal radii to effective radii assuming each cluster can be represented by a K62 profile. Assuming all stars within the cluster are identical and the cluster is spherically symmetric, Equation 2.32 can be integrated with respect to $2\pi r dr$ to determine the total number of stars within a radius r. For $x = (r/r_c)^2$ and $x_t = (r_t/r_c)^2$, the number of stars within a radius r is given by Equation 4.27. The total number of stars within a cluster is given as $n(x_t)$ (Equation 4.28).

$$n(x) = \pi r_c^2 k(\ln(1+x) - 4\frac{(1+x)^{\frac{1}{2}} - 1}{(1+x_t)^{\frac{1}{2}}} + \frac{x}{1+x_t}) \tag{4.27}$$

$$n(x_t) = \pi r_c^2 k(\ln(1+x_t) - \frac{(3(1+x_t)^{\frac{1}{2}} - 1) * ((1+x_t)^{\frac{1}{2}} - 1)}{1+x_t}) \tag{4.28}$$

The effective radius is then the radius at which the ratio $n(x)/n(xt)$ is 1/2. Using this conversion method, we can plot the ratio of r_h/r_t versus

central concentration and compare the results to the K62 portion of Figure 3.25. This comparison is made in Figure 4.20. The perfect agreement between the simulated clusters (solid line) and observed clusters (points) illustrate that our conversion method is appropriate for any cluster which can be represented by K62 model. The results of this conversion versus projected cluster distance is illustrated in Figure 4.21, with the median cluster effective radius shown in red. The median effective radius at a given distance was found by dividing clusters into bins based on their projected galactocentric distance. Each bin was 0.03 kpc in width.

4.5 Analysis of Individual Simulated Globular Clusters

4.5.1 In-spiral Time Due to Dynamical Friction

Before we compare the simulated population to observations, we must first consider which simulated clusters are expected to survive to present day. More specifically, clusters with small orbits and clusters with highly elliptical orbits such that their perigalactic distance is very small may have been torn apart by dynamical friction, the force exerted on a cluster due to the tidal field of the galaxy which will decrease the cluster's tangential velocity, causing its orbit to decay (Chandrasekhar, 1943). Over time, the cluster's orbit can decay until the cluster reaches the center of the galaxy, and the stars can no longer remain bound. It must be determined which of the simulated globular clusters should

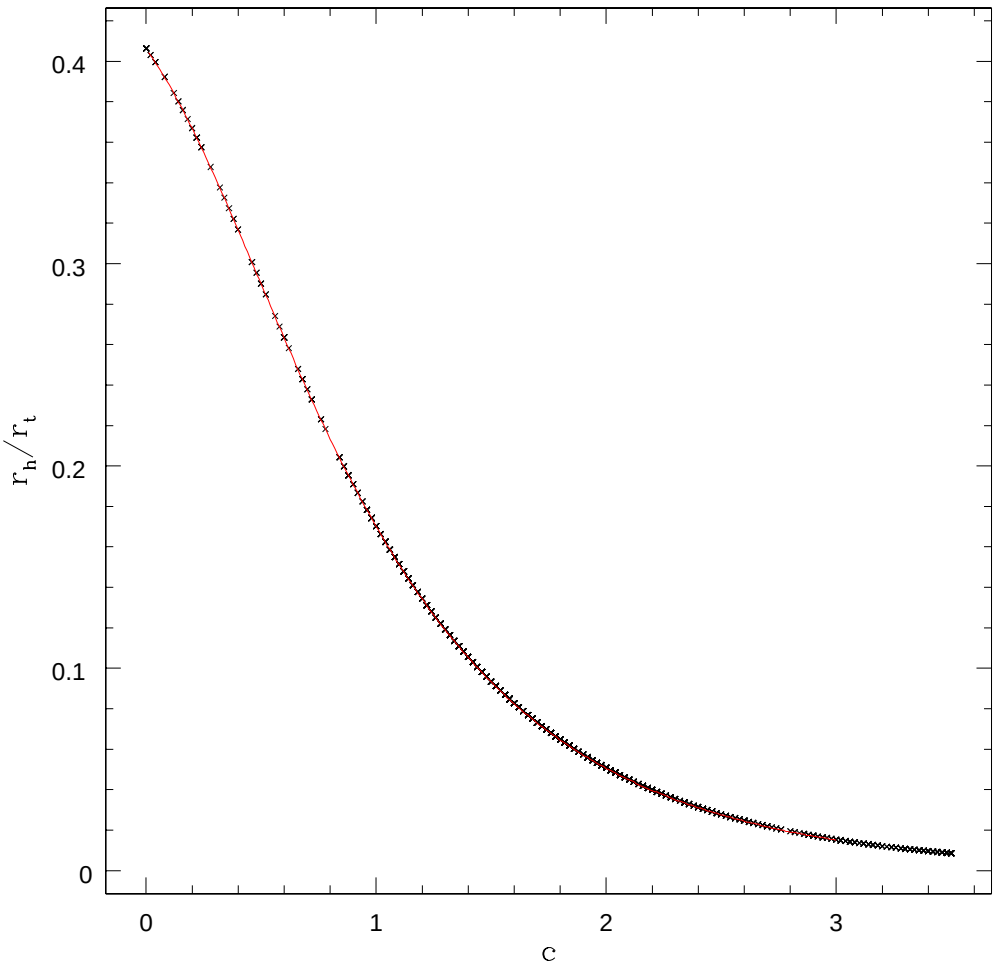

Figure 4.20: Ratio of effective radius to tidal radius vs. central concentration for observed clusters fit with K62 models (black points) and theoretical clusters with tidal radii converted to effective radii via K62 models (red line).

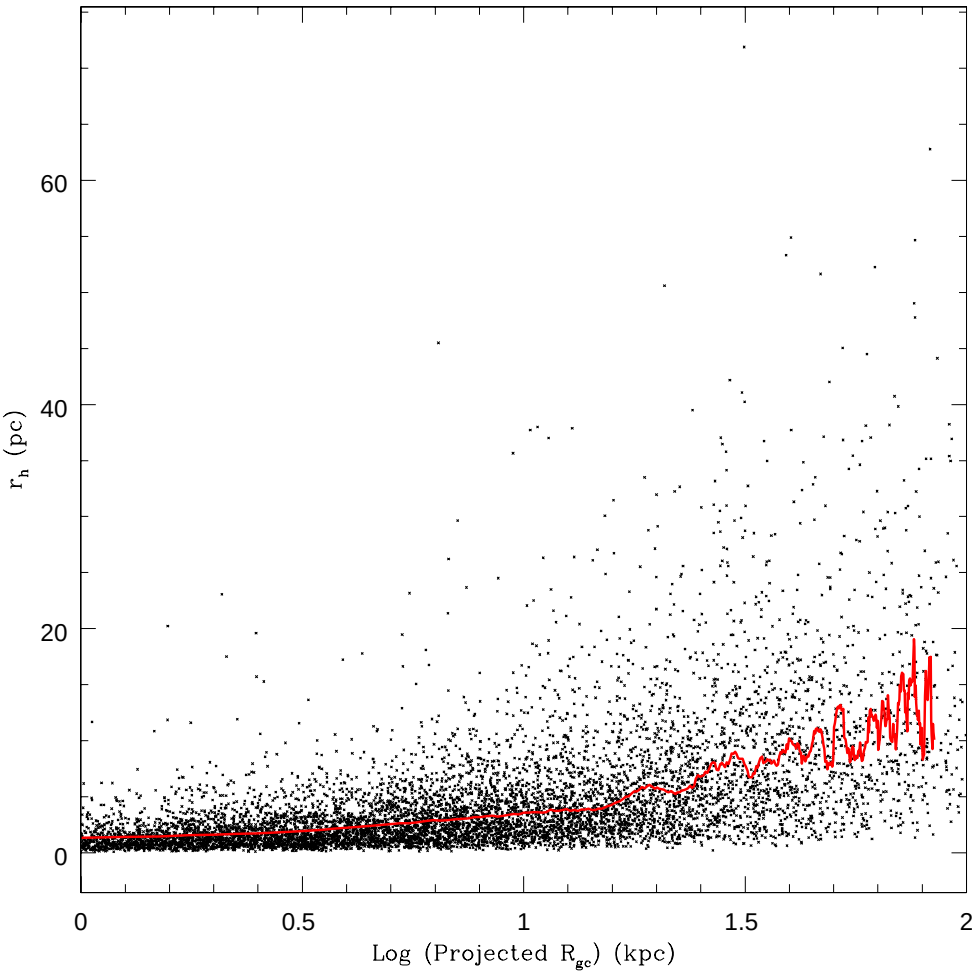

Figure 4.21: Effective radius of each globular cluster compared with its projected distance. The red line illustrates the median effective radius.

be removed from the dataset. The following derivation of in-spiral time is taken from Binney & Tremaine (2008).

We can begin with Chandrasekhar's dynamical friction formula (Equation 4.29), which determines the rate of change in the velocity ($\frac{dv_M}{dt}$) of a mass M, orbiting in a field of stars of mass m_a with a distribution $f(\vec{x}, \vec{m}_a)$ (Chandrasekhar, 1943).

$$\frac{d\vec{v}_M}{dt} = -16\pi^2 G^2 M m_a \ln\Lambda [\int_0^{v_M} v_a^2 f(v_a)\, dv_a] \frac{\vec{v}_M}{v_M^3} \tag{4.29}$$

where the Coulomb logarithm ($\ln\Lambda$) is defined as

$$\ln\Lambda = \ln(\frac{b_{max}}{max(r_h, \frac{GM}{v_{typ}^2})}) \tag{4.30}$$

where r_h is the half-mass radius of the subject system, v_{typ} is the typical relative velocity at a distance $\mathbf{R}$ ($v_{typ} = \frac{G\mathbf{M}}{\mathbf{R}}$), $\mathbf{M}$ and $\mathbf{R}$ are the mass and radius of the host galaxy, and b_{max} is the maximum impact parameter. The maximum impact parameter can be assumed to be the orbiting radius R of the mass M. However, it is important to note that this assumption is a local approximation, and does not take into account very close or very distant encounters (Binney & Tremaine, 2008).

It is then assumed that the distribution function $f(\vec{v}_a)$ is Maxwellian with dispersion σ, and Equation 4.29 can be rewritten as

$$\frac{d\vec{v}_M}{dt} = -\frac{4\pi G^2 M n m \ln\Lambda}{v_M^3} [erfX - \frac{2X}{\sqrt{\pi}} e^{-X^2}] \vec{v}_M \tag{4.31}$$

where n is the total number of field stars, $X = \frac{\vec{v}_M}{\sqrt{2}\sigma}$, and erf is the error function.

Taking nm to be the overall background density ρ, we assume the density distribution of the host galaxy is that of an isothermal sphere ($\rho(r) = \frac{v_c^2}{4\pi G r^2}$) where $v_c = \sqrt{2}\sigma$ is the constant circular speed at r. As summarized in Churazov et al. (2010), this is an acceptable assumption for an elliptical galaxy like M87. The frictional force $F = M|\frac{d\vec{v}_M}{dt}|$ on the orbiting mass M is then

$$\begin{aligned} F &= -\frac{4\pi G^2 M^2 \rho(r) \ln\Lambda}{v_c^2}[erf(X) - \frac{2X}{\sqrt{\pi}}e^{-X^2}]\vec{v}_M \\ &= 0.428 \ln\Lambda \frac{GM^2}{r^2} \end{aligned} \tag{4.32}$$

and $X = \frac{v_c}{\sqrt{2}\sigma} = 1$.

This force is tangential and in the opposite direction to the velocity of the orbiting mass M. This results in the mass M losing angular momentum L at a rate of

$$\frac{dL}{dt} = -Fr \approx -0.428 \ln\Lambda \frac{GM^2}{r} \tag{4.33}$$

Thus the orbiting mass M, which was initially assumed to have a circular orbit, will continue to spiral towards the center of the host galaxy while remaining in an almost circular orbit. Since the circular-speed curve of the singular isothermal sphere is flat, the orbiting mass will continue to orbit at speed v_c at a radius r with angular momentum $L = Mrv_c$ as it spirals inward. Substituting $\frac{dL}{dt} = Mv_c\frac{dr}{dt}$ into Equation 4.33, we obtain

$$\begin{aligned} r\frac{dr}{dt} &= -0.428 \ln \Lambda \frac{GM}{v_c} \\ &= -0.302 \ln \Lambda \frac{GM}{\sigma} \end{aligned} \tag{4.34}$$

Returning to the fact that the host galaxy of mass **M** is assumed to be an isothermal sphere, its velocity dispersion at a distance r is then

$$\sigma_{\mathbf{M}} = \sqrt{\frac{G\ \mathbf{M}(r)}{2\ r}} \tag{4.35}$$

Assuming that the orbiting mass M is a globular cluster, which is also isothermal, the mass of the globular cluster M can be set equal to

$$M = \frac{2\sigma_s^2 r_t}{G} \tag{4.36}$$

where σ_s is the velocity dispersion of the cluster.

Substituting into Equation 4.34, we get the rate of orbital decay for the globular cluster to be

$$\frac{dr}{dt} = -0.428 \ln \Lambda \frac{\sigma_s^3}{\sigma_M^2} \tag{4.37}$$

Assuming there is no variation in $\ln \Lambda$ with radius, the in-spiral time from a radius r_i is found to be

$$T_{df} = \frac{2.7Gyr}{\ln \Lambda}\ \frac{r_i}{30kpc}\ (\frac{\sigma_m}{200\ km/s})^2\ (\frac{100\ km/s}{\sigma_s})^3 \tag{4.38}$$

It is important to note that Equation 4.38 assumes the clusters have a circular orbit. In calculating each cluster's in-spiral time, we will incorrectly assume each cluster has a circular orbit at its perigalactic distance. This results in an underestimation of a cluster's in-spiral time for more elliptical orbits, as the cluster spends little time near perigalacticon. In essence we are calculating a lower limit for each cluster's in-spiral time. Additionally, we have assumed that the host galaxy and globular cluster are both isothermal spheres, and that the distribution function of field stars in the galaxy is Maxwellian. These assumptions will be justified later.

We calculate the in-spiral time due to dynamical friction of each simulated cluster with Equation 4.38 and the cluster's perigalactic distance. Figure 4.22 illustrates the resulting distribution. While the distribution appears to be relatively symmetric about a mean in-spiral time of approximately 10^{14} years, there is a small percentage of clusters with very small in-spiral times less than 10 Gyr, which is an approximation of the age of M87.

If we consider the relationship between a cluster's in-spiral time and its perigalactic distance (Figure 4.23), we see that clusters with in-spiral times less than 10 Gyr all have very small perigalactic distances. This is as expected, as we observe in Equation 4.38 that $T_{df} \; \alpha \; r$. Other clusters with small perigalactic distances but higher in-spiral times will be of lower mass and/or large tidal radii such that their velocity dispersions (σ_{gc}) are small ($T_{df} \; \propto (1/\sigma_{gc})^{1/3}$).

When we compare each cluster's in-spiral time to its radial period (Figure 4.24), globular clusters with in-spiral times less then 10 Gyr have a range of radial periods between $10^{6.5}$ and $10^{8.5}$ years. While the clusters with smaller

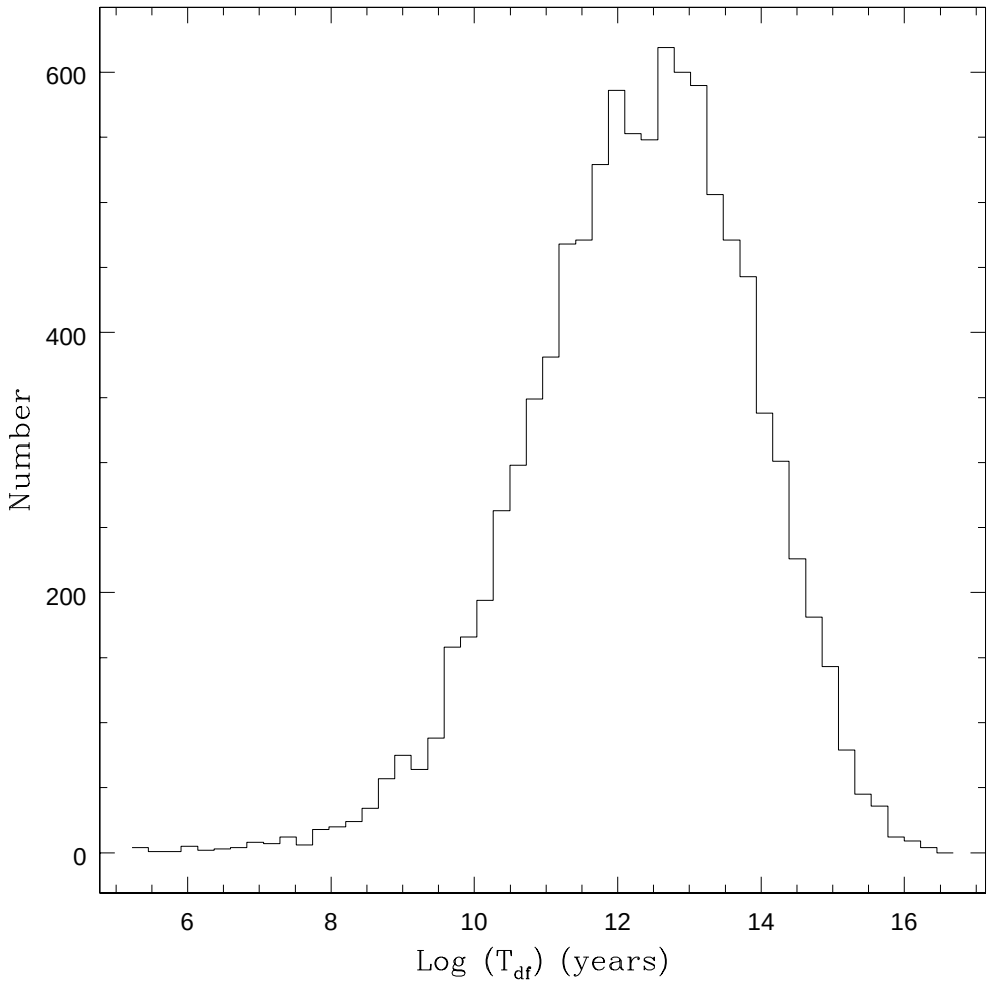

Figure 4.22: Distribution of in-spiral times due to dynamical friction.

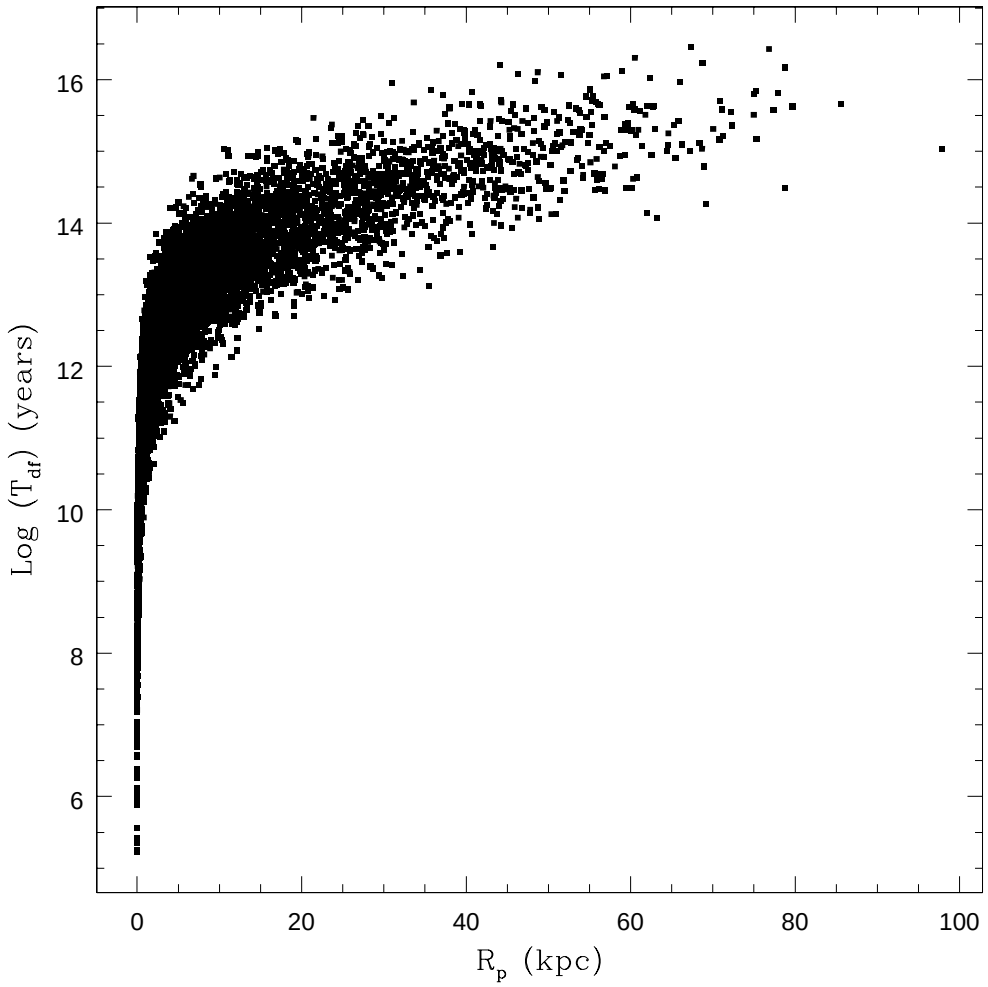

Figure 4.23: Simulated globular cluster's in-spiral time due to dynamical friction as a function of its perigalactic distance.

radial periods will have mean distances near their perigalactic distance, clusters with larger radial periods will have highly elliptical orbits, and spend little time near perigalacticon. It will be these large period clusters whose calculated in-spiral time will be a notable underestimation. However, since the total amount of clusters with calculated in-spiral times less than 10 Gyr is a mere 0.78% of the entire population, eliminating a few clusters which may actually have acceptable orbits will not alter the findings of this simulation. Hence the previously mentioned assumptions required to make this calculation are acceptable. The 78 globular clusters with in-spiral times less than the approximate age of M87 (10 Gyr) were eliminated from the simulation.

4.5.2 Relaxation Time

By assuming that a cluster's tidal radius is imposed at perigalacticon, we have indirectly made a second assumption that each cluster does not change in size over the course of its orbit, before it returns to perigalacticon. A more precise way of making this statement is that we have assumed the radial period of each cluster is less than its relaxation time, such that it returns to perigalacticon before it is able to relax. A star orbiting within a globular cluster will be subject to multiple two-body interactions between itself and every other star in the cluster. This results in each star in the cluster modifying each other's velocity such that each star has a final orbit which is much different than if it had been orbiting in a smooth gravitational field. The time it takes for the cluster to undergo all these two-body encounters in order to significantly change stellar velocities is known as the relaxation time (Binney & Tremaine,

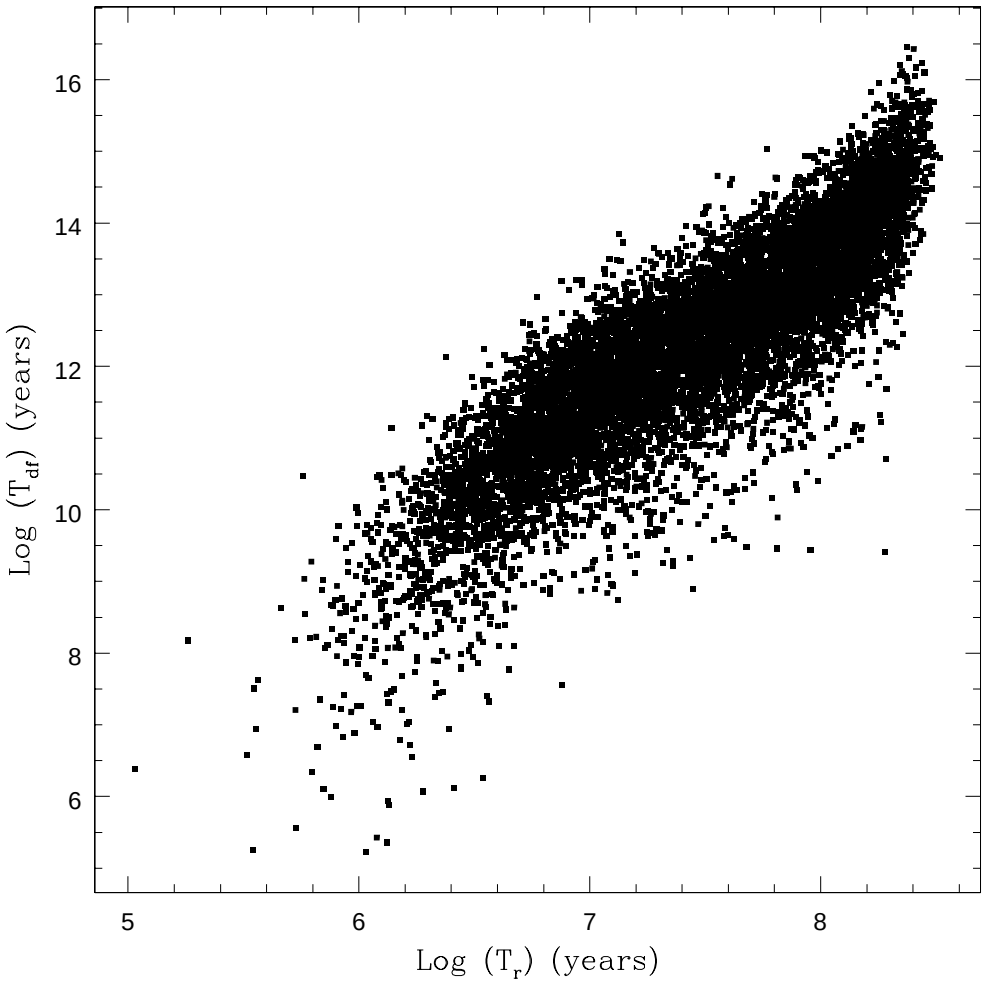

Figure 4.24: Simulated globular cluster's in-spiral time due to dynamical friction vs. radial period.

2008). If a cluster's radial period is longer then its relaxation time, then it is entirely possible that as the cluster relaxes, it may push stellar orbits beyond the theoretical tidal limit imposed by its perigalactic distance. This results in the cluster's observational tidal radius being much larger than theory suggests. Therefore we must test each simulated cluster to ensure that this is not the case.

For each simulated cluster, we calculate the half-mass relaxation time, which is the time it takes for the stars within a radius that contains half of the cluster's mass to relax. The relation is shown as Equation 4.39, taken from Meylan et al. (2001).

$$t_{rh} = (8.92 \times 10^5) \frac{(M/M_\odot)^{\frac{1}{2}}}{(\bar{m}/M_\odot)} \frac{(r_h/1pc)^{\frac{3}{2}}}{log(0.4M/\bar{m})} \tag{4.39}$$

where $\bar{m}$ is the mean stellar mass of all the stars in the cluster (taken to be 0.5 $M_\odot$), M is the total mass of the cluster, and r_h is the half-mass radius. Figure 4.25 illustrates the half-mass relaxation time and radial period of each simulated globular cluster. Only clusters below the dashed line have relaxation times that are less than their radial period, such that they could potentially grow larger than their perigalacticon induced tidal radius. These clusters only constitute approximately 1% of the simulated cluster population. Additionally, these clusters have relaxation times that are only marginally less than their radial period, which suggests the cluster's ability to grow to sizes greater than its perigalacticon induced tidal radius is minimal.

We also calculated the core relaxation time of each cluster as given by Djorgovski (1993). We found that while approximately 25% of the simulated

clusters have core relaxation times less than their orbital period (Figure 4.26), these clusters cover the full range of masses and concentrations in our cluster sample. Hence their inclusion will not bias our results in any way. We conclude that based on the assumptions and calculations above, using a cluster's perigalactic distance to calculate tidal radii is acceptable, and that a cluster will undergo minimal changes in size before it returns to perigalacticon.

4.6 Effects of Orbital Anisotropy

Up to this point, we have been operating under the assumption that the velocity distribution of M87 is isotropic. That is the radial, θ, and ϕ velocity distributions are all equal to the observed velocity distribution of M87. In terms of the anisotropy parameter β, this is the $\beta = 0$ case. However, as discussed in Chapter 2 it is not expected that $\beta = 0$ for every galaxy. In fact, it is more likely that the value of β changes for different regions of a galaxy. For M87, Côté et al. (2001) found that while the cluster population of M87 appears to be isotropic as a whole, it is possible that β could change as a function of galactocentric distance. More specifically, the inner regions of M87 could possibly have a negative value for β such that orbits are preferentially tangential, while the outer regions of M87 may contain clusters with more radial orbits ($\beta > 0$). This forces us to consider the effects of changing the value of β in our simulation to observe the effect this has on cluster tidal radii.

The simulation outlined in this chapter was repeated for different values of β. For β greater than zero, the radial velocity dispersion was assumed to be equal to the observed velocity dispersion, and the θ and ϕ distributions were

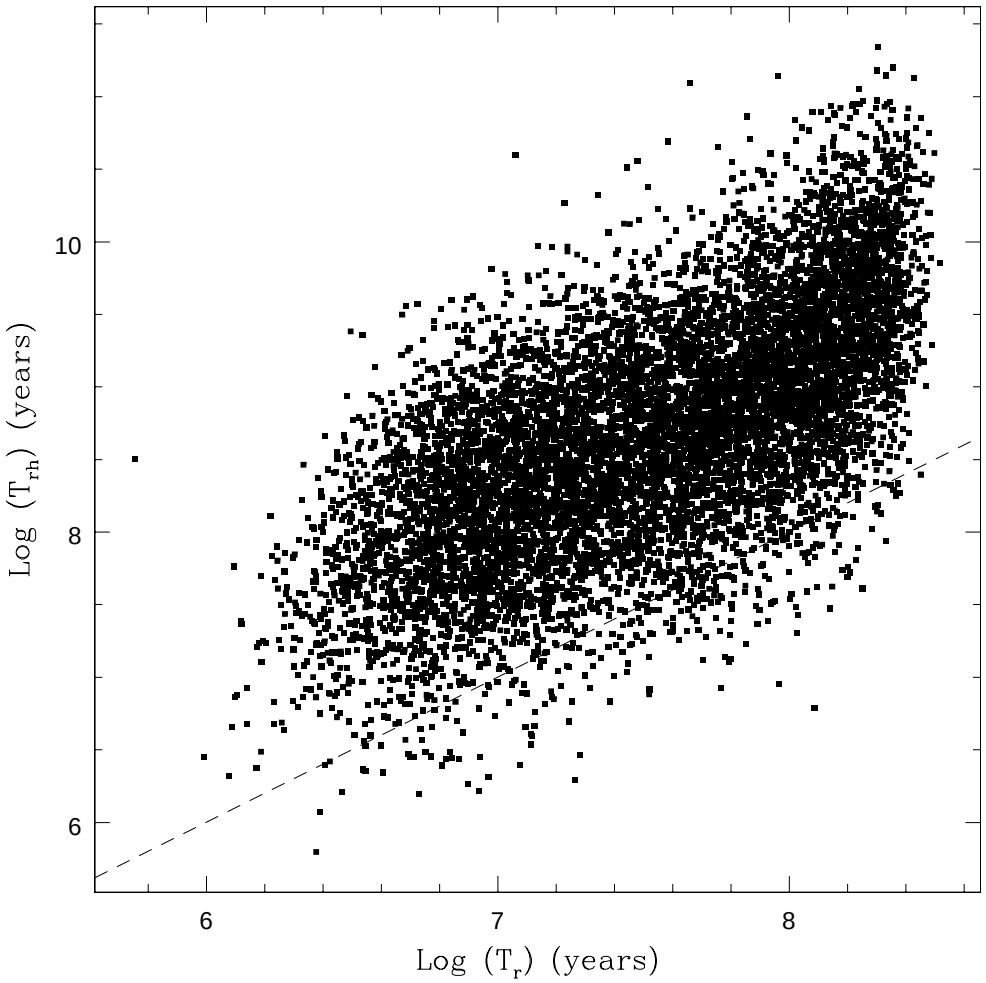

Figure 4.25: Simulated globular cluster's half-mass relaxation vs. radial period. The dashed line represents half-mass relaxation time equalling radial period.

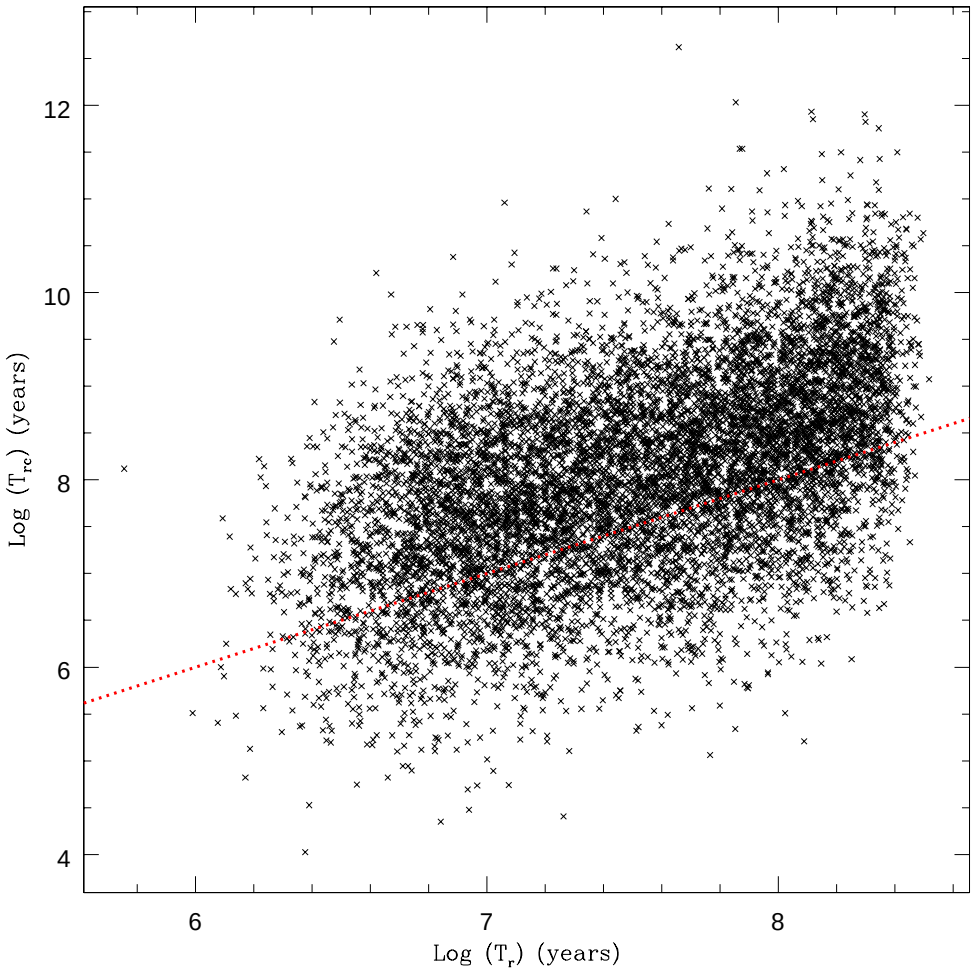

Figure 4.26: Simulated globular cluster's core relaxation vs. radial period. The dashed line represents core relaxation time equalling radial period.

assumed to be equal and calculated via Equation 2.57. This ensures that each cluster's radial velocity will be larger than its tangential velocity, showing a preference towards radial orbits. For β less than zero, the θ and ϕ velocity distributions are assumed to be equal to the observed velocity distribution, with the radial velocity distribution determined via Equation 2.57. This ensures that tangential velocities will be larger than radial velocities, showing a preference towards circular orbits.

To illustrate the influence orbital anisotropy has on cluster sizes, we plot the median effective radius of each simulated population versus projected galactocentric distance. As seen in Figure 4.27, a cluster at a given galactocentric distance has its largest possible size when $\beta = -1$ (magenta). As discussed in Chapter 2, this is because the cluster's orbit will be nearly circular, so it is not brought much deeper into the tidal field of the galaxy then its present galactocentric distance. Also in agreement with Chapter 2, as β increases, orbits become more and more radial, such that clusters are brought deeper and deeper into the tidal field of the galaxy to small perigalactic distances. This in turn minimizes their tidal and effective radii.

We will leave it to Section 4.7 to compare Figure 4.27 with observations, and determine how β should behave as a function of galactocentric distance to best match theoretical tidal radii to observations.

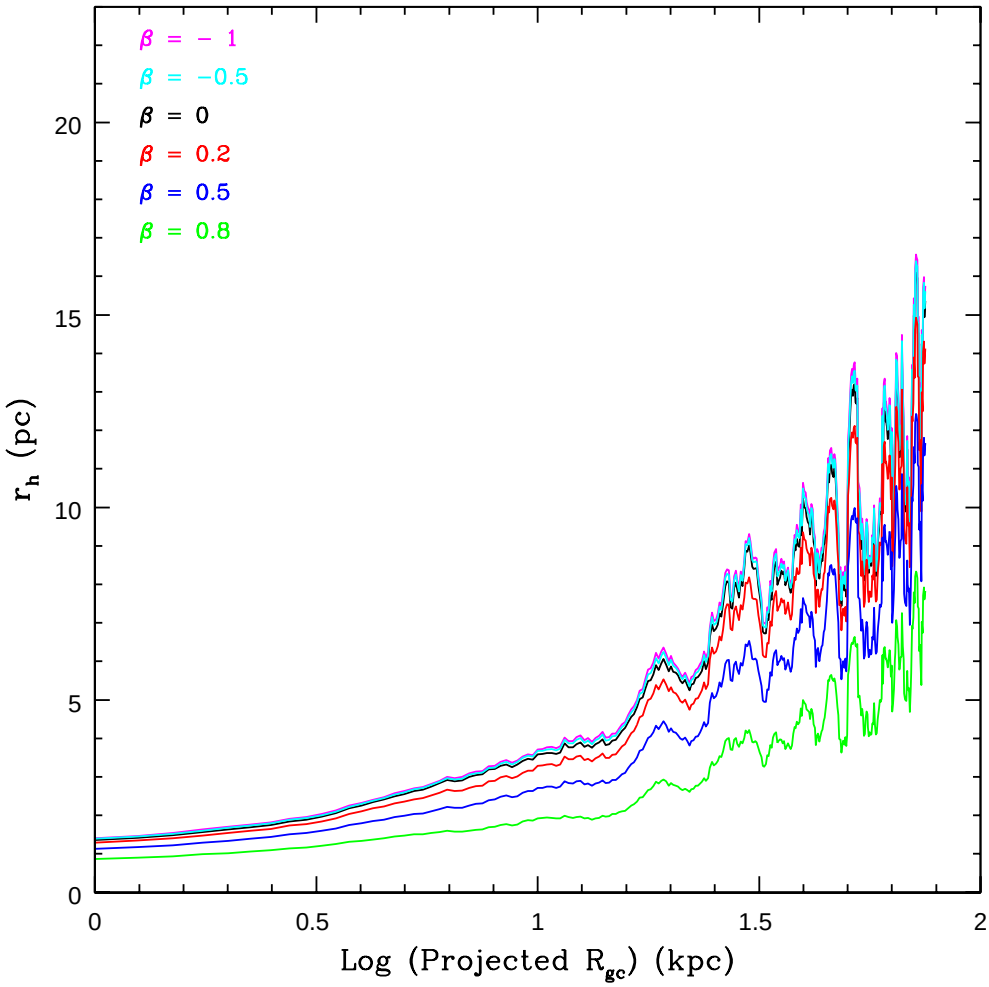

Figure 4.27: Effective radius of each globular cluster compared with its projected distance for different values of β.

4.7 Matching Simulation to Observations

4.7.1 The Isotropic Case

Ultimately, comparisons between K62, K66, W75, and S68 models in Chapter 3 suggested that K62 effective radii better represent the true effective radius of each cluster. Comparisons with the more commonly used K66 models resulted in the identification of a sub-set of clusters with K66 effective radii much smaller then K62 effective radii. Since W75 and S68 effective radii were in agreement with the K62 model, the decision was made to compare only the results from K62 model fitting to theoretical tidal radii.

The first comparison that was made between observations and theory was for the simulated isotropic case, with $\beta = 0$. The median effective radius versus projected galactocentric distance is illustrated in Figure 4.28. The first observation that can be made is that the simulation underestimates effective radii in the inner regions of M87. Second, in the central and outer regions of M87 the simulation appears to be in agreement with the observations, however due to the limited field of view of the observations we cannot make comparisons past approximately 9 kpc. It would be beneficial to have observations of M87 out to larger galactocentric distances, to see if the theoretical and observational tidal radii remain in agreement.

Applying a χ^2 test to the model and observations resulted in $\chi^2 = 30.16$. While this result is clearly not a match, a perfect match was not anticipated. As previously mentioned, Côté et al. (2001) suggested that it is possible that β could be less than zero for the inner regions of M87 and greater than zero

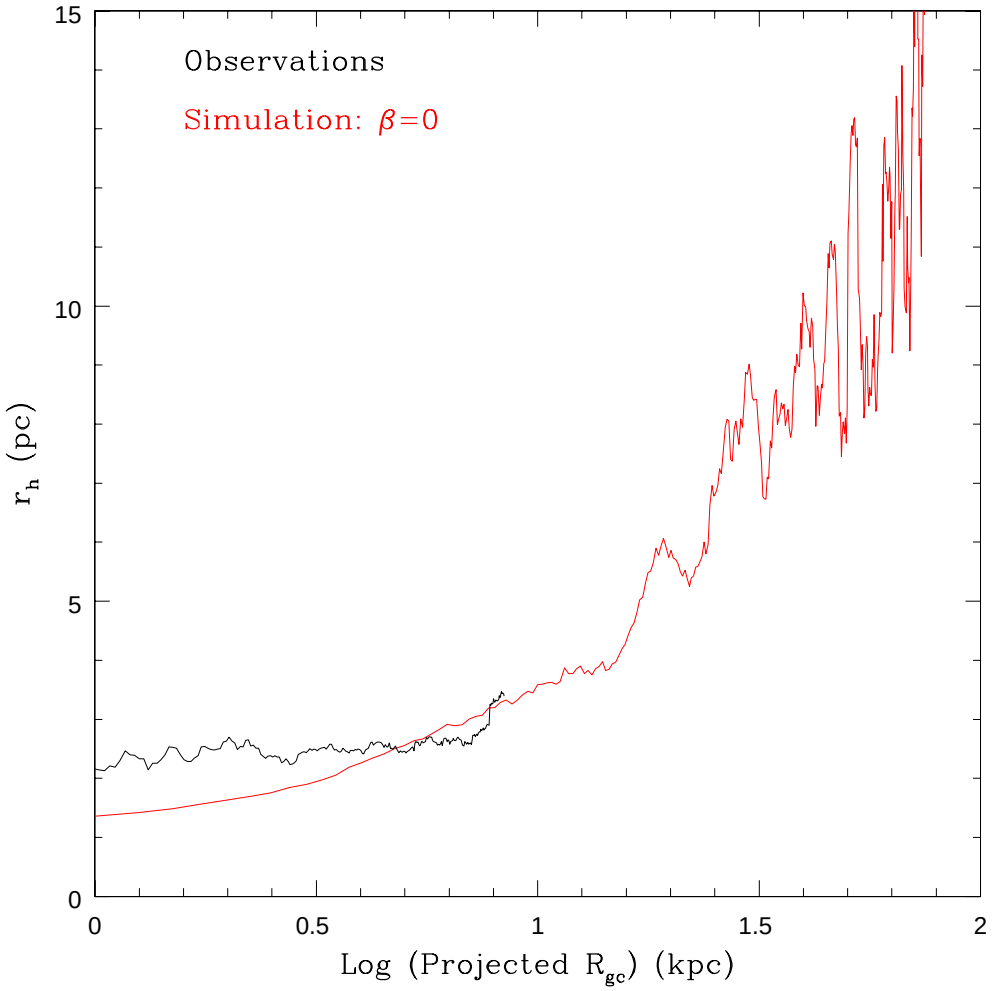

Figure 4.28: Effective radius of each globular cluster compared with its projected distance for observations and the $\beta = 0$ simulation.

in the outer regions. This is not only possible for M87 (Côté et al., 2001), but for other galaxies as well. Using cosmological N-body simulations, Prieto & Gnedin (2008) calculate the orbits of model clusters in the tidal field of the Milky Way and find that orbits are nearly isotropic ($\beta = 0$) for the inner regions and radial ($\beta > 0$) in the outer regions of the galaxy. Theoretical work regarding dark matter halos with NFW profiles (similar to M87) by Zait, Hoffman, & Shlosman (2008) also find that β increases from the isotropic case in the inner regions of a galaxy to more radial orbits in the outer regions. N-body simulations by Ludlow et al. (2010) investigating the radial dependence of the density and velocity dispersion in cold dark matter halos also support these findings. Both Prieto & Gnedin (2008) and Zait, Hoffman, & Shlosman (2008) find evidence for β to be less than zero at small galactocentric distances. Therefore, while the isotropic case was essentially a reasonable first comparison to make between observations and theory, we expect a change in the anisotropy profile of our simulated population is necessary to better match theory to observations. It is encouraging that by taking the gravitational potential of M87 and the observed cluster radial, mass, central concentration, and velocity distributions, it is possible to calculate simulated effective radii that are comparable in size to the observations. Additionally, the radial trend of cluster sizes increasing with galactocentric distance is also observed in the simulation. This calculation required no free parameters or assumptions beyond M87 being spherically symmetric. We will turn to Section 4.7.2 to illustrate how a better match between theory and observations can be achieved by including an anisotropy profile in the simulation.

Table 4.3: Results of χ^2 Test Comparing Simulations with Different Values of β to Observations

β	χ^2
-1	27.98
-0.5	28.57
0	30.16
0.2	36.24
0.5	56.39
0.8	112.08

4.7.2 Anisotropic Cases

After comparing the isotropic case to observations, the obvious next step is to compare simulations with different values of β to observational effective radii. Introducing anisotropy into the simulation is one possible way of obtaining a stronger agreement between theory and observations. With Côté et al. (2001) finding evidence for $-0.4 < \beta < 0.4$, we decided to compare the observational results to simulations with $-1 < \beta < 1$ such that the range found by Côté et al. (2001) is sufficiently covered. Simulations with β = -1, 0, 0.5, and 0.8 are shown in Figure 4.29 with the median observational K62 effective radii in black. Simulations with β = -0.5, and 0.2 were also compared to observations. The results of applying a χ^2 for each case can be found in Table 4.3.

The results of the χ^2 testing suggest that the globular cluster population of M87 is tangentially anisotropic, with $\beta = -1$ yielding the lowest χ^2. This is only due to the obvious discrepancy of the simulation predicting much smaller effective radii than observed in the inner regions of M87. Since negative values

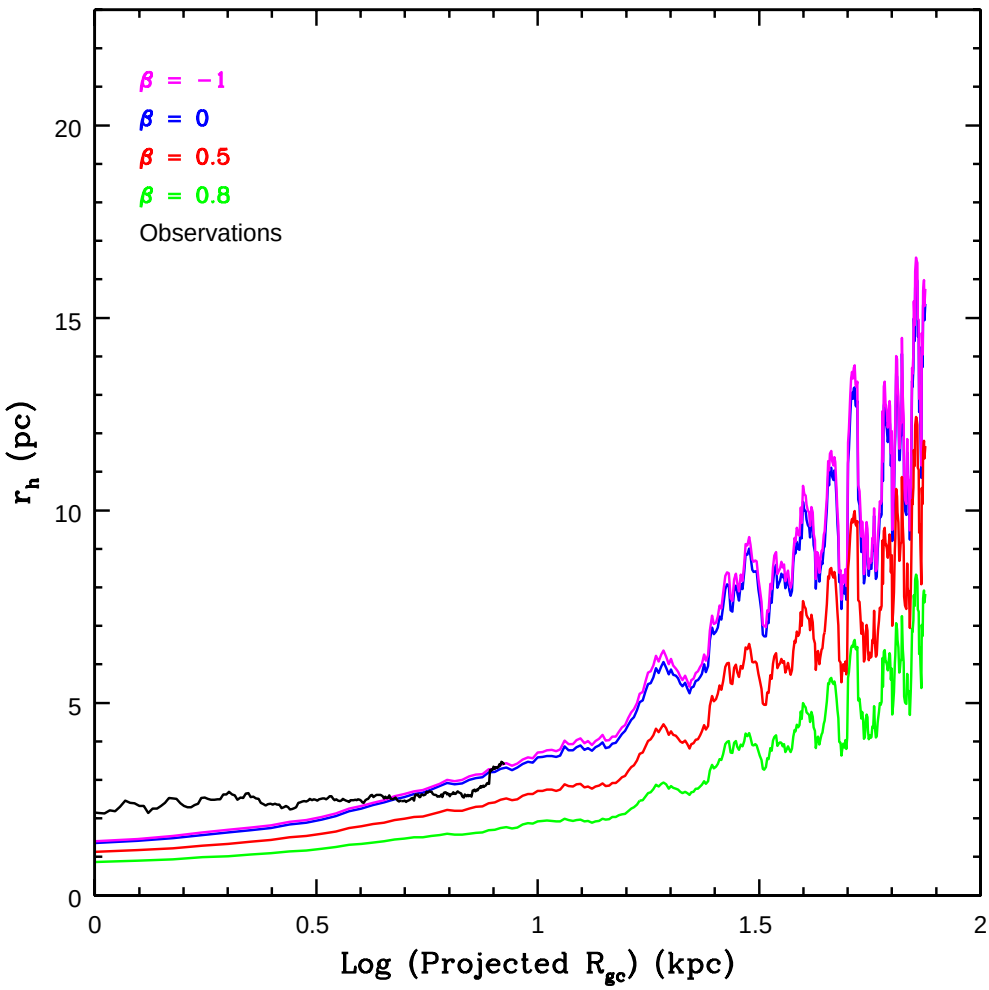

Figure 4.29: Effective radius of each globular cluster compared with its projected distance for different values of β. The black line is the median effective radius taken from K62 model fits to the observations

Table 4.4: Results of χ^2 Test Comparing Simulations with Different Values of β to Observations at Different Galactocentric Distances

β	0 - 1 kpc	1 - 2 kpc	2 - 3 kpc	3 - 4 kpc	4 -5 kpc	5 - 6 kpc	6 - 7 kpc
-1	**9.65**	**8.71**	**5.31**	**2.63**	**0.50**	**0.13**	0.80
-0.5	9.71	8.93	5.57	2.80	0.58	0.14	0.62
0	10.05	9.44	6.09	3.12	0.74	0.19	0.37
0.2	10.74	11.03	7.78	4.55	1.47	0.60	**0.04**
0.5	12.87	14.87	11.67	8.39	4.28	2.86	1.20
0.8	18.52	23.50	20.36	17.28	11.99	10.70	7.88

of β produce larger cluster sizes, this result was not surprising. However, with very little difference in χ^2 for the β equals -1 and isotropic cases, the population can still be taken to be isotropic. We can further test the findings of Côté et al. (2001) that β may increases with galactocentric distance by finding χ^2 in different radial bins. The results of these calculations are found in Table 4.4, with the lowest χ^2's highlighted in bold.

As we see in Figure 4.29 and Table 4.4, matching simulated and observed effective radii suggests that M87 is tangentially anisotropic ($\beta < 0$) for $R_{gc} < 5$ kpc, approximately isotropic for $5 < R_{gc} < 6$ kpc, and radially anisotropic ($\beta > 0$) for $R_{gc} > 6kpc$.

We combine our findings to create an anisotropy profile of M87 such that $\beta = -1$ for $R_{gc} \leq 5$ kpc and $\beta = 0.2$ for $R_{gc} \geq 6$ kpc. β can be set to increase from -1 to 0.2 from $5 < R_{gc} < 6$. We chose to simulate cluster populations with β increasing linearly, through a 1/3 power law, and a 1/6 power law. These β profiles are illustrated in Figure 4.30. Applying a χ^2 test between each simulation and the observations, the β profile that yielded the best fit

was for $\beta \propto R_{gc}$. However, not only were the χ^2 values all very close, but since the increase in β is only over 1 kpc, it only affects a minimal number of simulated clusters, so the manner in which β increases is not important. The effective radius distribution produced by the linear anisotropy profile is plotted with observational effective radii in Figure 4.31.

Our findings that β increases with galactocentric distance are consistent with those of Côté et al. (2001) for M87 and Weijmans et al. (2009) for NGC 3379 and NGC 821. However neither Côté et al. (2001) or Weijmans et al. (2009) found such negative values of β at low galactocentric distances. Looking at the value of χ^2 in different galactocentric distance bins, we see that χ^2 is greater than 1 for $R_{gc} < 3$ kpc. Additionally, it is clear just by looking at Figure 4.31 that the simulation and observations disagree for small galactocentric distances. While it is possible that the gravitational field of M87 is inaccurate at small distances, it is more likely that our understanding of how the tidal field of the galaxy limits cluster size, at least in the inner regions of a galaxy, may be flawed. More specifically, we find that theoretical Jacobi radii do not equal observed K62 tidal radii at small galactocentric distances. However, at larger galactocentric distances, it appears that there is a strong agreement between observationally determined and theoretical calculated cluster sizes. This indicates that to first order, the assumption that a cluster's limiting radius is equal to its Jacobi radius is valid.

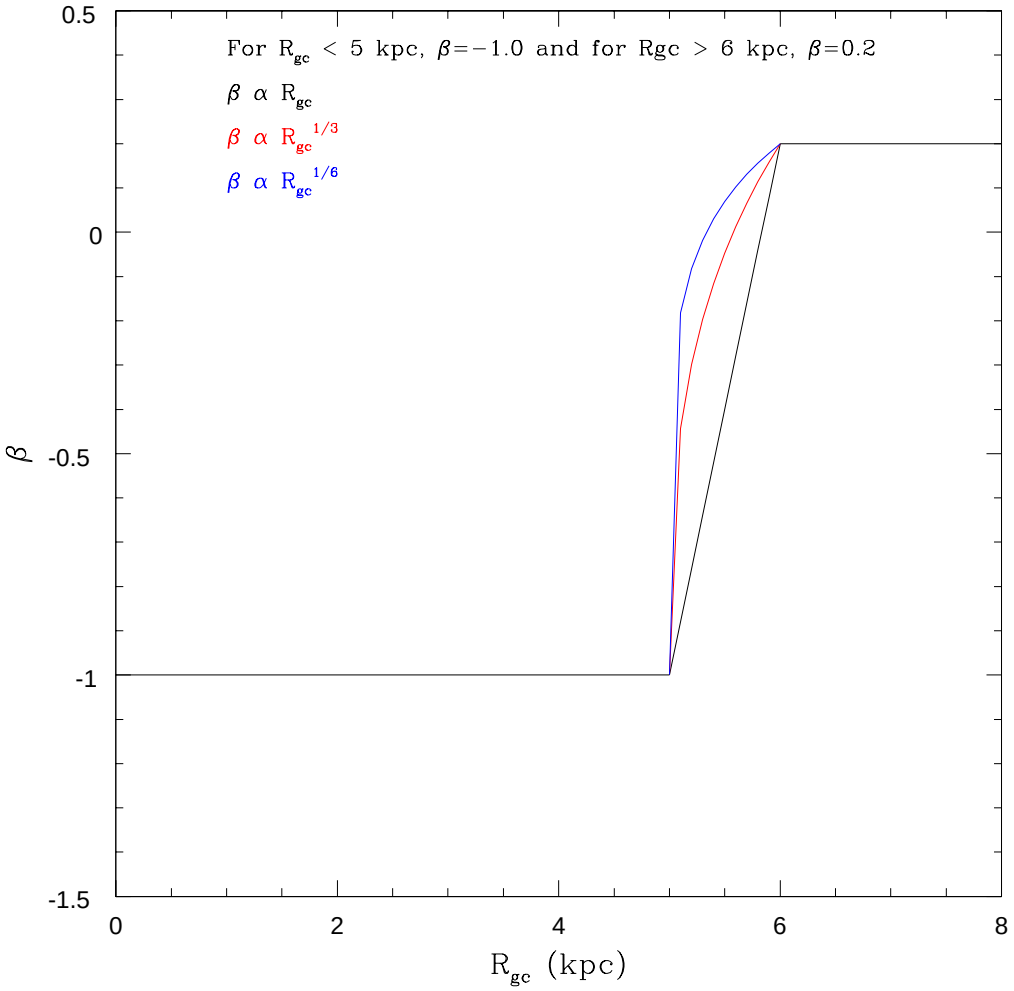

Figure 4.30: Anisotropy parameter (β) profiles of M87 used to simulate globular cluster populations

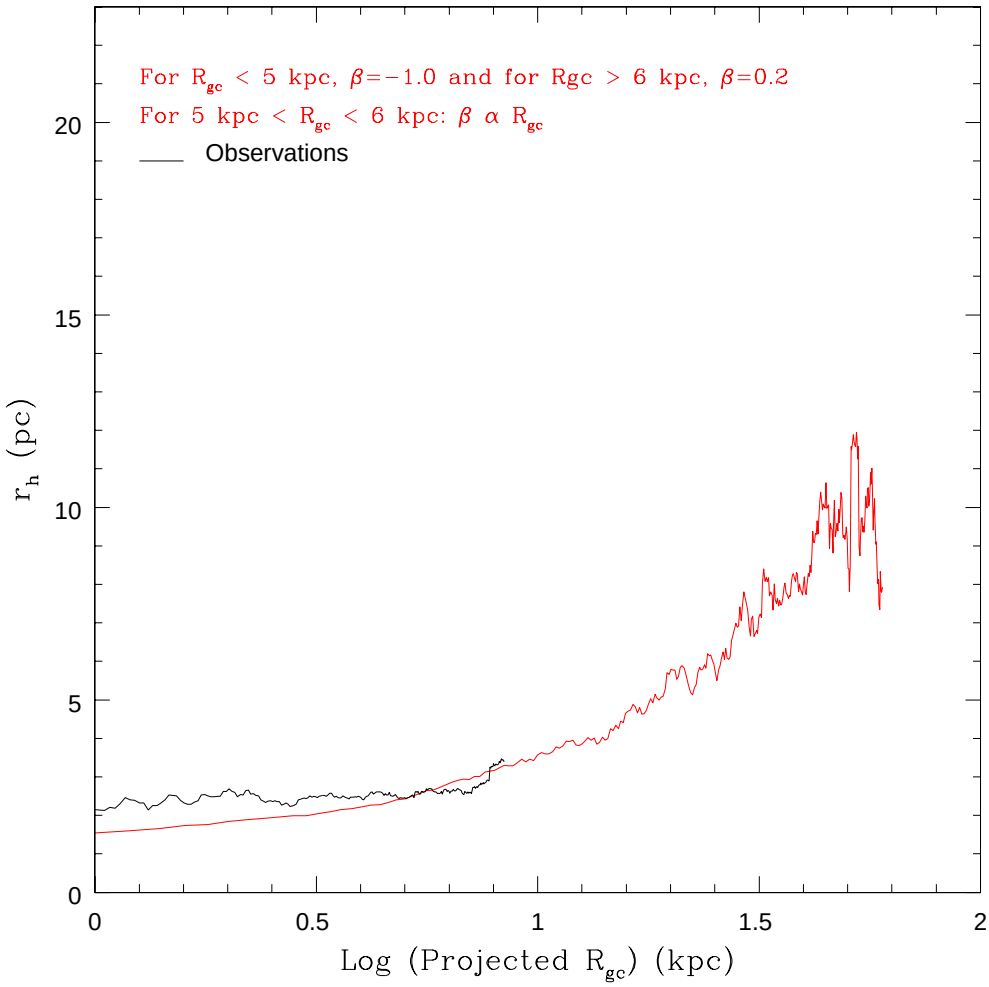

Figure 4.31: Effective radius of each globular cluster compared with its projected distance for a radially dependent $\beta(r)$. The black line is the median effective radius taken from K62 model fits to the observations

Bibliography

Bertin, G. & Varri, A. L. 2008, ApJ, 689, 1005

Binggeli, B., Tammann, G. A., & Sandage, A. 1987, AJ, 94, 251

Binney, J. & Tremaine, S. 2008, Galactic Dynamics, 2^{nd} edition (Princeton, NJ, Princeton University Press)

Brodie, J. P. & Strader, J. 2006, ARA&A, 44, 193

Casetti-Dinescu, D.I., Girard, T.M., Herrera, D., van Altena, W.E., López, C.E., Castillo, D.J. 2007, AJ, 134, 195

Chandrasekhar, S. 1943, ApJ, 97, 255

Churazov, E., Tremaine, S., Forman, W., Gerhard, O., Das, P., Vikhlinin, A., Jones, C., Böhringer, H., & Gebhardt, K. 2010, MNRAS, 404, 1165

Côté, P., McLaughlin, D.E., Hanes, D.A., Bridges, T.J., Geisler, D., Merrid, D., Hesser, J.E., Harris, G.L.H., Lee, M.G., 2001, ApJ, 559, 828, 257B

de Vaucouleurs, G., & Nieto, J.-L. 1978, ApJ, 220, 449

Dehnen, W. 1993, MNRAS, 265, 250

Dinescu, D.I., Girard, T.M., van Altena, W.E. 1999, AJ, 117, 1792

Djorgovski, S. 1993, Astronomical Society of the Pacific Conference Series, 50, 373

Girardi, M., Fadda, D., Giuricin, G., Mardirossian, F., Mezzetti, M., & Biviano, A. 1996, ApJ, 457, 670

Harris, W. E. 1996, AJ, 112, 1487, 2010 Edition

Harris, W.E. 2009, ApJ, 703, 939

Ludlow, A. D., Navarro, J. F., Springler, V., Vogelsberger, M., Wang , J., White, S. D. M., Jenkins, A., & Frenk, C. S. 2010, MNRAS, 406, 137

McLaughlin, D. E. 1999, ApJ, 512, L9

McLaughlin, D. E. & van der Marel, R. P. 2008, ApJS, 161, 304

Meylan, G., Sarajedini, A., Jablonka, P., Djorgovski, S.G., Bridges, T., Rich, R.M., 2001, AJ, 122, 830

Navarro, J. F., Frenk, C. S., & White, S. D. M. 1997, ApJ, 490, 493

Nulsen, P. E. J., & Böhringer, H. 1995, MNRAS, 274, 1093

Prieto, J. L. & Gnedin, O. Y. 2008, ApJ, 689, 919

Tremaine, S., Richstone, D.O., Byun, Y.-L., Dressler, A., Faber, S. M., Grillmair, C., Kormendy, J. and Lauer, T. R. 1994, AJ, 107, 634

von Hoerner, S. 1957, ApJ, 125, 451

Weijmans, A., Cappellari, M., Bacon, R., de Zeeuw, P. T., Emsellem, E., Falcon-Barroso, J., Kuntschner, H., McDermid, R. M., van den Bosch, R. C. E., and van de Ven, G., 2009, MNRAS, 398, 561

Zait, A., Hoffman, Y. & Shlosman, I. 2008, ApJ, 682, 835

Chapter 5

Application to the Milky Way

With a framework in place for calculating theoretical tidal radii, it is only a matter of changing the gravitational potential field to apply this method to other galaxies besides M87. However, for any extragalactic globular cluster population we will again be forced to compare a simulated globular cluster population to observations as we did in Chapter 4. The Milky Way, on the other hand, presents a unique cluster population which allows us to compare theoretical and observational tidal radii on a cluster to cluster basis. More specifically, the Milky Way clusters are the only population that can be measured in three dimensions. For example, when comparing theory and observations in Chapter 4, we are forced to compare the relationship between cluster size and projected galactocentric distance, as observations of M87 project the galaxies cluster population onto the two dimensional plane of the sky. However for the Milky Way globular cluster population, all cluster positions are known in three dimensions. Furthermore, since integrating the orbits of extragalactic globular clusters is currently not possible, the Milky Way is again unique in the sense that it is the only cluster population in which we can use perigalactic distances as opposed to current galactocentric distances for calcu-

lating tidal radii. This makes the Milky Way globular cluster population the best possible testbed for exploring our assumption that the theoretical radius of a cluster, defined in Chapter 2 as the Jacobi radius (r_j), is the same as the limiting radius (r_k) of a cluster. A match between r_j and r_k will validate our comparison between theory and observations in Chapter 4. A discrepancy will suggest that other factors play a role in cluster size in addition to galactic gravitational potential, cluster mass and perigalactic distance.

5.1 Theoretical Tidal Radii

When calculating the tidal radius of a globular cluster, we operate under the assumption that cluster size is imposed at the perigalacticon of a cluster's orbit, as this is where the cluster reaches the deepest point in the gravitational potential of the galaxy. Dinescu et al. (1999) have compiled a catalog of the absolute proper motions of 38 globular clusters and integrated their orbits using the Galactic potentials of Johnston et al. (1995) and Paczyński (1990). In addition to the Dinescu et al. (1999) catalog, Casetti-Dinescu et al. (2007) integrated the orbits of six more galactic globular clusters with the Galactic potential of Johnston et al. (1995). Due to the use of only the Johnston et al. (1995) Galactic potential in Casetti-Dinescu et al. (2007), it is what we will use in our calculations of tidal radius. The Galactic potential is given as

$$\Phi_{bulge} = -\frac{GM_b}{r+c} \tag{5.1}$$

$$\Phi_{disk} = -\frac{GM_d}{\sqrt{R^2 + (a_d + \sqrt{z^2 + b_d^2})^2}} \tag{5.2}$$

$$\Phi_{halo} = v_0^2 ln(1 + \frac{r^2}{d^2}) \tag{5.3}$$

where r is the cluster's perigalactic distance, R and z are the cluster's perigalactic position in cylindrical coordinates, $M_b = 3.4 \times 10^{10} M_\odot$, $c = 0.7$ kpc, $M_d = 10^{11} M_\odot$, $b_d = 0.26$ kpc, $v_0 = 128$ km s^{-1}, and $d = 12.0$ kpc (Johnston et al., 1995). The perigalactic distances determined by Dinescu et al. (1999) and Casetti-Dinescu et al. (2007), along with their uncertainties are illustrated in Figure 5.1 compared with their present galactocentric distance. The dotted line represents $R_p = R_{gc}$. Since orbital parameters as determined by Dinescu et al. (1999) and Casetti-Dinescu et al. (2007) are averages over a number of cycles in a 10 Gyr integration time, all averaged orbital parameters (including R_p as seen in Figure 5.1) will have uncertainties equal to the dispersions over the number of cycles. The top plot in Figure 5.1 is of all the globular clusters, while the bottom plot excludes Pal 3. As seen in the top plot, since Pal 3 has a large galactocentric distance (95.7 kpc), perigalactic distance (82.5 kpc) and measured limiting radius (107.8 pc), including it in the diagram makes it difficult to observe any trends in the data. For the same reason, Pal 3 is not included in any remaining figures or discussion, however it was monitored to ensure it did not present an outlying datapoint.

Using the Galactic gravitational potential of Johnston et al. (1995) (Equations 5.1-5.3), each cluster's perigalactic distance (Figure 5.1) and mass (Harris, 1996 (2010 Edition)), the theoretical tidal radius of 44 Galactic globular

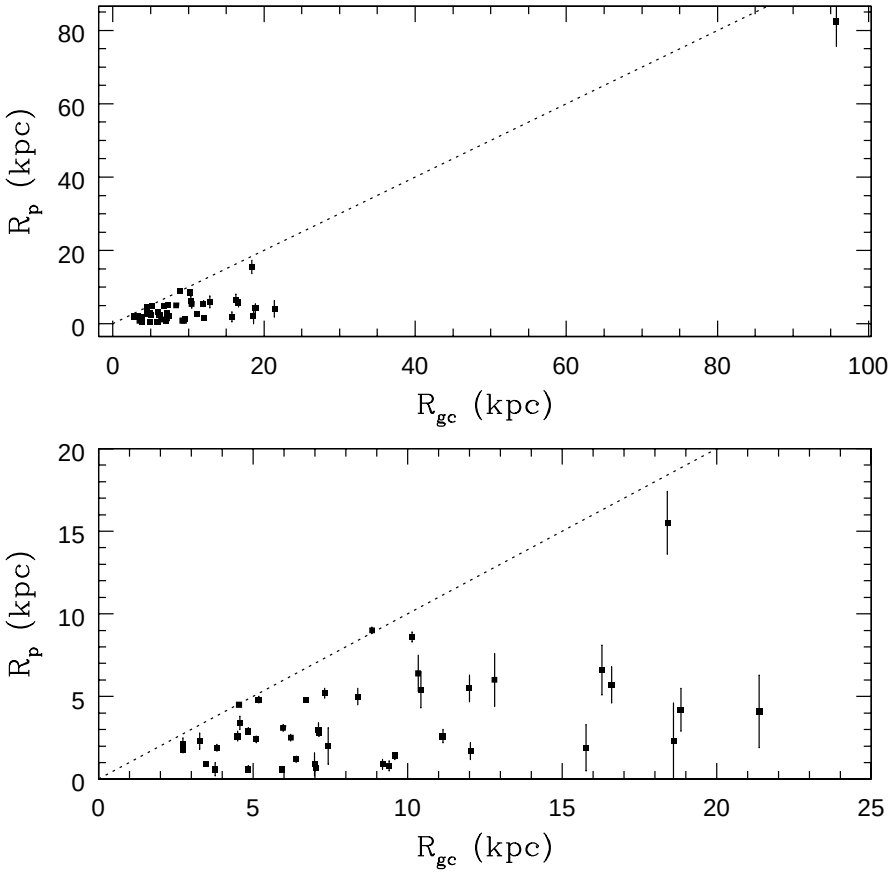

Figure 5.1: Perigalactic distance versus galactocentric distance for all Milky Way globular clusters (Top) and excluding Pal 3 (Bottom). Data taken from Dinescu et al. (1999) and Casetti-Dinescu et al. (2007).

clusters was determined via Equation 2.22. It is important to note that the Bertin & Varri (2008) definition for tidal radius requires that the gravitational potential of the host galaxy be spherically symmetric. Due to the presence of the galactic disk (Equation 5.2), the gravitational field of the Milky Way is not spherically symmetric. This is evident in Equation 5.2, which requires both a cluster's distance from the center of the galaxy in the plane of the disk (R) and its distance from the disk itself (z). In the next section, we will test how the use of the non-spherically symmetric potential of the Milky Way in Equation 2.22 could influence theoretical tidal radii calculations.

The theoretical tidal radius of each cluster with respect to its perigalactic distance (Top) and present galactocentric distance (Bottom) is illustrated in Figure 5.2. The uncertainty in tidal radius is due to uncertainty in perigalactic distance. As expected from our simulation in Chapter 4, we see in Figure 5.2 an increase in cluster size with distance, and a spread in cluster sizes at a given distance due to a spread in cluster mass.

5.2 Comparison with Observations

With the theoretical tidal radius calculated for each Galactic globular cluster with a solved orbit, it is now possible to determine if theoretical tidal radii (r_j) are equal to the tidal radii measured by King (1966) model fitting (r_k). For each of the 44 globular clusters with solved orbits, their limiting radius as determined by a K66 model was taken from the Harris (1996) (2010 Edition) catalog. We assigned an uncertainty of 10% to each value. It is important to note that while we used K62 models to determine cluster sizes in M87, we

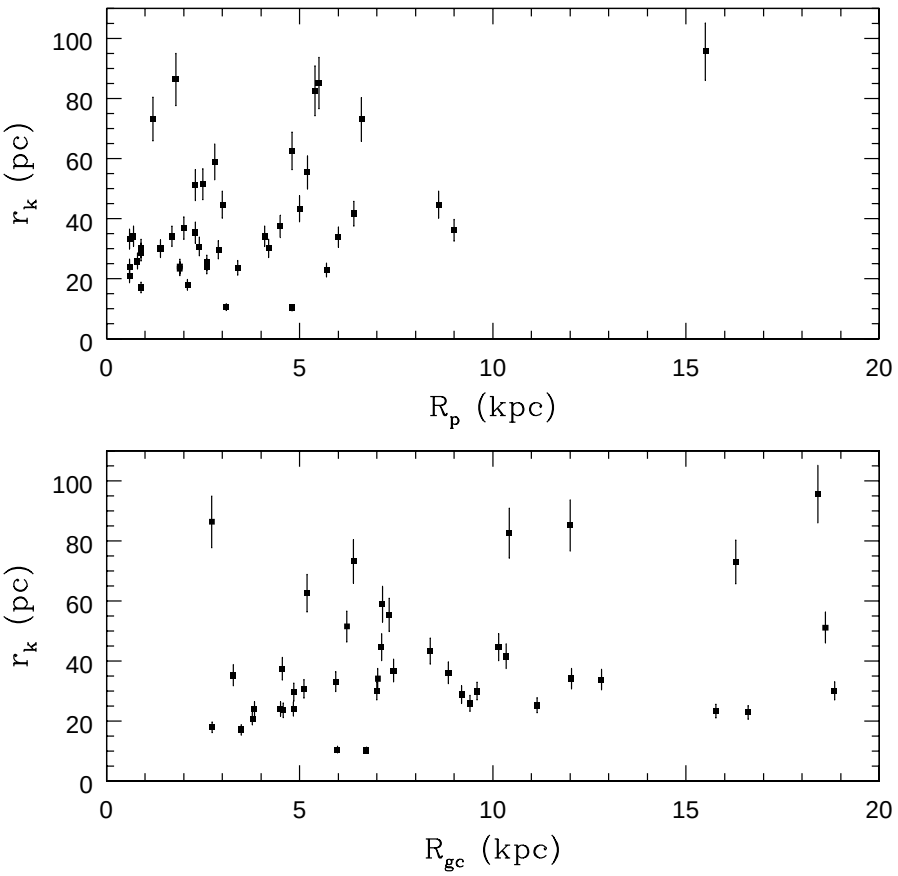

Figure 5.2: Measured tidal radius (limiting radius) versus perigalactic distance (Top) and galactocentric distance (Bottom) for Milky Way globular clusters.

are now using K66 models to determine the sizes of globular clusters in the Milky Way. However, since individual stars within Milky Way clusters can be resolved, their brightness profiles can be accurately determined using star counts. This results in very little difference between K62 and K66 model fits.

Unlike the cluster population of M87, the masses of the Milky Way globular clusters are known. Therefore, similar to Figure 4.18 in Chapter 4, cluster sizes can be normalized by a factor of $1/(M/M_{\odot})^{\frac{1}{3}}$ to eliminate the spread in the top plot of Figure 5.2. This is illustrated in Figure 5.3 for both observational tidal radii (top) and theoretical tidal radii (bottom). While in Figure 4.18 this normalization resulted in the complete elimination of scatter due to cluster mass, scatter is still present in both the upper and lower plots of Figure 5.3. This was not surprising, as two clusters with the exact same perigalactic distance and mass can still have different theoretical tidal radii as their distance from the galactic disk at perigalacticon still plays a role in limiting cluster size. The closer a cluster is to the galactic disk at perigalacticon, the stronger the tidal field will be, which results in a smaller theoretical tidal radius. In the case of the observational tidal radii (Figure 5.3 - Top), while the normalization by cluster mass has minimized some of the scatter seen in Figure 5.2 (top), it still does not perfectly reflect the normalized theoretical distribution. This suggests that our theoretical calculation of Milky Way cluster tidal radii is incorrect. A comparison on a cluster to cluster basis will provide further insight into why the theoretical and observational tidal radii of Milky Way clusters are not in agreement.

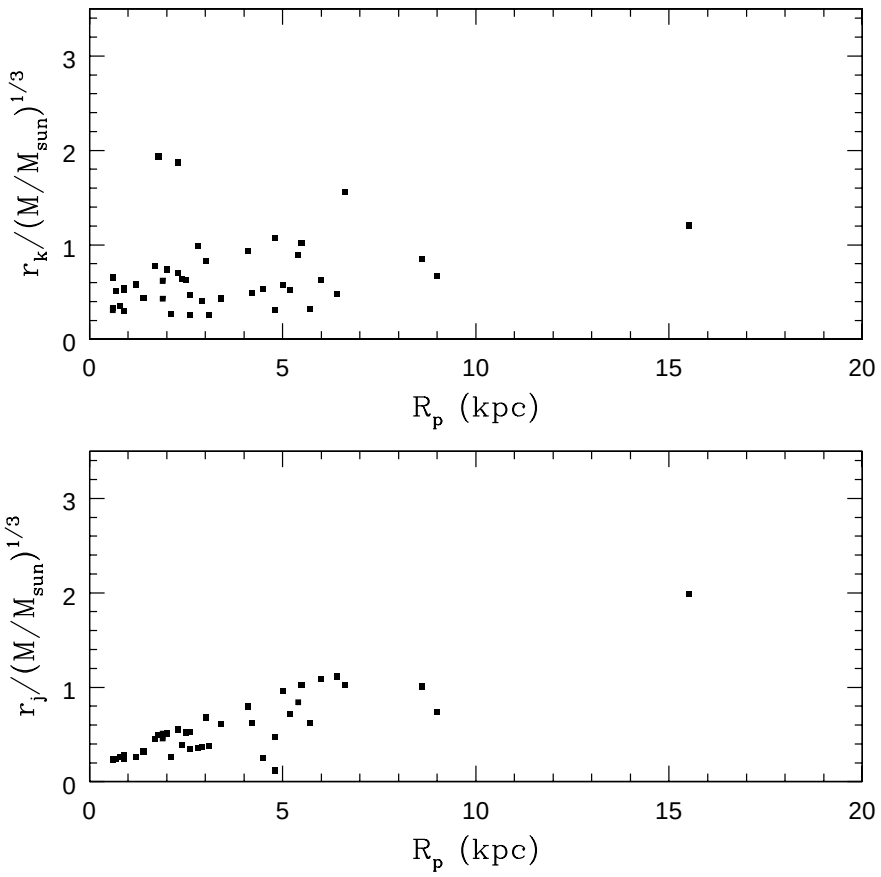

Figure 5.3: Observational (Top) and theoretical (bottom) tidal radius divided by $(M/M_{\odot})^{\frac{1}{3}}$ versus perigalactic distance for Milky Way globular clusters.

To best compare theory and observations for individual clusters, we determine the ratio of the difference between theoretical and observational tidal radii ($r_j - r_k$) to the average of the two radii ($(r_j + r_k)/2$). If theory and observations are in agreement, the ratio will be approximately zero. Clusters which have a ratio greater than zero will be clusters which overfill their Roche surface, while clusters with ratios less than zero will underfill their Roche surface. If non-zero ratios turn out to be the norm, then our assumption that $r_j = r_k$ may be invalid. The comparison between theory and observations is illustrated in Figure 5.4.

As seen in Figure 5.4, while some clusters seem to be very near the $r_j = r_k$ dashed line, the majority of clusters appear to overfill their Roche lobe, with some underfilling their Roche surface. This suggests that our assumption that $r_j = r_k$ is incorrect. It then leads us to question whether our understanding of how cluster tidal radii are related to the gravitational field is incorrect. However, before we address this issue, we first consider the use of a non-spherically symmetric gravitational field for calculating theoretical tidal radii.

To determine whether the disk of the Milky Way is the reason we do not find $r_j = r_k$, we re-plot Figure 5.4, but with the x-axis changed to the inclination of each cluster's orbit (Figure 5.5). Each cluster has been colour coded based on the ratio of the difference between observed and theoretical tidal radius to average tidal radius.

From Figure 5.5 we see that all the red data points (except NGC 7089) which mark clusters with ratios between 70 and 140 % all have low orbital inclinations. Hence their orbital plane is very close to the plane of the disk. This

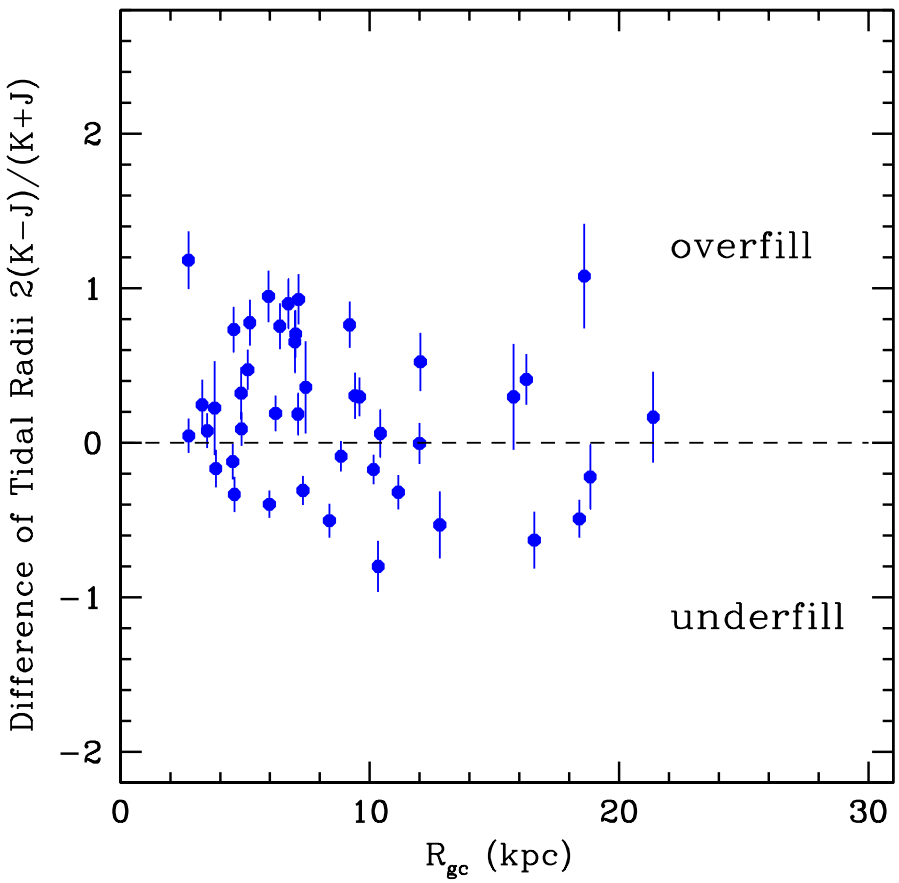

Figure 5.4: Ratio of difference between observed and theoretical tidal radius to average tidal radius versus galactocentric distance for Milky Way globular clusters.

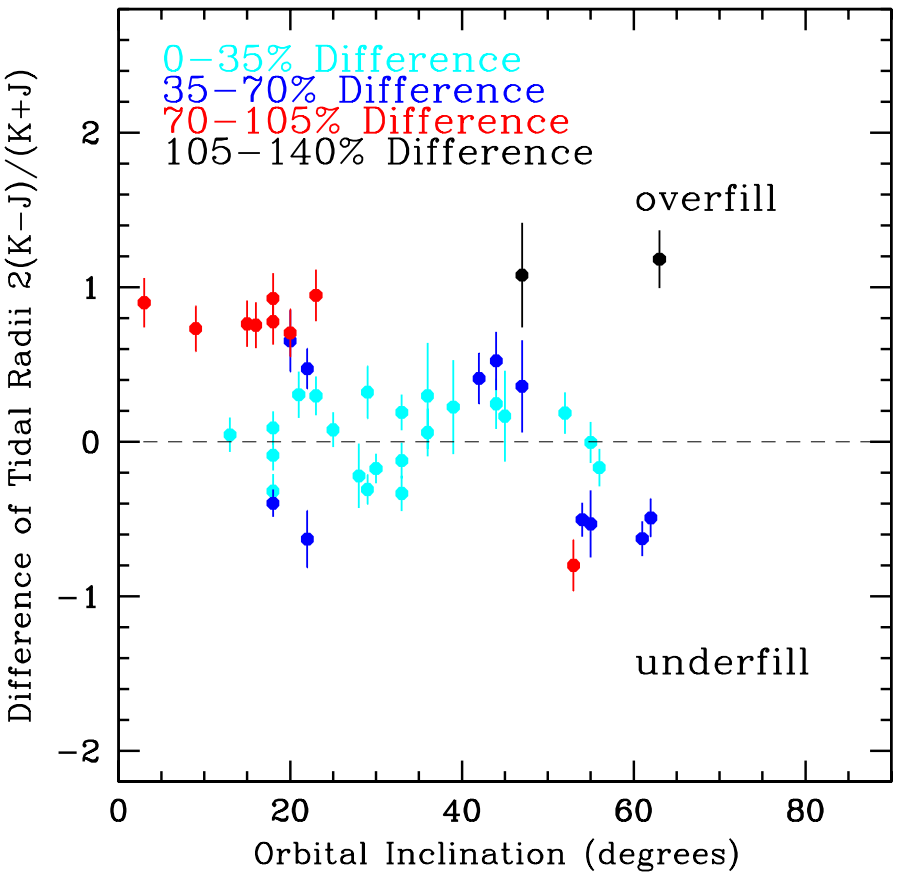

Figure 5.5: Ratio of difference between observed and theoretical tidal radius to average tidal radius versus orbital inclination for Milky Way globular clusters.

suggests that the disk has a strong influence on these clusters, and our calculation of r_j is likely incorrect. However, the two black data points marking ratios between 105-140 % with observed tidal radii greater than their theoretical tidal radii and NGC 7089 are still left unexplained. We now plot each clusters perigalactic position in cylindrical coordinates (R_{xy}, z), with each cluster's ratio in Figure 5.5 identified by each data point's colour. This is illustrated in Figure 5.6.

From Figure 5.6, we see that the two datapoints which have the greatest deviation from r_j (black) have perigalactic locations very close to the plane of the disk. Since the disk plays an important role in restricting these cluster sizes at perigalacticon, the calculation of their theoretical tidal radii is also likely incorrect. Furthermore, of the two black data points, the cluster that is farthest from the disk which has the largest ratio is Pal 5. This is important because Pal 5 has well-documented tidal tails (Odenkirchen et al., 2003). Therefore it is expected that fitting the brightness profile of Pal 5 with a King (1966) model would yield an inaccurate tidal radius, as the presence of tidal tails makes it difficult to determine where on the brightness profile the cluster ends and the tails begin. We can also apply this argument to NGC 7089, the final red data point that has been left unexplained, as Grillmair & Irwin (1999) documented extended tidal tails in their observations of this cluster as well.

So while Figure 5.4 gave the initial impression that the assumption $r_j = r_k$ is incorrect, Figures 5.5 and 5.6 have shown that using a non-spherically symmetric potential in Equation 2.22 is likely the cause for the most notable discrepancies. However for clusters less affected by the galactic disk, it still

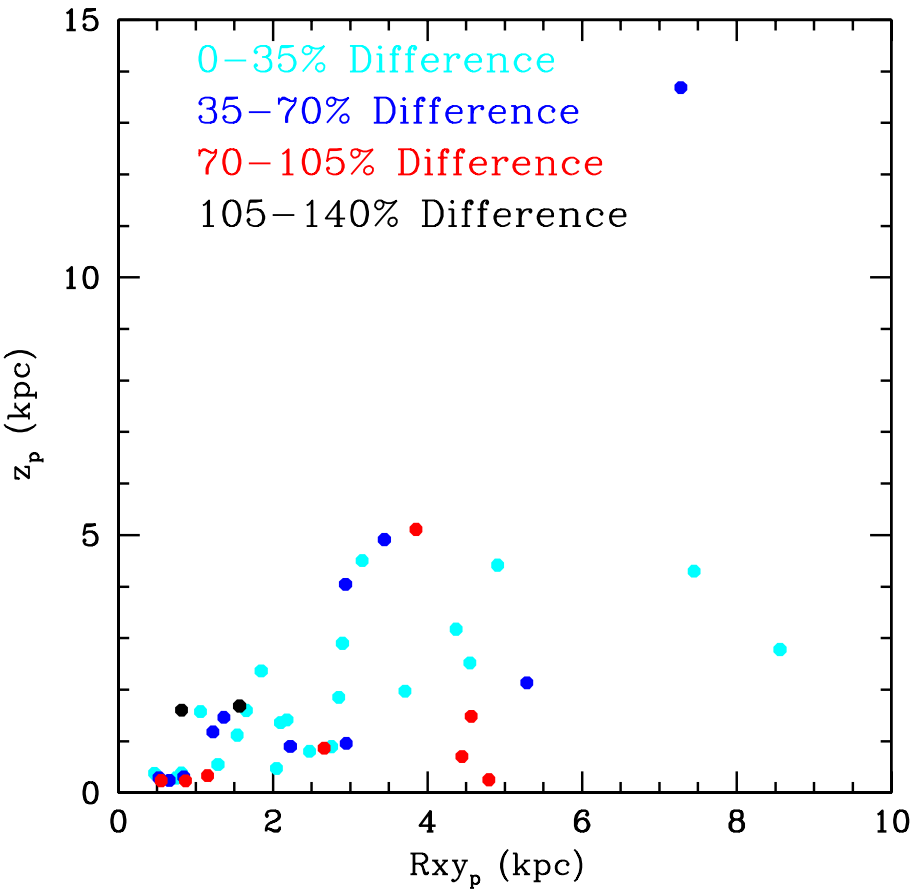

Figure 5.6: Cylindrical coordinate of each cluster's perigalactic location, with clusters colour based on the ratio of the difference between observed and theoretical tidal radius to average tidal radius.

appears the assumption that r_j and r_k are approximately equal is still valid. Work regarding the derivation of a cluster's tidal radius in a non-spherically symmetric potential is needed before the Milky Way can be properly used to compare theoretical and observational tidal radii. Looking forward, this is something that could be done, perhaps numerically, and will improve the comparison between r_j and r_k for Milky Way globular clusters. However for galaxies without a disk, which likely have a spherically symmetric potential (e.g. M87), we conclude the assumption that $r_j \sim r_t$ is both reasonable and unavoidable when dealing with globular cluster populations in other galaxies.

Bibliography

Bertin, G. & Varri, A. L. 2008, ApJ, 689, 1005

Binney, J. & Tremaine, S. 2008, Galactic Dynamics, 2^{nd} edition (Princeton, NJ, Princeton University Press)

Casetti-Dinescu, D.I., Girard, T.M., Herrera, D., van Altena, W.E., López, C.E., Castillo, D.J. 2007, AJ, 134, 195

Dinescu, D.I., Girard, T.M., van Altena, W.E. 1999, AJ, 117, 1792

Grillmair, C. J. & Irwin, M. 1999, AAS, 31, 905

Harris, W. E. 1996, AJ, 112, 1487, 2010 Edition

Johnston, K.V., Spergel, D.N., Hernquist, L. 1995, ApJ, 451, 598

King, I. R. 1966, AJ, 71, 64

McLaughlin, D. E. & van der Marel, R. P. 2008, ApJS, 161, 304

Odenkirchen, M., Grebel, E. K., Dehnen, W., Rix, H., Yanny, B., Newberg, H. J., Rockosi, C. M., Martínez-Delgado, D., Brinkmann, J., Pier, J.R. 2003, AJ, 126, 2385

Paczyński, B. 1990, ApJ, 348, 485

Chapter 6

Conclusions

We present the observed tidal and effective radii of approximately 2000 globular clusters within 10 kpc of the center of the giant elliptical galaxy M87. Cluster sizes were determined by fitting the surface brightness profiles of individual globular clusters with King (1962) models. A theoretical cluster population was then simulated which has the same radial distribution, velocity dispersion, and mass distribution as the observed cluster population of M87. Placing the simulated population within the known tidal field of M87 (McLaughlin, 1999), the orbit of each simulated cluster was solved. Using the formalism of Bertin & Varri (2008), the theoretical tidal and effective radius of each simulated cluster was then determined based on each cluster's mass, and its perigalactic position within the tidal field of the galaxy.

The relationship between median cluster size and projected galactocentric distance was used to compare theoretical and observational tidal radii. To first order, it appears that the assumption that a cluster's observed tidal radius is equal to its theoretical radius. Both the theoretical and observational distributions result in a general increase in cluster size with galactocentric distance. This is expected, as the farther a cluster is from the galactic center, the weaker

is the tidal field to which the cluster is exposed. This results in larger tidal radii at large galactocentric distances. However upon closer inspection, the theoretical and observational distributions are not in complete agreement, as tidal theory tends to underestimate cluster sizes in the inner regions of M87. Unfortunately, for the outer regions of M87, we reach the radial limit of our observations right where the comparison between theory and observations becomes interesting, and theoretical tidal radii may either be in agreement or overestimate cluster sizes. An HST proposal has just recently been approved to observe the outer regions of M87, and future work will involve the comparison of theoretical and observational tidal radii at large galactocentric distances.

One possible explanation for the discrepancy between theory and observations within the inner regions of M87 which we explore is the effect of orbital anisotropy on the simulated distribution of cluster sizes. The initial comparison between observations and theory assumed the simulated cluster population had an isotropic velocity dispersion, such that the observed line of sight velocity dispersion of the M87 cluster population was independent of direction. By instead assuming that clusters in different regions of the galaxy may have different velocity dispersions in different directions, we can compensate for the discrepancy between theoretical and observational cluster sizes. For example, by assuming that in the inner regions of M87 that cluster orbits are tangentially anisotropic, cluster orbits will tend to be more circular. This in turn keeps clusters at larger perigalactic distances, which results in larger cluster sizes. At larger galactocentric distances, if we take the cluster population to be radially anisotropic such that clusters have very eccentric orbits, clusters will be brought close to the galactic center at perigalacticon, resulting in

smaller cluster sizes. This sort of orbital anisotropy profile is consistent with recent observations and simulations (e.g. Weijmans et al. (2009), Ludlow et al. (2010)). We include a "best guess" anisotropy profile which yields a stronger agreement between theoretical and observational tidal radii. Future work will include the use of Monte Carlo Markov Chain formalism to explore a broad range of anisotropy profiles to find the profile which best matches theoretical cluster sizes to observations.

Since our comparison between theoretical and observational tidal radii of clusters in M87 is limited to the projected distribution of cluster sizes, we also use the cluster population of the Milky Way to compare theory to observations. The Milky Way cluster population presents a unique dataset, in the sense that it is the only cluster population in which the orbits of select clusters have been solved. This allows for the comparison of theoretical and observational tidal radii on a cluster-to-cluster basis. When this comparison was made, we found that tidal theory does not provide an accurate estimate of observed cluster sizes. However, this discrepancy can easily be explained by the presence of the galactic disk. The calculation of a cluster's tidal radius, as given by Bertin & Varri (2008), assumes the tidal field of the host galaxy is spherically symmetric. While this is likely the case for M87, it is most definitely not true for the Milky Way. Therefore the discrepancy between theoretical and observational cluster sizes for Milky Way globular clusters is not surprising. Future work will involve the proper calculation of a cluster's theoretical tidal radius in a non-spherically symmetric galactic potential, such that the Milky Way cluster population can be properly used to compare theoretical and observational cluster sizes.

An additional explanation for the discrepancy between theoretical and observational tidal radii which we wish to explore is based on the assumption that a cluster's tidal radius is imposed at perigalacticon. As mentioned in Chapter 2, recent studies are finding that an orbit averaged tidal radius is more accurate than using a cluster's perigalactic distance to calculate tidal radii (e.g. Brosche, Odenkirchen, & Geffert (1999), Kupper et al. (2010)). Unfortunately, there is no agreed-upon technique in place to calculate a cluster's orbit averaged tidal radius. We wish to explore, through the use of N-body simulations, how a cluster's tidal radius will change over the course of its orbit, and from these simulations develop a theoretical method of determining an orbit-averaged tidal radius which is comparable to observations.

Combining the comparison of theoretical and observational tidal radii of clusters in M87 in this study with our future work of observing the outer regions of M87, studying the influence of anisotropy profiles on cluster sizes, the calculation of tidal radii in non-spherically symmetric potentials, and the calculation of orbit-averaged tidal radii will result in a more complete understanding of how the tidal field of a galaxy influences cluster size. We will be able to say with certainty whether the tidal field of a galaxy is solely responsible for determining cluster size, or whether other contributing factors exist. Furthermore, with an established link between theoretical and observation tidal radii, globular clusters can be exploited in new ways to extract information from their host galaxy. This includes the use of globular clusters to trace the mass distribution within a galaxy and its dark matter halo.

Bibliography

Bertin, G. & Varri, A. L. 2008, ApJ, 689, 1005

Brosche, P., Odenkirchen, M., Geffert, M. 1999, New Astron., 4, 133

King, I. R. 1962, AJ, 67, 471

Kupper, A. H. W, Kroupa, P, Baumgardt, H., Heggie , D. C., 2010, MNRAS, 407, 2260

Ludlow, A. D., Navarro, J. F., Springler, V., Vogelsberger, M., Wang , J., White, S. D. M., Jenkins, A., & Frenk, C. S. 2010, MNRAS, 406, 137

McLaughlin, D. E. 1999, ApJ, 512, L9

Weijmans, A., Cappellari, M., Bacon, R., de Zeeuw, P. T., Emsellem, E., Falcon-Barroso, J., Kuntschner, H., McDermid, R. M., van den Bosch, R. C. E., and van de Ven, G., 2009, MNRAS, 398, 561